

Fluctuations of spin and charge
in stripe phases
of layered antiferromagnets

I n a u g u r a l - D i s s e r t a t i o n
zur
Erlangung des Doktorgrades
der Mathematisch-Naturwissenschaftlichen Fakultät
der Universität zu Köln

vorgelegt von
Frank Krüger
aus Hameln

2004

Berichterstatter: Priv. Doz. Dr. S. Scheidl
Prof. Dr. M. Braden
Datum der mündlichen Prüfung: 9. Juli 2004

Abstract

The formation of stripes in layered cuprate high- T_c superconductors and closely related nickelate compounds is generic. Doped charge carriers condense into spontaneously generated anti-phase domain walls between antiferromagnetic insulating regions. In this thesis fluctuations of spin and charge in these two-dimensional stripe superstructures are investigated.

The first part addresses the phenomenon of spin-charge separation. Experimentally charge ordering of stripes is always observed at a higher temperature than the magnetic ordering. The melting of stripes mediated by the unbinding of different types of topological defects, namely charge dislocations, charge loops, and spin vortices is studied. The phase diagram and the critical properties of the phase transitions are calculated in the framework of a renormalization-group analysis in the Coulomb-gas representation of these defects, which interact logarithmically on large scales in two dimensions. Depending on which type of defect proliferates we identify four different phases characterized by the range of charge order, spin order, and a less accessible collinear order. From the resulting phase diagram several scenarios of spin-charge separation are possible. Depending on the interaction parameters the orders can disappear at a single transition or in a sequence of two transitions.

In the second part the spin dynamics of stripes is studied in the framework of a linear spin-wave theory for a minimalistic spin-only model. The magnon dispersion and the magnetic zero temperature structure factor are calculated for diagonal and vertical stripes since both configurations are realized in doped layered antiferromagnets. Acoustical as well as optical bands are included in the analysis. Incommensurate spin fluctuations and the commensurate π resonance at the antiferromagnetic wave vector appear as complementary features of the band structure at different energy scales. The dependence of the spin-wave velocities and the resonance frequencies on the stripe spacing and coupling is calculated. At low doping, the resonance frequency is found to scale inversely proportional to the stripe spacing. Finally, we extend our minimalistic model to a bilayer, allowing for several stripe configurations which differ by the relative location of the stripes in the layers. Again the spectral properties are calculated in linear spin-wave theory. We focus on the bilayer splitting of the magnon bands near the incommensurate low energy peaks as well as near the π resonance, distinguishing between the odd and even channel. We find that an x-shaped dispersion near the π resonance is generic for stripes. The favorable comparison of the results to experimental data suggests that the spin-only model provides a suitable and simple basis for calculating and understanding the spin dynamics of stripes.

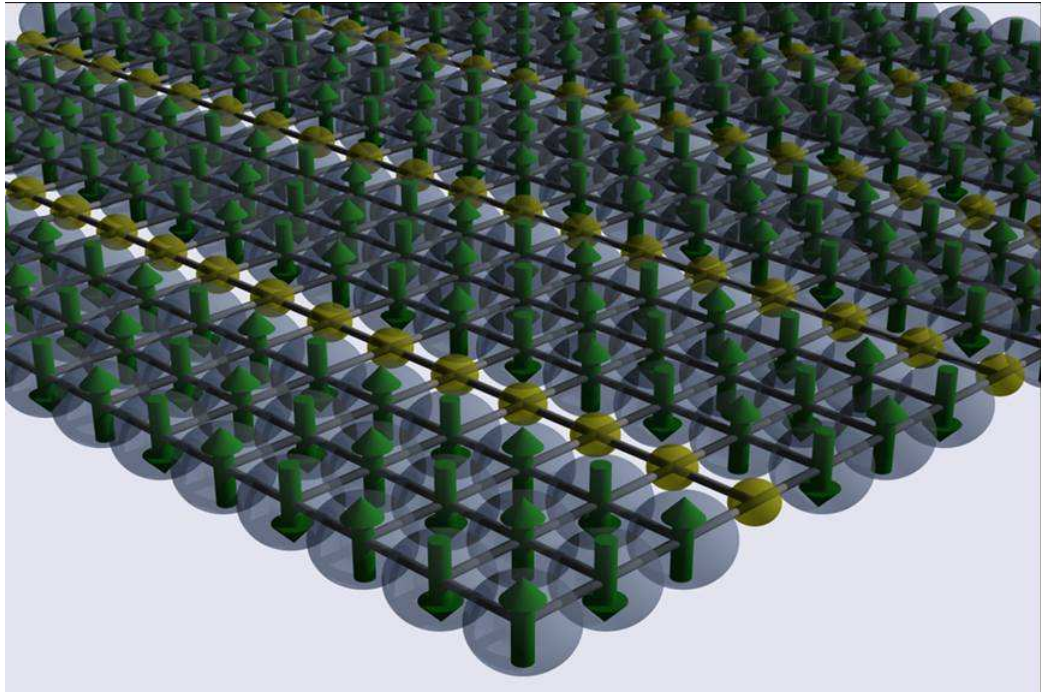


Figure 1: *Minimalistic real-space picture of a stripe phase [90]. The doped holes are assumed to form site-centered rivers which act as anti-phase boundaries between antiferromagnetic spin domains.*

Contents

I	Introduction	9
1	Stripes in high-T_c superconductors and related compounds	9
1.1	Structures and doping mechanisms	11
1.2	Phase diagrams	12
1.3	Theoretical prediction of stripes	14
1.4	Phenomenology of stripes	18
1.5	Spin dynamics	22
2	Outline	25
II	Ordering of spin and charge in stripe phases	29
1	Introduction	30
2	Model	32
2.1	The ground state	32
2.2	Wave-like low energy excitations	33
2.3	Charge order, spin order, and collinear order	34
2.4	Topological defects	35
2.4.1	Vortices	35
2.4.2	Dislocations	38
2.4.3	Topological defects in stripes	39
3	Qualitative understanding of the phase diagram	41
4	Renormalization	43
5	Short review of the KT-transition	44
6	Results	46
6.1	Phase diagram	46
6.2	Correlation lengths of disordered phases	49
7	Discussion and conclusion	51

III	Spin dynamics of stripes	55
1	Introduction	56
2	Spin-only model for a single layer	59
3	Spin-wave theory	62
3.1	Holstein-Primakoff representation	62
3.2	Bogoliubov transformation	64
3.3	Structure factor	65
4	Monolayer results	68
4.1	Pure antiferromagnet	68
4.2	Vertical stripes	70
4.3	Diagonal stripes	73
4.4	Density of states	76
5	Comparison to experiments	79
5.1	$\text{La}_{2-x}\text{Sr}_x\text{NiO}_4$	79
5.2	Cuprates	81
6	Conclusion	85
7	Bilayer model	87
7.1	Energetic estimates	89
7.2	Classical ground states	90
8	Bilayer modifications of spin-wave theory	94
9	Bilayer results	97
10	Discussion	104
IV	Appendix	108
A	Correlation functions \mathcal{C}_ρ , \mathcal{C}_σ , and \mathcal{C}_\parallel	108

B Renormalization of vector-Coulomb gases	110
B.1 Rescaling	111
B.2 Annihilation and fusion	111
B.2.1 Annihilation	112
B.2.2 Fusion	113
B.3 Evaluation for the stripe system	114
C Correlation length in the disordered phase	116
References	118
Kurzzusammenfassung	127
Dank	129
Erklärung	131
Lebenslauf	133

Part I

Introduction

1 Stripes in high- T_c superconductors and related compounds

The first discovery of superconductivity in ceramic copper-oxide compounds by Bednorz and Müller [4] in 1986 came as a great surprise, not only because of the record-high transition temperatures compared to conventional superconductors, but also because these materials are relatively poor conductors in the non-superconducting state. Indeed, this new class of superconductors is obtained by doping parent compounds that are antiferromagnetic Mott insulators, materials in which both the antiferromagnetism and the insulating behavior arise from strong electron-electron interactions. Since local magnetic correlations survive in the metallic state, it is necessary to view these compounds as doped antiferromagnets. In this sense, other related transition-metal oxides, such as layered nickelates which remain insulating when doped or manganites which are prominent for their 'colossal' magnetoresistance, are also doped antiferromagnets.

The number of materials belonging to the high- T_c cuprate family has increased rapidly. One driving force for this growth is the quest for higher and higher superconducting transition temperatures, which have evolved rapidly from the original 30 K in $\text{La}_{1.85}\text{Ba}_{0.15}\text{CuO}_4$ [4] to more than 160 K in 1993 in $\text{HgBa}_2\text{Ca}_2\text{Cu}_3\text{O}_{8+\delta}$ under pressure [80]. A few of the most widely studied systems are $\text{La}_{2-x}\text{Sr}_x\text{CuO}_4$ (LSCO), $\text{YBaCuO}_{6+\delta}$ (YBCO), and $\text{Bi}_2\text{Sr}_2\text{CaCu}_2\text{O}_{8+\delta}$ (BSCCO). The essential ingredient that all cuprate compounds share are two-dimensional CuO_2 layers, whereas everything else is subject to change and thereby appears to be detail, nevertheless, T_c can be strongly enhanced by these 'details'.

Depending on the concentration of the charge carriers within the CuO_2 layers introduced via doping, substitutional or with excess oxygen, the physical properties of the cuprates vary on a broad scale. The undoped samples are insulating antiferromagnets. With increasing doping antiferromagnetic long-range order disappears and the layered cuprates become metallic and superconducting. To the present day, a satisfactory understanding of the mechanism giving rise to the superconducting instability has not been achieved.

The existence of an ordered superconducting phase as well as the anomalous or non-Fermi liquid behavior at optimal doping call for the existence of a quantum critical point apart from the antiferromagnetic one.

Theoretically, in 1989 stripes as a new ordering phenomenon in doped layered antiferromagnets had been predicted [116, 92, 63]: Holes induced by doping condense into arrays of parallel rivers which act like anti-phase domain boundaries for the antiferromagnetic spins. Thus, stripes are a unidirectional combined charge- and spin-density wave. Stripe phases should arise as a compromise between antiferromagnetic interactions among magnetic ions and Coulomb interactions between charges, which both favor localized electrons, and the zero-point kinetic energy of the doped holes, which tends to delocalize charge [29].

Years passed until a broad interest was triggered by experiments on insulating $\text{La}_{2-x}\text{Sr}_x\text{NiO}_{4+\delta}$ (LSNO) and superconducting LSCO [101, 102] observing collective magnetic excitations at satellite positions in the vicinity of the antiferromagnetic wave-vector as well as charge superstructure peaks shifted from the reciprocal lattice vectors. After this first experimental evidence of stripes as a *combined* charge- and spin-density wave phenomenon the field of stripes physics in the cuprates and closely related nickelates began to flourish. More recent experimental evidence [21, 72, 43, 42] for stripes in the paradigmatic high-temperature superconductors (HTSCs) YBCO and BSCCO strengthens the expectation that stripe formation in doped layered perovskites is quite generic. In spite of the striking evidence for stripes in HTSCs, the causal connection between stripe formation and superconductivity still is a mystery. There is a simple linear relation between the inverse stripe spacing and the superconducting T_c observed in several materials including LSCO and YBCO. It is puzzling that both phenomena coexist and that, nevertheless, strongly condensed stripe order tends to suppress superconductivity [99, 51]. For this interplay spin order is more relevant than charge order. In particular, the strength of spin fluctuations appears to play a central role. Static spin order seems to be much less compatible with superconductivity than dynamic spin order. Moreover, there is a clear indication that the optimal situation for superconductivity is stripe correlations that are not too static or strongly condensed, but also not too ethereal or wildly fluctuating [29].

Theoretically, there are several scenarios suggesting that quantum critical behavior arising from stripes physics plays a central role for the understanding of high- T_c superconductivity [52, 115].

The focus of this thesis is neither on the microscopic mechanism of the stripe formation nor on the mechanism of superconductivity in the cuprates for which stripes may play an essential role. We rather explore the interplay between charge and spin order in stripe phases and focus on the spin dynamics of ordered stripe phases. In this introductory part we adumbrate the structural features of layered cuprate and nickelate compounds and briefly discuss the mechanisms of doping charge carriers in the magnetic layers. Furthermore, generic aspects of the phase diagrams are compiled and the theoretical prediction as well as the phenomenology of stripes are briefly discussed. Finally, in section 2 an outline of this thesis is given.

1.1 Structures and doping mechanisms

Here we sketch only a few characteristics of the structures of the layered cuprates and related nickelates. For a detailed description of the crystal structures, lattice parameters and interatomic distances of various cuprates and related transition-metal oxides we refer the reader to Refs. [84, 39].

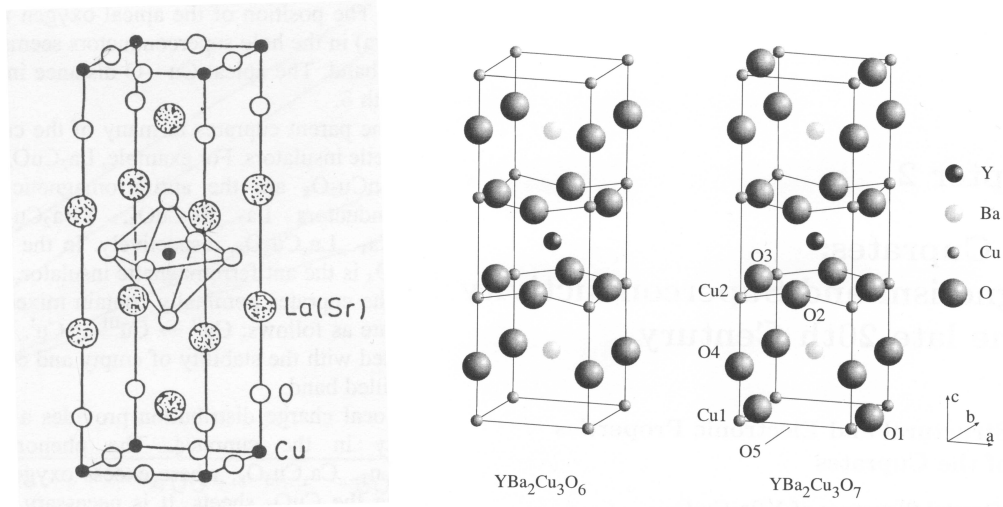


Figure 2: Structures of $\text{La}_{2-x}\text{Sr}_x\text{CuO}_4$ [84] (left) and $\text{YBaCuO}_{6+\delta}$ [35] (middle and right). In LSCO one finds a stack of equidistant CuO_2 layers, whereas in YBCO these layers are grouped in pairs. LSCO is doped by randomly replacing trivalent La^{3+} ions by divalent Sr^{2+} ions, whereas in YBCO the excess oxygen orders in chains in the adjacent layers.

The MO_2 layers ($M = \text{Cu, Ni}$) and the adjacent oxygen ions form a square lattice of corner sharing MO_6 octahedra or MO_5 pyramids (cf. Fig. 2), giving rise to a tetragonal symmetry which is slightly distorted to an orthorhombic structure in many of the related materials. The structures can be classified by the number n of MO_2 layers per unit cell, LSCO and LSNO are monolayer compounds ($n = 1$) whereas YBCO and BSCCO belong to the class of bilayer materials ($n = 2$), they have two closely spaced CuO_2 layers per unit cell, and the inter-bilayer distance is much larger than the intra-bilayer one.

In La_2MO_4 the generic way of doping holes in the MO_2 layers is to partially replace the trivalent La^{3+} by divalent ions such as Sr^{2+} or Ba^{2+} (substitutional doping). In this case the concentration of doped carriers in the MO_2 layers equals the concentration of Ba or Sr impurities. Since these impurities are randomly distributed, disorder may play an important role. In principle, YBCO can also be doped by substituting Y^{3+} ions with divalent ones. However, the way usually chosen to change the doping level in YBCO or BSCCO is to play with the oxygen content, which influences the doping in a more subtle way. The excess oxygen orders in Cu-O chains in adjacent layers (cf. Fig. 2). A lack of electrons in these chains is compensated by electrons from the CuO_2 layers.

1.2 Phase diagrams

We briefly discuss generic aspects of the phase diagrams of the cuprates and the closely related nickelates. Although there are several similarities between this two classes of doped layered antiferromagnets, one crucial difference is that, by doping, the cuprates can be driven into a superconducting state on contrary to the nickelates.

The parent compounds are antiferromagnetic Mott insulators as a consequence of strong electron-electron interactions. Insulating behavior arises from a strong on-site repulsion of the electrons, strong antiferromagnetic nearest neighbor couplings between the metallic spins in the MO_2 layers as a consequence of a double exchange via the intervening oxygen ions. Typically, the charge-transfer gap is of the order of a few eV, the Néel temperatures are about a few hundred Kelvin. Due to the $3d^9$ electron structure of the Cu^{2+} ions the cuprates are spin 1/2 antiferromagnets whereas the Ni^{2+} ions carry a spin $S = 1$ because of their $3d^8$ configuration. Of course, the magnetism of the compounds is only approximately captured by the two dimensional quantum Heisenberg model reduced to an antiferromagnetic nearest neigh-

bor exchange. Within the layers higher order exchange processes lead to weak antiferromagnetic next nearest neighbor couplings or to four-spin couplings. In the cuprates four-spin couplings generated by a cyclic exchange are sufficiently strong [97, 75] and relevant for quantitative purposes. Furthermore small spin anisotropies, Dzyaloshinskii-Moriya interactions and weak 3D couplings are present [47, 48]. In bilayer compounds the couplings between the layers within a bilayer can be quite strong [85].

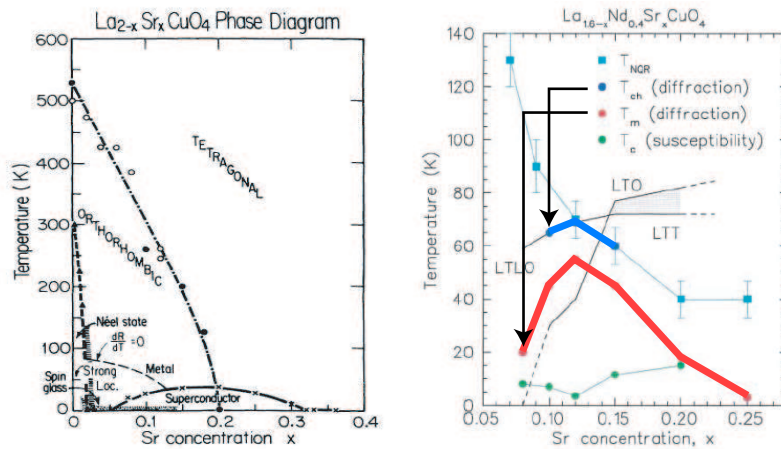


Figure 3: *Left: Temperature vs. doping phase diagram of $\text{La}_{2-x}\text{Sr}_x\text{CuO}_4$ [48] showing the AF phase at low doping and the SC phase which extends over a wide doping range. Furthermore, the structural transition and the metal-insulator transition are displayed. At very low temperatures spin-glass behavior is observed. Right: Charge (ch) and magnetic (m) ordering temperatures $T_{\text{ch}} > T_{\text{m}}$ of stripes in LSCO codoped with Nd. The codoping leads to a stabilization of static stripe order as well as to a reduction of T_{c} . At optimum doping of $x \approx 0.12$ the stripe ordering temperatures reach their maximum values whereas T_{c} shows a dip; from [45].*

At a critical doping long-range antiferromagnetic order disappears and, depending on the material, at low temperatures spin-glass phases are observed. For the appearance of spin-glass behavior disorder plays a fundamental role. In the case of substitutional doping the divalent ions replacing the trivalent ones are randomly distributed. The resulting disorder potential tends to pin the holes in the MO_2 layers. Excess oxygen orders in chains in adjacent layers, therefore the effect of disorder is much weaker in oxygen

doped compounds. In fact, spin glass behavior is observed in substitutional doped LSCO (cf. Fig. 3) but not in YBCO doped with excess oxygen.

With doping the cuprates become metallic and superconducting whereas the nickelates remain insulating. LSCO has a maximum T_c of about 38 K, YBCO with a maximum T_c of 90 K is the first material to support superconductivity at liquid nitrogen temperatures [39]. In general, T_c within one cuprate subgroup increases from single layer over bilayer to trilayer compounds, a fact that is not understood and barely addressed [16, 60]. This neglect may for example be justified by a T_c as high as 90 K encountered in the single layer material $Tl_2Ba_2CuO_{6+x}$, which has a relatively large layer-to-layer distance.

With doping not only the conducting and magnetic properties change, also structural transitions between orthorhombic and tetragonal phases are observed (cf. Fig. 3).

In both, the nickelates and the cuprates, stripe superstructures are observed over a wide doping and temperature range, in the case of the cuprates in the superconducting as well as in the 'normal' phase (cf. Fig. 3), and even at very low dopings in the antiferromagnetic phase [66]. It is significant that charge order always emerges at higher temperatures than spin order (cf. Fig. 3), as observed in cuprates [102, 79, 45] as well as in nickelates [100, 59, 113], which is characteristic [120] of a transition driven by the charge.

1.3 Theoretical prediction of stripes

Self organized local inhomogeneities in doped antiferromagnets were predicted theoretically [116, 92, 93, 63, 28]. They arise because the charge carriers tend to cluster in regions of suppressed antiferromagnetism [91] leading to a strong, short-ranged tendency to phase separation [28]. Because of the long-ranged Coulomb interaction which compete with the short-ranged attractive interactions between holes the system is frustrated and cannot macroscopically phase separate. The best compromise [61, 17] between these competing mechanisms is achieved by allowing the holes to be delocalized along linear stripes acting as anti-phase boundaries for the antiferromagnetic domains in between, which remain more or less in the undoped correlated insulating state. From numerical studies of a minimalistic three-band Hubbard model Zaanen and Gunnarson [116] have derived a picture of charged magnetic domain lines, however they had to choose appropriate geometries and boundary

conditions to force the holes to condense into parallel rivers. It is generally accepted that in the CuO_2 layers the $3d_{x^2-y^2}$ band is the only Cu^{2+} band of relevance. Including the planar $2p_{x,y}$ orbitals of the intervening oxygen ions (cf. Fig. 4) the electronic structure can be modelled by the well-known Emery three-band Hamiltonian [27, 106]

$$\mathcal{H} = \mathcal{H}_0 + \mathcal{H}_1, \quad (1a)$$

$$\begin{aligned} \mathcal{H}_0 = & \epsilon_d \sum_{i\sigma} n_{i\sigma}^d + \epsilon_p \sum_{j\sigma} n_{j\sigma}^p + \sum_{\langle ij \rangle \sigma} t_{pd}^{ij} (d_{i\sigma}^\dagger p_{j\sigma} + \text{H.c.}) \\ & + \sum_{\langle jj' \rangle \sigma} t_{pp}^{jj'} (p_{j\sigma}^\dagger p_{j'\sigma} + \text{H.c.}), \end{aligned} \quad (1b)$$

$$\mathcal{H}_1 = U_d \sum_i n_{i\uparrow}^d n_{i\downarrow}^d + U_p \sum_j n_{j\uparrow}^p n_{j\downarrow}^p + U_{pd} \sum_{\langle ij \rangle \sigma \sigma'} n_{i\sigma}^d n_{j\sigma'}^p. \quad (1c)$$

Here the index $i(j)$ denotes $\text{Cu}(\text{O})$ sites. The operators $d_{i\sigma}^\dagger$ ($d_{i\sigma}$) and $p_{j\sigma}^\dagger$ ($p_{j\sigma}$) create (annihilate) a hole with spin $\sigma = \pm 1/2$ in the copper $d_{x^2-y^2}$ and oxygen $p_{x,y}$ orbitals, respectively. $n_{i\sigma}^d = d_{i\sigma}^\dagger d_{i\sigma}$ and $n_{j\sigma}^p = p_{j\sigma}^\dagger p_{j\sigma}$ are the hole number operators for the corresponding orbitals.

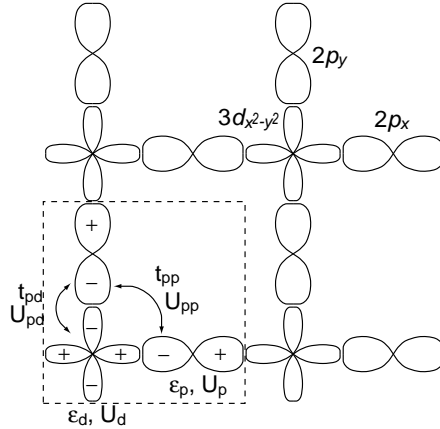


Figure 4: Four unit cells of a CuO_2 layer showing the most relevant orbitals contributing to the three-band Hubbard model (the $3d_{x^2-y^2}$ orbitals of the Cu^{2+} ions and the $2p_{x,y}$ orbitals of the oxygen ions) as well as the most important electronic parameters. Typical values for these parameters are given in Tab. 1.

The on-site energies of the holes in the orbital are denoted by ϵ_d and ϵ_p . The hopping matrix elements between the $d_{x^2-y^2}$ and $p_{x,y}$ orbitals are given by t_{pd} , the corresponding contribution to the Hamiltonian (1) describes a hybridization of these orbitals. Correspondingly, the hybridization of the p orbitals is captured by t_{pp} . On-site Coulomb repulsions of the holes are incorporated by U_d and U_p , while U_{pd} takes the inter-site Coulomb repulsion into account. A standard set of typical electronic parameters is given in Table 1.

$\Delta = \epsilon_p - \epsilon_d$	t_{pd}	t_{pp}	U_d	U_p	U_{pd}	U_{pp}
3.5	1.3-1.5	0.65	8.8-10.5	4-6	≤ 1.2	≈ 0

Table 1: *A widely accepted standard set of typical parameter values (in eV) for the three-band Hubbard model [44, 68].*

In the strong-coupling limit the three-band Hubbard model can be mapped onto a t - J model where the superexchange coupling between neighboring spins in leading order is given by [30]

$$J = \frac{4t_{pd}^4}{(\Delta + U_{pd})^2} \left(\frac{1}{U_d} + \frac{2}{2\Delta + U_p} \right). \quad (2)$$

Using the parameters given in Tab. 1 the superexchange of the cuprates $J \approx 120 - 150\text{meV}$ [62, 37, 97] is slightly overestimated (for further details see Ref. [30]). In the t - J model only states with one additional hole per O-Cu-O unit are allowed, whereby such a hole leads to the formation of a Zhang-Rice singlet. It is shown in numerical studies of the t - J model [28] that dilute holes in an antiferromagnet are unstable against phase separation into a hole-rich and a no-hole phase. This result is not surprising since there is an attractive potential ($-J$) between holes in singlet states on neighboring sites and the mobility of a single hole in an antiferromagnetic environment is strongly suppressed.

Let us come back to the calculations of Zaanen and Gunnarson [116]. As starting point they use a minimalistic version of the three-band Hubbard Hamiltonian (1). For simplicity they neglect the hybridization of the p orbitals ($t_{pp} = 0$) and keep the on-site repulsion on the Cu sites as the only Coulomb interaction term ($U_p = U_{pp} = U_{pd} = 0$). In the undoped system charge excitations are gapped. This is incorporated in the model since the

charge transfer $d^9 \rightarrow d^{10} + p\text{-hole}$ costs an energy $\Delta = \epsilon_p - \epsilon_d > 0$. To allow for the fact that in doped samples the majority of the excess holes are localized on the oxygen ions a large on-site repulsion $U_d > \Delta$ on the copper sites is necessary.

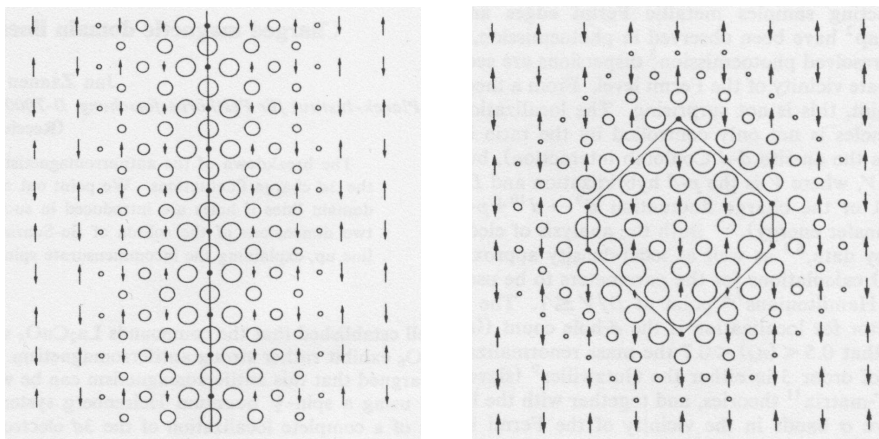


Figure 5: Results of numerical simulations [116] based on the three-band Hubbard model for 10 excess holes in supercells of 9×10 (left) and 10×10 (right) CuO_2 units. The density of excess holes on the oxygen ions is proportional to the radius of the circles and the spins on the Cu lattice are represented by arrows. For the non-quadratic supercell the holes condense into a charged Néel line whereas for the quadratic cell the line is forced to form a ring as a consequence of the periodic boundary conditions.

Treating the Coulomb term $\mathcal{H}_1 = U_d \sum_i n_{i\uparrow}^d n_{i\downarrow}^d$ in a Hartree-Fock approximation Zaanen and Gunnarson perform numerical simulations for supercells containing up to 10×10 elementary CuO_2 unit cells subject to periodic boundary conditions. For their numerics they chose $\Delta = t_{pd}$ and $U_d = 4t_{pd}$. At half filling (in the undoped case) the system is unstable towards the formation of a Néel state, which leads to a gap in the charge excitations spectrum. Having one excess hole per supercell, the self-localization is energetically favored compared to having an extended excess hole. A spin bag [91, 96] is found in the ground state. The ground states for 10 excess holes in a 9×10 and 10×10 supercell are shown in Fig. 5. As in the localized regime the majority of the charge is localized on the oxygen ions, while the spins reside mainly on the Cu sites. For both supercells 10 unit cells long charged domain walls are found. Due to the periodic boundary conditions the domain

line forms a ring in the quadratic supercell and a straight line in the non-quadratic one. Finally, having $2N$ holes in a $N \times N$ cell leads to two parallel lines repelling each other.

Almost at the same time similar calculations were performed by Schulz [92] for a single-band Hubbard model. With increasing on-site repulsion U , a transition from a vertical to a diagonal domain wall is found. The diagonal wall has been found to be stable at large U by Poilblanc and Rice [83].

1.4 Phenomenology of stripes

From the theoretical point of view one expects an instability towards the formation of a combined charge- and spin-density wave. Since the charge stripes act as anti-phase boundaries for the antiferromagnetic spin domains the period the magnetization is modulated with twice the period of the charge-density modulation (cf. Fig. 6).

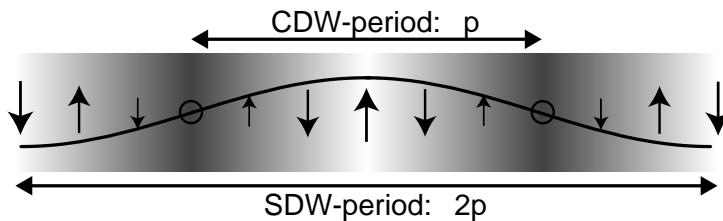


Figure 6: *Sketch of a combined charge- and spin-density wave. The arrows represent the magnetic or spin order, the gray levels of the background the local charge density. Dark regions correspond to a high concentration of charge carriers. The staggered magnetization is modulated with a period $2p$ where p is the period of the charge modulation.*

The first indications of long-period ('incommensurate') spin-density modulations were provided by inelastic neutron scattering studies [19] of superconducting LSCO, and by related measurements on the insulating LSNO analog [38], whereas the first experimental evidence for stripes as a *combined* spin- and charge-density wave phenomenon in LSCO codoped with Nd and LSNO was achieved by Tranquada and co-workers [101, 102]. The codoping in LSCO is necessary to slow down the stripe dynamics. To the present day, stripes have been observed in various nickelate and cuprate compounds over a wide doping range, suggesting that their formation in doped layered

perovskites is generic. The most direct evidence for stripes in doped antiferromagnets has come from neutron scattering studies.

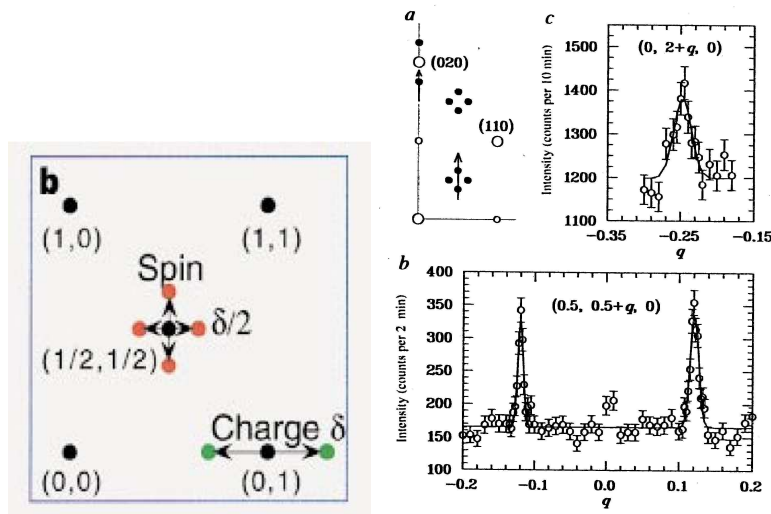


Figure 7: *Observation of static stripes via neutron scattering. Left: Location of the static superstructure peaks for vertical stripes. Wave vectors are measured in reciprocal lattice units. The magnetic Bragg peaks are shifted by $\delta/2$ from the AF wave vector, the charge peaks by δ from the reciprocal lattice positions (the $(1,0)$ position is shown as an example) indicating that the period of the spin modulation is twice that of the charge modulation [73]. Right: First experimental evidence of static stripes in LSCO codoped with Nd [102].*

Diffraction of a neutron beam by spin- and charge density modulations extending over a few unit cells (cf. Fig. 6) yields superstructure Bragg peaks. Their position measures the direction as well as the period of the corresponding density modulations. The intensity of the peaks provides a measure of the modulation amplitudes. Charge order is much harder to detect than spin order, since neutrons have no charge and do not scatter directly from the modulated electron density, but only from small displacements of the magnetic ions, which are caused by the modulation of the electron density. The lattice modulation is also measurable with electron and x-ray diffraction.

The positions of the Bragg superstructure peaks in the reciprocal space are illustrated in Fig. 7 for vertical stripes as observed in the superconducting

cuprates. While in the nickelates the stripes appear to be diagonal in general the orientation of the stripes in the cuprates changes from diagonal to vertical at the transition to the superconducting state [66, 108] (cf. Fig. 8). This reorientation of the stripes can probably be ascribed to the coupling to the superconducting order parameter which has a $d_{x^2-y^2}$ symmetry favoring a vertical orientation.

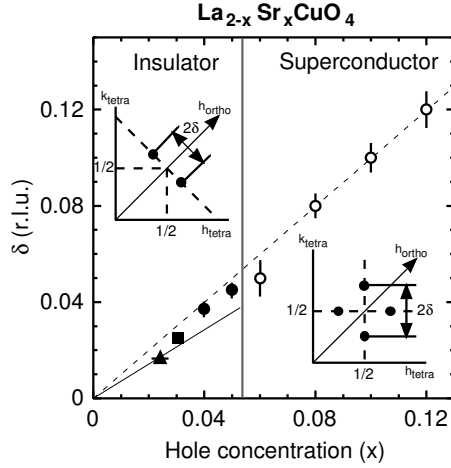


Figure 8: In LSCO the incommensurability δ (in this notation $\delta \rightarrow 2\delta$) equals the hole concentration x over a wide doping range [66]. At the superconducting transition the stripes reorientate from diagonal to vertical.

Although one expects the formation of a unidirectional charge- and spin-density wave, experimentally, a fourfold pattern of the superstructure peaks is observed (as illustrated for the magnetic Bragg peaks in Fig. 7). Either the picture of a unidirectional modulation is wrong or the fourfold symmetry is originated from stripes which are rotated by 90 degrees from layer to layer or results from twinning which is usually present in orthorhombic distorted crystals if stripes tend to orientate along a certain crystal axis. Experiments [71, 95, 94] in (partially) detwinned YBCO provide evidence for unidirectional order, i.e., that a fourfold pattern of incommensurate peaks near the antiferromagnetic wave vector $\mathbf{k}_{\text{AF}} = (1/2, 1/2)$ results only from the twinning. Stripes from different layer seem to be parallel and oriented along the direction of the oxygen chains in the adjacent planes. However, in other compounds the stripes from neighboring layers may be perpendicular to each other as suggested for the monolayer compound LSCO [102].

The magnitude δ of the charge-modulation wave vector in reciprocal lattice units is given by the ratio between the square-lattice spacing a and the stripe distance d , $\delta = a/d$. In the stripe community δ is usually referred as 'incommensurability'. In experiments stripe structures are most clearly seen if the ratio $p := 1/\delta = d/a$ is close to an integer value. For stripes (as for any density wave) one actually expects that integer values of p are energetically very stable due to a lock-in of the superstructure into the atomic structure. This pinning mechanism is considered as the origin of the so called '1/8 co-nundrum' in the cuprates [102], i.e., the stability of $p = 4$ over a considerable doping range.

In the nickelates the incommensurability δ equals the hole concentration x over a wide doping range, whereas in the cuprates the relation $\delta \approx 2x$ is observed (cf. Fig. 8). These observations and the stability of stripes for integer values p suggest a naive real-space picture of holes forming parallel site-centered rivers which are half filled in the cuprates and fully occupied in the nickelates (cf. Fig. 9).

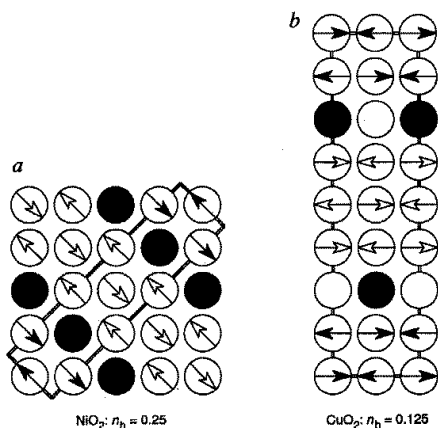


Figure 9: *Minimalistic real-space picture of diagonal stripes realized in the nickelates and vertical stripes as observed in the superconducting cuprates. The holes are assumed to form site centered rivers. The stripe spacing $p = 4$ corresponds to a doping of $x = 1/4$ in the case of the nickelates and $x = 1/8$ for the cuprates where the stripes are half filled (indicated by black and white circles) [102].*

1.5 Spin dynamics

The first indications of incommensurate stripe-like spin-density modulations at low energies were provided by inelastic neutron scattering studies of superconducting LSCO [19] and insulating LSNO [38]. Collective *low energy* excitations at satellite positions in the vicinity of the antiferromagnetic wave vector $\mathbf{k}_{AF} = (1/2, 1/2)$ had been observed.

To the present day the formation of stripes in layered nickelates and cuprate superconductors including the paradigmatic high- T_c compounds YBCO and BSCCO seems to be generic. Nevertheless, it is still an open question to what extent the stripe picture can account not only for the incommensurate spin fluctuations at low energies but also for magnetic excitations at a higher energy range including the π -resonance mode observed in various superconducting cuprates. The magnetic π -resonance peak centered commensurately on the antiferromagnetic wave vector is a collective mode well defined in both energy and momentum. So far, this resonance has been observed in YBCO [88, 33], BSCCO [50], and in the monolayer compound $Tl_2Ba_2CuO_{6+x}$ [41] suggesting that it is a universal feature of all cuprate superconductors. The fact that the π -resonant mode had not been detected in LSCO so far can possibly be ascribed to a larger effective strength of disorder due to substitutional doping.

In optimally doped YBCO the specific form of the dynamic magnetic response including the incommensurability and the π resonance gave rise to doubts that it could be consistent with the stripe model [12]. On the other hand Batista *et al.* [3] have explicitly proposed that the dispersive resonance represents the magnon like excitations emanating from incommensurate wave vectors associated with a stripe correlated spin system.

Indeed, the dispersion in LSNO and in underdoped cuprates supports this picture. The excitations are observed to disperse from each satellite up to a commensurate peak at \mathbf{k}_{AF} (cf. Fig. 10), which may be associated with the resonance peak. In LSNO the branches from $+\delta$ and $-\delta$ merge at \mathbf{k}_{AF} forming a single broad peak with additional weight coming from excitations associated with the orthogonal stripe domains [11]. A similar behavior is observed in underdoped LSCO [82]. However, on contrary to YBCO no sharp resonance is observed. For Sr doped samples the momentum broadening of the excitation peaks can be ascribed, at least in parts, to disorder effects which render spin-spin correlations finite [11]. In YBCO the response above the resonance energy is found to become incommensurate again. Such and

”x-shaped” dispersion in the vicinity of the resonance (cf. Fig. 10) has been observed explicitly in Refs. [10, 2, 31, 70].

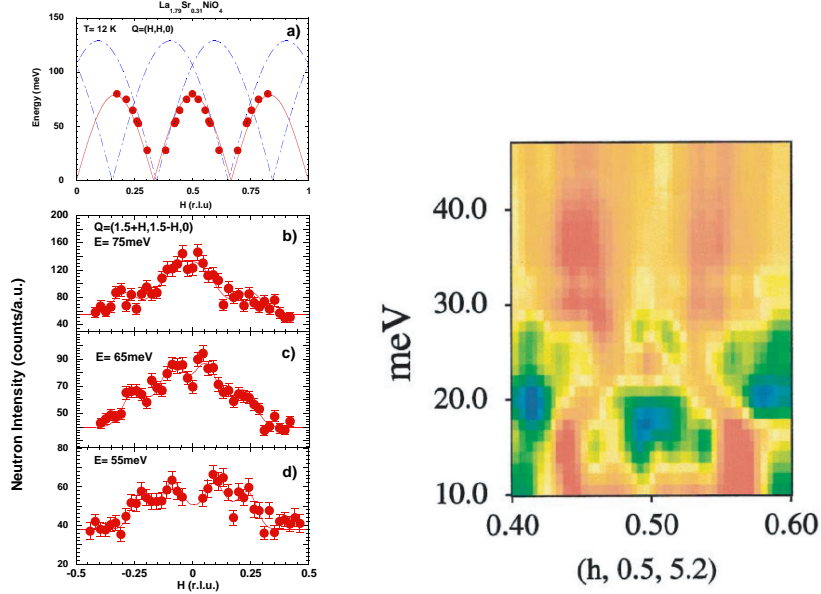


Figure 10: *Left: Neutron scattering data and fits from Bourges et al. [11] for $\text{La}_{1.69}\text{Sr}_{0.31}\text{NiO}_4$. The doping content corresponds to a stripe spacing $p = 1/x \approx 3$. In the upper panel the dispersion relation of the spin excitations is shown. The full line is a fit by a simple $|\sin(3\pi H)|$ function. The two dashed lines correspond to the spin-wave dispersion relation in undoped La_2NiO_4 , but shifted to the incommensurate wave vectors. Three selective constant energy scans are shown in the lower panels. At 75 meV the incommensurate branches begin to merge at \mathbf{k}_{AF} forming a single broad peak. Right: Magnetic scattering distribution in the odd channel for underdoped YBCO6.35 along the $(H, 1/2)$ direction [70]. A small π resonance at \mathbf{k}_{AF} can be observed at 23 meV. The intense incommensurate scattering between 12 and 17 meV is consistent with a stripe spacing $p = 8$. In the vicinity of the resonance the dispersion is found to be x-shaped.*

The apparent inconsistency between the stripe picture and the magnetic excitations observed in YBCO near optimum doping was only resolved recently. In neutron scattering studies of optimally doped, stripe-ordered $\text{La}_{1.875}\text{Ba}_{0.125}\text{CuO}_4$ [103] a spectrum quite similar to that of optimally doped YBCO [12, 86] has been measured. Only the low-energy excitations behave

similarly to spin waves whereas with increasing energy significant deviations to what is naively expected for a material with stripes [3, 46] become apparent. Tranquada *et al.* [103] have suggested that even the high-energy response can be understood in terms of a stripe picture in which quantum excitations beyond spin waves have to be taken into account. At high energies the excitations are found to be very similar to spin-1 excitations of isolated spin ladders [103]. Very recently, Uhrig *et al.* [105] derived a unified picture of the experimental observation of low-energy magnons around the superstructure satellites and of the triplon excitations at higher energies. Their analysis is based on a two-dimensional model of coupled two-leg spin ladders. Including a relatively strong cyclic exchange they find a very satisfying overall agreement to the scattering data of stripe-ordered $\text{La}_{1.875}\text{Ba}_{0.125}\text{CuO}_4$ [103]. Qualitatively similar results are obtained by a mean-field analysis of coupled dimers in a bond-centered stripe state [107].

In the underdoped regime the stripe spacing will become larger upon decreasing doping [66] (cf. Fig. 8), which on the one hand moves the ordering wave vectors closer to \mathbf{k}_{AF} and lowers the energy of the resonance peak. On the other hand the hole-poor regions become wider, which stabilizes magnetic order, thus reducing dimerization and quantum effects. Therefore, for small doping one can expect the semi classical spin-wave approach [3, 46] to be more appropriate for the whole energy range.

In the nickelates, a spin-wave picture at higher energies is more justified due to the larger spin $S = 1$. Furthermore, compared to the cuprates the effective spin couplings across the charge stripes are relatively strong in the nickelates [56] leading to a stabilization of magnetic order.

2 Outline

In this thesis we study fluctuations of spin and charge in stripe phases, which are a universal feature of doped layered cuprate and nickelate compounds.

In part II of this thesis we study the interplay of topological excitations in stripe phases: charge dislocations, charge loops, and spin vortices. Since these defects interact logarithmically on large distances in two dimensions they resemble a Coulomb gas of topological charges. Using a renormalization-group analysis in this Coulomb-gas representation, we calculate the mutual screening of the defects and establish the phase diagram. The transitions are driven by the unbinding of the topological defects similar to the Kosterlitz-Thouless transition where the order is destroyed by the proliferation of vortices or to the melting of two dimensional crystals which is mediated by the unbinding of dislocations. Although the physics of defect-mediated melting is well known for almost thirty years, the relation to stripe systems is delicate because of the interplay of spin and charge order. Since the charge stripes act as anti-phase domain boundaries for the spins a single dislocation (an ending domain wall) entails a half vortex like spin texture. Depending on which types of defects proliferate we identify four different phases which are characterized by the range of spin order, charge order, and a less accessible collinear order. These orders can disappear at a single transition or in a sequence of two transitions. The scenario is determined by the ratio of the spin- and charge-stiffness constants. The phenomenon of spin-charge separation is observed experimentally, the charge ordering of stripes is always observed at a higher temperature than the magnetic ordering [102, 79, 45, 100, 59, 113] (cf. Fig. 8). Further on, we calculate the critical properties of the phase transitions. The phases are separated by transition lines along which the correlation functions decay with non-universal, continuously varying critical exponents. Slightly above the temperature T^{crit} of the transition out of the ordered low-temperature phase, the short-ranged orders have a correlation length $\xi \sim \exp(\lambda(T - T^{crit})^{-\nu})$ characteristic for defect-mediated melting. Along the phase boundary to the ordered phase ν behaves discontinuously. We find $\nu = 1/2$ (as for the usual KT-transition) except for the points where three phases coexist. There the exponent jumps to a smaller value reflecting the balanced competition of two types of defects at the special points.

In part III the spin dynamics of stripes in high-temperature superconductors and related compounds is studied in the framework of a spin-wave theory for a simple spin-only model. The starting point for a suitable parameter-

ized Heisenberg model is the naive real-space picture (cf. Fig. 9) motivated in the introduction. The holes are assumed to form parallel site-centered rivers of one lattice spacing wide which act as anti-phase domain walls for the antiferromagnetically coupled spins. We choose the simplest possible implementation of exchange couplings stabilizing this magnetic structure: antiferromagnetic exchange couplings J between neighboring spins within the domains and antiferromagnetic couplings λJ between closest spins across a stripe. Assuming that J should be comparable to the exchange coupling in the undoped material, the relative coupling strength λ is the only a priori unknown model parameter. Of course, such a minimalistic spin-only model does not fully account for electronic correlations. In particular, a possible spin gap at very low energies due to the formation of Cooper pairs is not incorporated in our model. Nevertheless, one can expect an adequate description of the spin fluctuations well above the gap energy. This energy range also includes the π -resonance energy. Of course, our spin-wave approach has its limitations also at higher energies where excitations beyond magnons may become relevant as observed in superconducting cuprates near optimum doping.

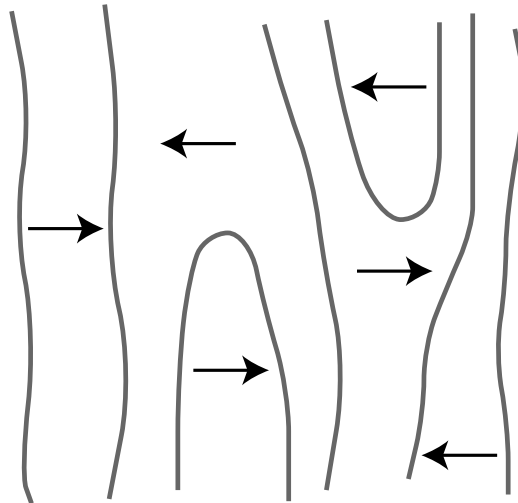
In the first instance we focus on a single layer motivated by the weakly coupled layered structure of the materials. The magnon dispersion relation and the magnetic zero-temperature structure factor are calculated whereby acoustical as well as optical bands are included in the analysis. We distinguish between diagonal stripes as observed in the nickelates and non-superconducting cuprates and vertical stripes present in the superconducting cuprate compounds. The incommensurability and the π resonance appear as complementary features of the band structure at different energy scales. The dependence of spin-wave velocities and resonance frequencies on the stripe spacing and coupling is calculated. At low doping, the resonance frequency is found to scale inversely proportional to the stripe spacing. Since the overall agreement with experimental observations is relatively satisfying we conclude that the spin-only model provides an adequate and simple basis for calculating and understanding the spin dynamics of stripes.

Eventually we extend our basic model to a bilayer considering a vertical stripe orientation realized in $\text{YBa}_2\text{Cu}_3\text{O}_{6+x}$, a compound in which the layers are grouped to closed and strongly coupled pairs. Again, the magnetic spectral properties are calculated in linear spin-wave theory. We consider several stripe configurations which differ by the relative location of the stripes in the layers. We focus on the bilayer splitting of the magnon bands near the in-

commensurate low energy peaks as well as in the vicinity of the π resonance, distinguishing between the odd and even channel. We find that an x-shaped dispersion near the π resonance is generic for stripes. By comparison of our results to neutron scattering data for $\text{YBa}_2\text{Cu}_3\text{O}_{6+x}$, we conclude that the stripe model is consistent with characteristic features of bilayer high- T_c compounds.

Part II

Ordering of spin and charge in stripe phases



1 Introduction

Layered copper oxide high- T_c compounds fascinate not only because of superconductivity but also because of a variety of concurring orders. In particular, theoretical [92, 116, 28, 63] and experimental [19, 65, 38, 18] evidence has been found for stripes. Holes which are induced by doping condense into arrays of parallel rivers in the CuO_2 layers. Within a layer, each river acts as a boundary between antiferromagnetic domains with opposite sublattice magnetization. Thus, stripes are a combined charge- and spin-density wave phenomenon.

Based on charge density and magnetization as order parameters, it is instructive to analyze the interplay of orders in the framework of a Landau theory [120]. However, in low dimensional structures fluctuations can be crucial for the nature of phases and of phase transitions. In particular, fluctuations play a central role (i) for spin-charge separation, i.e., the phenomenon that charge order emerges at higher temperatures than spin order (as observed in cuprates [102, 79, 45] as well as in nickelates [100, 59, 113]) and (ii) for the anomalous properties of the cuprates near optimum doping [98]. To account for collective low-energy excitations of the electronic system, continuous deformations of perfect stripe order (spin waves or smooth stripe displacements) as well as topological defects (such as dislocations, vortices, or skyrmions) must be considered. The latter were found to induce transitions between various liquid-crystal like electronic phases [52]. Besides transitions which are related to a degradation of the charge and spin structure factors, Zaanen *et al.* [117] have suggested a further transition characterized by a less accessible, intrinsically topological order.

In the following we present a paradigmatic model which is amenable to a largely analytical analysis of the interplay between charge and spin orders. Motivated by the weakly coupled layered structure of the materials, we restrict our analysis to two dimensions. Since the relevant materials typically have a planar spin anisotropy, the out-of-plane component of the spins is neglected. Assuming quantum fluctuations to be weak in comparison to thermal fluctuations we treat all degrees of freedom classically. The stripe melting mediated by the unbinding of three classes of topological point defects, namely charge dislocations, charge loops, and spin vortices is investigated. In the framework of a renormalization-group approach we establish the phase diagram and determine the nature of the phase transitions.

The outline of this chapter is as follows: in section 2 the model is worked

out. The collective low-energy excitations are introduced, on the one hand smooth stripe displacements and slowly varying spin Goldstone modes representing wave-like excitations, on the other hand the excitations of three classes of topological defects: dislocations, charge loops and vortices. The phase transitions are driven by the unbinding of these defects. To characterize the nature of the phases we introduce, in addition to the spin and charge density correlation functions, a correlation function measuring the collinearity of the spins. The dependence of these correlation functions on the spin and charge stiffness constants in the absence of topological defects is calculated. Finally, the Coulomb-gas representation of the interacting topological defects is motivated. In section 3 a qualitative picture of the phase diagram obtained by a simple heuristic argument is presented. In section 4 we incorporate the mutual screening of the defects in the framework of a renormalization-group analysis in the Coulomb-gas representation of the topological charges. Flow equations for the stiffness constants and the fugacities arising from additional core energies of the defects are derived. After a brief review of the usual Kosterlitz-Thouless transition in section 5 the phase diagram and the critical properties of the phase transitions are determined by a numerical integration of the flow equations in section 6. Finally, in section 7 we discuss the relation of our findings to experimental observations.

2 Model

We start to establish a paradigmatic model which allows for a largely analytical analysis of the interplay between charge and spin orders and provides several scenarios of spin-charge separation. As motivated in the introduction we treat all degrees of freedom as classical, restrict our analysis to two dimensions, and neglect the out-of-plane components of the spins.

2.1 The ground state

We assume that the stripes are parallel to the the y -direction with a spacing d . In the ground state the charge density is modulated with a wave vector $\mathbf{q} = (2\pi/d, 0)$. To implement that the charge stripes are anti-phase domain boundaries for the antiferromagnetically coupled spins, it is useful to label the domains by a step function which increases by 2π across a stripe located at $x = nd, n \in \mathbb{Z}$ (cf. Fig. 11).

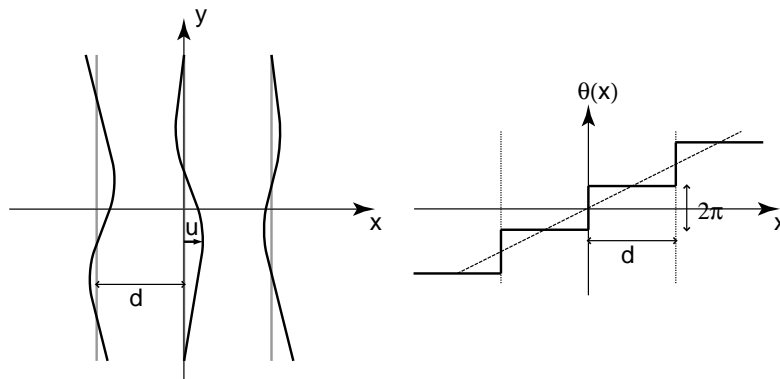


Figure 11: *Left: Smooth conformations of the charge stripes, described by a single valued displacement field $\mathbf{u}(\mathbf{r}) = \{u(\mathbf{r}), 0\}$ from the ground-state configuration (straight grey lines). In the ground state the stripes are located at $x = nd, n \in \mathbb{Z}$. Right: Step function $\theta(x)$ labelling the inter-stripe domains in the ground state. The function increases by 2π across a stripe.*

Rewriting the periodic seesaw function $\theta(\mathbf{r}) - \mathbf{q} \cdot \mathbf{r}$ as a Fourier series, the step function illustrated in Fig. 11 is given by

$$\theta(\mathbf{r}) = \mathbf{q} \cdot \mathbf{r} + \sum_{m \neq 0} \frac{1}{im} e^{im\mathbf{q} \cdot \mathbf{r}}. \quad (3)$$

Using this step function, the charge density in the ground state can be expressed as

$$\rho_0(\mathbf{r}) = \frac{\lambda}{2\pi} \partial_x \theta(\mathbf{r}), \quad (4)$$

where λ denotes the charge per unit length per stripe. Since we treat spins as classical two-component vectors with fixed length S we can parameterize them by an angle field $\Phi(\mathbf{r})$,

$$\vec{S}(\mathbf{r}) = S\{\cos \Phi(\mathbf{r}), \sin \Phi(\mathbf{r})\}. \quad (5)$$

The magnetization of the ground state, including the modulation by the antiferromagnetic order within the domains and by the anti-phase boundary condition on the stripes is captured by Eq.(5) with an angle field

$$\Phi(\mathbf{r}) = \mathbf{Q} \cdot \mathbf{r} + \theta(\mathbf{r})/2. \quad (6)$$

Here $\mathbf{Q} = (\pi/a, \pi/a)$ is the antiferromagnetic wave vector, where a denotes the spacing of the square lattice which the spins populate.

2.2 Wave-like low energy excitations

First of all we want to consider wave-like excitations of the ground state, namely smooth stripe conformations and spin rotations. The stripe conformations can be described by a single-valued displacement field $\mathbf{u}(\mathbf{r}) = \{u(\mathbf{r}), 0\}$ (cf. Fig. 11). Since the deformation of the stripes causes a deformation of the antiferromagnetic domains in between, the argument of the step function has to be shifted by the displacement field. Therefore we generalize the step function introduced in Section 2.1,

$$\theta(\mathbf{r}) = \mathbf{q} \cdot [\mathbf{r} - \mathbf{u}(\mathbf{r})] + \sum_{m \neq 0} \frac{1}{im} e^{im\mathbf{q} \cdot [\mathbf{r} - \mathbf{u}(\mathbf{r})]}. \quad (7)$$

This function increases by 2π across the deformed stripes. Of course, using this deformed step function, the charge density $\rho(\mathbf{r})$ of the excited state is still given by Eq.(4). Including spin Goldstone modes represented by an angle field $\phi(\mathbf{r})$ the phase field of the spins is given by

$$\Phi(\mathbf{r}) = \mathbf{Q} \cdot \mathbf{r} + \theta(\mathbf{r})/2 + \phi(\mathbf{r}). \quad (8)$$

The angle ϕ describes smoothly varying deformations of the spin ground state in the presence of deformed charge stripes. In the absence of topological defects low-energy excitations are wave-like and, in a continuum description, governed by the Hamiltonian

$$H_{\text{wave}} = \frac{1}{2} \int d^2r \left\{ J_s (\nabla\phi)^2 + J_c (2\pi/d)^2 (\nabla u)^2 \right\} \quad (9)$$

with phenomenological spin and charge stiffness constants J_α (with $\alpha = s, c$, respectively).

2.3 Charge order, spin order, and collinear order

Charge and spin order (CO,SO) are measured by the charge-density correlation function $\mathcal{C}_\rho(\mathbf{r}) = \langle \delta\rho(\mathbf{r})\delta\rho(\mathbf{0}) \rangle$, where $\delta\rho(\mathbf{r}) = \rho(\mathbf{r}) - \rho_0(\mathbf{r})$ denotes the modulation of the charge density with respect to the ground state, and the spin correlation function $\mathcal{C}_\sigma(\mathbf{r}) = \langle \vec{\sigma}(\mathbf{r}) \cdot \vec{\sigma}(\mathbf{0}) \rangle$ with $\vec{\sigma}(\mathbf{r}) := \vec{S}(\mathbf{r})/S$. In the absence of topological defects where the low energy excitations are governed by H_{wave} (9) both orders are quasi-long ranged, the correlation functions decay algebraically on large scales,

$$\mathcal{C}_\rho(\mathbf{r}) = \langle \delta\rho(\mathbf{r})\delta\rho(\mathbf{0}) \rangle \stackrel{|\mathbf{r}| \rightarrow \infty}{\sim} \cos(\mathbf{q}\mathbf{r}) \cdot |\mathbf{r}|^{-\eta_\rho}, \quad (10)$$

$$\mathcal{C}_\sigma(\mathbf{r}) = \langle \vec{\sigma}(\mathbf{r}) \cdot \vec{\sigma}(\mathbf{0}) \rangle \stackrel{|\mathbf{r}| \rightarrow \infty}{\sim} \cos[(\mathbf{Q} + \frac{\mathbf{q}}{2})\mathbf{r}] \cdot |\mathbf{r}|^{-\eta_\sigma}, \quad (11)$$

where the exponents depend on the temperature reduced stiffness constants $K_\alpha = J_\alpha/T$ due to

$$\eta_\rho = \frac{1}{2\pi K_c}, \quad (12)$$

$$\eta_\sigma = \frac{1}{2\pi K_s} + \frac{1}{8\pi K_c}. \quad (13)$$

The correlation functions are explicitly calculated in appendix A. Their algebraic decay is characteristic for the spatial dimension $D = 2$. For $D > 2$ the order remains long-ranged, the correlations are independent of the distance on large scales and just reduced by thermal fluctuations. At the lower critical dimension $D = 2$ the order parameters are suppressed by thermal

fluctuations and the correlation functions decay algebraically with distance on large scales, the orders are called quasi-long ranged. This is the phenomenon of fluctuation destruction of long range order (LRO). The absence of LRO in two-dimensional systems with a continuous symmetry (e.g., the global rotation of all spins) is often referred as the Mermin-Wagner theorem [69]. In $D = 1$ the orders are rendered short ranged by thermal fluctuations, the correlation functions decay exponentially with distance.

The dependence of the exponent η_σ on the charge stiffness K_c reflects that fluctuations of the charge stripes cause fluctuations of the spins since the stripes act like anti-phase domain boundaries. A correlation function depending only on the spin stiffness K_s but not on K_c should measure the spin collinearity since this quantity is not affected by smooth stripe deformations. Such a *collinear order* (LO) can be measured by the correlation function

$$\mathcal{C}_\parallel(\mathbf{r}) = 2\langle[\vec{\sigma}(\mathbf{r})\vec{\sigma}(\mathbf{0})]^2\rangle - 1. \quad (14)$$

In the absence of topological defects the asymptotic behavior of this correlation function (see Appendix A) is given by

$$\mathcal{C}_\parallel(\mathbf{r}) \stackrel{|\mathbf{r}|\rightarrow\infty}{\sim} \cos(2\mathbf{Q}\mathbf{r}) \cdot |\mathbf{r}|^{-\eta_\parallel}, \quad (15)$$

$$\eta_\parallel = \frac{2}{\pi K_s}. \quad (16)$$

2.4 Topological defects

Before we introduce the relevant topological defects in the stripe system we briefly discuss the topological excitations in the spin and charge sector separately.

2.4.1 Vortices

The XY-spins $\vec{S}(\mathbf{r}) = S\{\cos\phi(\mathbf{r}), \sin\phi(\mathbf{r})\} = Se^{i\phi(\mathbf{r})}$ are 2π -periodic functions of the angle field $\phi(\mathbf{r})$. A vortex is a point singularity of the phase field $\phi(\mathbf{r})$ characterized by the phase of the spins going continuously through a multiple of 2π as we go round a contour enclosing the vortex,

$$\oint_\gamma \nabla\phi = 2\pi m, \quad m \in \mathbb{Z}. \quad (17)$$

If the contour γ is orientated anticlockwise, m is called the *winding number* or the *topological charge* of the vortex. To minimize the elastic energy, the Laplace equation $\nabla^2\phi(\mathbf{r}) = 0$ has to be fulfilled for all $\mathbf{r} \neq \mathbf{r}_0$ where \mathbf{r}_0 is the position of the vortex core. For $\mathbf{r}_0 = \mathbf{0}$ one solution of the Laplace equation with respect to the topological constraint (17) is given by $\phi(x, y) = m \arctan(y/x)$. Using this solution the elastic energy of a single vortex is easily calculated:

$$\begin{aligned} E_v &= \frac{1}{2} J_s \int d^2r (\nabla\phi)^2 = \pi J_s m^2 \int_{a_0}^R \frac{r dr}{r^2} \\ &= \pi J_s m^2 \ln(R/a_0), \end{aligned} \quad (18)$$

where a_0 is the *core radius* and R the linear dimension of the sample. The energy of a single vortex diverges logarithmically with the system size. Nevertheless a vortex is topologically stable since it cannot be made to disappear by a continuous deformation of the spins, it is a *topological defect*. In Fig. 12 possible spin configurations for single $m = \pm 1$ vortices as well as for a neutral vortex pair are shown. Far from a pair of vortices with opposite winding numbers the spins are nearly parallel and the far-field configuration can be transformed continuously to the uniform state. Furthermore, continuous distortions can bring the vortices together and cause them to annihilate. Therefore, a neutral vortex pair is topologically equivalent to the uniform state and represents an important excitation from the ground state.

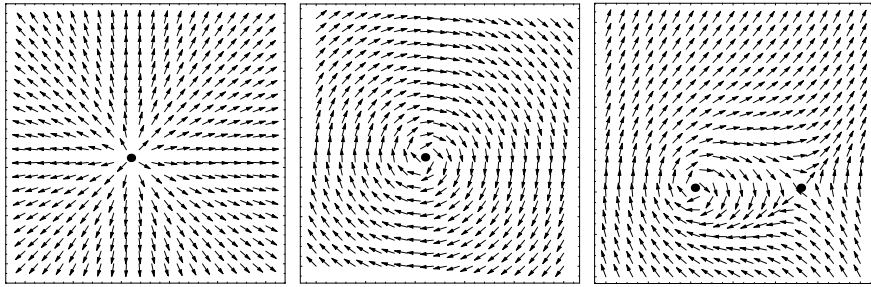


Figure 12: Possible configurations of the staggered magnetization for isolated vortices with topological charges $m = 1$ (left) and $m = -1$ (middle), and for a pair of single charged vortices with opposite winding numbers (right). The cores of the vortices are denoted by thick points.

We now consider an arbitrary number of vortices at positions \mathbf{r}_i with topological charges m_i . Since only excitations of neutral pairs or clusters should be considered, the constraint of charge neutrality of the system has to be fulfilled, $\sum_i m_i = 0$. For abbreviation we write $\mathbf{v} = \nabla\phi$. Assuming that the defects are enclosed by a contour Γ and let A be the orientated area in the xy-plane defined by $\partial A = \Gamma$, we have

$$2\pi \sum_i m_i = \oint_{\Gamma=\partial A} \mathbf{v} \cdot d\mathbf{l} = \int_A \nabla \times \mathbf{v} \cdot d\mathbf{A}. \quad (19)$$

Since the vector $d\mathbf{A}$ is perpendicular to the xy-plane, the source function $\mathbf{J} := \nabla \times \mathbf{v}$ can be expressed by the vortex density $n(\mathbf{r}) = \sum_i m_i \delta(\mathbf{r} - \mathbf{r}_i)$ due to $\mathbf{J}(\mathbf{r}) = 2\pi \mathbf{e}_z n(\mathbf{r})$. With $\nabla \cdot \mathbf{v} = 0$ it follows that $\nabla \times \mathbf{J} = -\nabla^2 \mathbf{v}$ and therefore

$$\mathbf{v} = -\nabla \times \int d^2r \mathcal{G}(\mathbf{r} - \mathbf{r}') \mathbf{J}(\mathbf{r}'), \quad (20)$$

while the 2D-Green function \mathcal{G} satisfies $\nabla^2 \mathcal{G}(\mathbf{r}, \mathbf{r}') = \delta(\mathbf{r} - \mathbf{r}')$. Using Eq.(20) we rewrite the energy of the vortex system,

$$\begin{aligned} H_v &= \frac{1}{2} J_s \int d^2r \mathbf{v}^2(\mathbf{r}) \\ &= \frac{1}{2} (2\pi)^2 J_s \int d^2r \int d^2r' n(\mathbf{r}) \mathcal{G}(\mathbf{r}, \mathbf{r}') n(\mathbf{r}'). \end{aligned} \quad (21)$$

For $|\mathbf{r} - \mathbf{r}'|$ large and both points far from boundaries, we have

$$\mathcal{G}(\mathbf{r}, \mathbf{r}') = \frac{1}{2\pi} \ln \left(\frac{|\mathbf{r} - \mathbf{r}'|}{a_0} \right) + \frac{C}{2\pi}, \quad (22)$$

where a_0 is an ultraviolet cutoff of order the vortex diameter and C is a constant associated with the core energy. For quantitative purposes one is supposed to use the Green function on a two-dimensional square lattice. Nevertheless, replacing a_0 by the lattice constant and using $C = \gamma + \frac{1}{2} \ln 8$ with Euler's constant γ , the Green function defined in Eq.(22) is an excellent approximation of the square-lattice Green function for all $|\mathbf{r} - \mathbf{r}'| \geq a_0$ [55, 53]. Inserting the Green function and using the charge neutrality we rewrite the vortex Hamiltonian (21)

$$H_v = -\pi J_s \sum_{i \neq j} m_i m_j \ln \left(\frac{|\mathbf{r}_i - \mathbf{r}_j|}{a_0} \right) + E_c \sum_i m_i^2, \quad (23)$$

with a *core energy* $E_c = \pi C J_s$. Apart from the core contribution, H_v is identical to the Hamiltonian of a two-dimensional Coulomb gas with point charges m_i located at \mathbf{r}_i .

2.4.2 Dislocations

Defects associated with the continuum elastic theory of solids are dislocations and disclinations [76]. Dislocations are characterized by a *Burgers vector* \mathbf{b} , defined as the amount by which a contour integral of the displacement field $\mathbf{u}(\mathbf{r})$ around the dislocation fails to close. The Burgers vector must itself be a vector from the underlying lattice. Similar to vortices, dislocations in two-dimensional crystals interact logarithmically on large scales what can be worked out just as in the case of vortices (see, for example, Ref. [78]). Therefore, one might expect that the unbinding of neutral dislocation pairs drives a finite-temperature transition directly from a solid to a liquid [5, 6, 54, 55]. In fact, the physics of defect-mediated melting of two dimensional crystals [78, 36, 114] is similar to that of the Kosterlitz-Thouless (KT) vortex-unbinding transition. However, dislocations are characterized by vector charges \mathbf{b} on contrary to vortices leading to different critical exponents, which depend on the geometry of the lattice.

Disclinations, which are also characterized by a conserved topological charge, have a much higher energy than dislocations and were neglected in the early work by Kosterlitz and Thouless [54, 55] and others [78, 36, 114].

Since in the case of the underlying line lattice of the charge stripes the displacement field $\mathbf{u}(\mathbf{r}) = \{u(\mathbf{r}), 0\}$ is single valued (the stripes are orientated along the y -direction), all possible Burgers vectors characterizing the dislocations point in the x -direction, $\mathbf{b} = m d \mathbf{e}_x$ with $m \in \mathbb{Z}$ and stripe spacing d (cf. Fig. 13). Therefore, in this simple situation dislocations can be characterized by scalar topological charges m . Their interaction is captured by the Coulomb-gas Hamiltonian (23) with the spin stiffness replaced by the charge stiffness J_c .

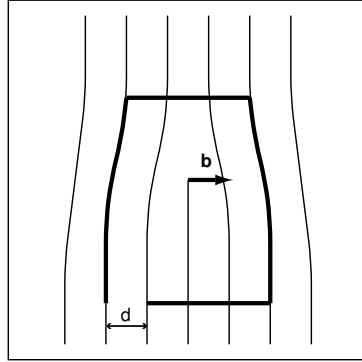


Figure 13: *Schematic representation of a single dislocation of charge stripes with spacing d . The Burgers circuit and the corresponding Burgers vector \mathbf{b} defined as the amount by which a contour integral of the displacement field around the dislocation fails to close are shown.*

2.4.3 Topological defects in stripes

In stripe systems the situation is more delicate because of the interplay between spin and charge order. Since charge stripes act as anti-phase domain boundaries, a single stripe *dislocation* (cf. Fig. 13) always entails a half-vortex like spin texture. Therefore, dislocations are combined defects interacting in both, the charge and the spin sector. We consider three types of topological defects (cf. Fig. 14), single stripe *dislocations*, charge *loops* (with a Burgers vector of two stripe spacings), and entire *vortices* [117].

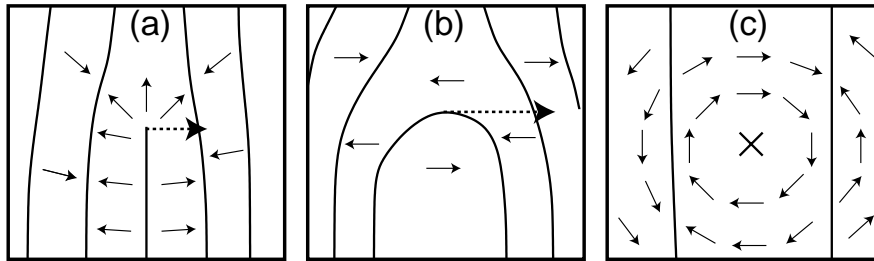


Figure 14: *Different types of topological defects in the charge density (lines) and sublattice magnetization (bold arrows). (a) Combination of a stripe dislocation (dashed arrows correspond with the Burgers vectors) and a half-vortex, (b) a charge loop, and (c) a vortex.*

Vortices as well as dislocations interact, in two dimensions, logarithmically on large scales. Therefore, apart from additional core contributions they resemble two dimensional Coulomb gases of topological point charges, namely the winding numbers of the vortices or Burgers vectors of the dislocations. For the stripe system charge and spin defects cannot be treated separately since dislocations are topological defects in both sectors simultaneously, a dislocation of a stripe is always combined with a half vortex in the spin sector. Therefore we classify a defect at position \mathbf{r}_i by its topological *vector charge* $\mathbf{m}_i = (m_{is}, m_{ic})$ and capture the interaction of the defects in a vector-Coulomb-gas formulation,

$$H_{\text{top}}/T = - \sum_{i \neq j} \sum_{\alpha=s,c} \pi K_{\alpha} m_{i\alpha} m_{j\alpha} \ln \left(\frac{|\mathbf{r}_i - \mathbf{r}_j|}{a_0} \right). \quad (24)$$

Additional core energies of such vector charges give rise to bare fugacities $y[\mathbf{m}] \equiv \exp\{-\pi C(K_s m_s^2 + K_c m_c^2)\}$, where C is a constant of order unity introduced in Eq.(22). Vortices have a vector charge $(m_s, m_c) = (\pm 1, 0)$ and a fugacity $y_v = \exp(-\pi C K_s)$, and loops are characterized by $(m_s, m_c) = (0, \pm 2)$ and $y_l = \exp(-4\pi C K_c)$. Dislocations have vector charges $|m_c| = 1$ and $|m_s| = \frac{1}{2}$ and fugacities $y_d = \exp\{-\pi C(K_c + K_s/4)\}$. Defects of higher charges are negligible for the critical aspects of the phase diagram.

3 Qualitative understanding of the phase diagram

In analogy to the KT transition [55, 53] the presence of topological defects effects a screening of the stiffness constant and phase transitions are driven by the unbinding of neutral defect clusters. Depending on which type of defects proliferates one or both stiffness constants are renormalized to zero and different phases characterized by the range of charge order (CO), spin order (SO), and collinear order (LO) can be identified. A qualitative understanding of the phase diagram can already be obtained by using a simple heuristic argument due to Kosterlitz and Thouless [55]. The energy of a single defect with vector charge $\mathbf{m} = (m_s, m_c)$ in a sample of linear dimension R is

$$E = \pi \sum_{\alpha=s,c} J_\alpha m_\alpha^2 \ln \left(\frac{R}{a_0} \right), \quad (25)$$

where a_0 is the short distance cutoff of order the core radius. The core can, of course, be anywhere in the sample. It therefore carries an entropy $S = \ln(R/a_0)^2$. Thus, the free energy of the system with a single defect with charge \mathbf{m} is

$$F = E - TS = \left(\pi \sum_{\alpha=s,c} J_\alpha m_\alpha^2 - 2T \right) \ln \left(\frac{R}{a_0} \right). \quad (26)$$

If $F > 0$ no isolated defects with charge \mathbf{m} are present, whereas for $F < 0$ the free energy of the system is minimized if neutral defect clusters unbind and the defects with charge \mathbf{m} proliferate. To be specific, vortices would proliferate for $\pi K_s < 2$, loops for $\pi K_c < \frac{1}{2}$, and dislocations for $\pi(K_c + K_s/4) < 2$. These barriers are shown in Fig. 15. Four phases can be identified. In phase I no free defects are present, SO, CO, and LO remain quasi-long ranged. In phase II vortices unbind as the only type of defect leading to a destruction of SO and LO, whereas CO is not affected. In phase III loops proliferate, while the other defects remain bound in clusters of neutral charge. The unbinding of loops renders SO and CO short-ranged, whereas the sublattice magnetization remains well defined, LO is preserved. Finally, in phase IV the existence of free dislocations leads to a destruction of all orders.

Although this simple argument leads to a qualitative understanding of the phase diagram, the precise shape of the phase boundaries cannot be

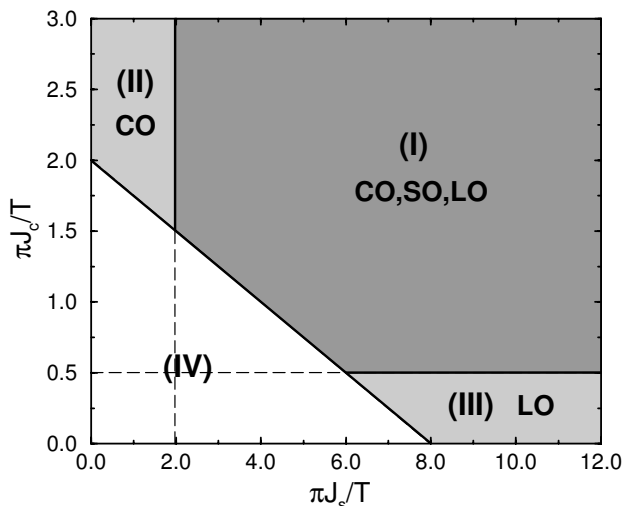


Figure 15: *Qualitative phase diagram obtained from the estimation of the free energies of the single defects. Phase I has no free defects and therefore CO, SO, and LO exist. In phase II, vortices proliferate and destroy SO and LO. In phase III, free loops are present, destroying CO and SO. Eventually, all orders are absent in phase IV since dislocations proliferate.*

obtained, since the argument neglects the interaction of defects as well as the screening of the stiffness constants by neutral defect clusters. However, performing a renormalization of the vector-Coulomb gas we will see that the straight lines separating the 'phases' correspond to zero fugacity fixed point lines of fully renormalized stiffness constants.

To distinguish phase III where loops proliferate as the only type of defect from the disordered phase IV the consideration of LO characterized by the correlation function \mathcal{C}_{\parallel} is necessary. Alternatively, Zaanen *et al.* [118, 117] have suggested a highly nonlocal correlation function involving spin *and* charge, which measures the sublattice magnetization as an intrinsic \mathbb{Z}_2 degree of freedom.

4 Renormalization

To incorporate the mutual screening of the defects we perform a renormalization group analysis in the vector-Coulomb-gas representation (24) of the topological charges. We follow the renormalization approach developed by Kosterlitz and Thouless [55, 53] for the usual scalar Coulomb gas which was generalized to vector gases in the context of 2D melting [78, 36, 114] or for random phase shift xy-models using replica representation [13, 15]. Here we present only the basic ideas of the renormalization procedure the detailed calculations are presented in Appendix B.

The charges are assigned a hard-core cutoff a_0 which is increased to $\tilde{a}_0 = a_0 e^{dl}$ under an infinitesimal coarse graining. Thereby, pairs of vector charges \mathbf{m}_i and \mathbf{m}_j with distance $a_0 \leq |\mathbf{r}_i - \mathbf{r}_j| \leq \tilde{a}_0$ annihilate each other if they have opposite charges, otherwise they recombine to a single non-vanishing vector charge $\mathbf{m} = \mathbf{m}_i + \mathbf{m}_j$ at position $\mathbf{R} = (\mathbf{r}_i + \mathbf{r}_j)/2$. For example, a pair of a dislocation $(1/2, -1)$ and a loop $(0, 2)$ at a scale a_0 is substituted by a dislocation $(1/2, 1)$, two dislocations $(1/2, 1)$ and $(-1/2, 1)$ would recombine into a loop $(0, 2)$. Under the coarse-graining procedure the functional form of the partition function is preserved and scale dependent stiffness constants and fugacities can be identified. The scale dependence of this parameters is controlled by the flow equations

$$\frac{dK_s^{-1}}{dl} = 2\pi^3(2y_v^2 + y_d^2), \quad (27a)$$

$$\frac{dK_c^{-1}}{dl} = 8\pi^3(2y_l^2 + y_d^2), \quad (27b)$$

$$\frac{dy_v}{dl} = (2 - \pi K_s)y_v + 2\pi y_d^2, \quad (27c)$$

$$\frac{dy_l}{dl} = (2 - 4\pi K_c)y_l + 2\pi y_d^2, \quad (27d)$$

$$\frac{dy_d}{dl} = \left(2 - \frac{\pi}{4}(K_s + 4K_c)\right)y_d + 2\pi(y_v + y_l)y_d, \quad (27e)$$

which are invariant under the mapping $(4K_c, K_s, y_l, y_v) \rightarrow (K_s, 4K_c, y_v, y_l)$. The flow equations are only valid for small temperatures since in the renormalization procedure the fugacities are assumed to be small, or in other words, the gas is assumed to be diluted. Annihilation or fusion processes of three or more closely spaced defects are neglected.

5 Short review of the KT-transition

We briefly discuss the flow of the KT equations controlling the scale dependence of the spin stiffness and the vortex fugacity in the xy-spin system. Of course, these equations can be obtained from our flow equations by setting $y_d = y_l = 0$,

$$\frac{dK_s^{-1}}{dl} = 4\pi^3 y_v^2, \quad (28a)$$

$$\frac{dy_v}{dl} = (2 - \pi K_s) y_v. \quad (28b)$$

Several trajectories of these flow equations including the separatrix terminating at the repulsive fixed point P_2 ($K_s^* = 2/\pi$, $y_v^* = 0$) are plotted in Fig. 16. The initial conditions of physical relevance have to fulfill $y_v = \exp(-\pi C K_s)$. The critical value K_s^{crit} at which the transition occurs is determined by the intersection of the separatrix and the line of initial conditions. The value K_s^* which is also obtained from the simple heuristic argument presented in section 3 is the fully renormalized stiffness at the transition.

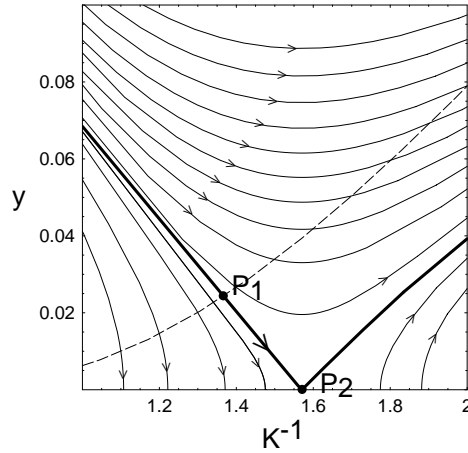


Figure 16: *Renormalization flows for the KT recursion relations. The dashed curve is a line of initial conditions. Some trajectories (thin lines) are shown. The critical value K_s^{crit} is determined by P_1 , the intersection of the separatrix (thick line) terminating at the fixed point P_2 ($K_s^* = 2/\pi$, $y_v^* = 0$) and the line of initial conditions.*

For $K_s > K_s^{crit}$ ($T < T^{crit}$) the fugacity is renormalized to zero whereas the temperature reduced stiffness saturates at a finite value smaller than the initial one. Therefore, on large scales no single defects are present. In the absence of topological defects SO is quasi-long ranged (QLR) characterized by an algebraic decay of the spin-spin correlation function, $\mathcal{C}_\sigma(\mathbf{r}) \sim |\mathbf{r}|^{-\eta_\sigma}$, where, in the absence of charge stripes, the exponent is given by $\eta_\sigma = 2\pi/K_s$. Since η_σ is renormalized to a finite value SO remains QLR.

For $K_s < K_s^{crit}$ ($T > T^{crit}$) the fugacity y_v diverges with the scale whereas the temperature-reduced stiffness K_s is renormalized to zero indicating that single vortices proliferate and QLRO is destroyed (η_σ goes to infinity). Since the flow equations are valid only for small fugacities they can be evaluated outside the ordered phase only up to a finite scale l^* where the fugacity becomes of the order unity. The divergence of η_σ signals short-range order with a finite correlation length, which scales as $\xi \sim e^{l^*}$ sufficiently close to the ordered phase. As shown in appendix C, the correlation length ξ diverges for $T \searrow T^{crit}$ as

$$\xi \sim \exp(\lambda(T - T^{crit})^{-\nu}), \quad (29)$$

with an exponent $\nu = 1/2$. While the value of the transition temperature T^{crit} depends on the constant C introduced in Eq.(22), the critical properties of the transition, namely the value of the exponent ν is not affected by this constant.

6 Results

In this section we proceed to integrate the flow equations (27) numerically to determine the precise shape of the phase diagram as well as the critical properties of the phase transitions. Outside the low-temperature phase where no free defects are present at least one order is rendered short-ranged, the corresponding correlation function decays exponentially, $\mathcal{C} \sim \exp(-r/\xi)$, with a correlation length ξ , which diverges due to Eq.(29) very close to the ordered phase. The critical exponent ν is calculated along the border to the ordered phase in section 6.2.

6.1 Phase diagram

Using a simple heuristic argument, we presented a qualitative picture of the phase diagram in section 3. From the rescaling contributions linear in the fugacities to the flow equations exactly the same picture is obtained. The unbinding of neutral defect pairs of a certain type is indicated by the divergence of the corresponding fugacity. Therefore, vortices proliferate for $\pi K_s < 2$ and loops for $4\pi K_c < 2$. Furthermore, for $\frac{\pi}{4}(K_s + 4K_c) < 2$ dislocations become relevant. The corresponding borders are shown in figure Fig. 17 as dashed lines.

In order to include the terms quadratic in the fugacities, the flow equations have to be integrated numerically. Thereby we use bare fugacities $y[\mathbf{m}] \equiv \exp\{-\pi C(K_s m_s^2 + K_c m_c^2)\}$ with the constant C determined in Eq. (22). A change of this constant has only quantitative effects on the location of the phase boundaries, the critical properties of the transitions are not affected by C .

In phase I all fugacities tend to zero as $l \rightarrow \infty$ and K_s and K_c are renormalized to finite values $K_s(\infty)$ and $K_c(\infty)$ smaller than the initial ones. The defects can be considered as being bound in local clusters of vanishing total charge. Their fluctuations enhance the wave excitations such that CO, SO, and LO remain quasi-long ranged: The correlation functions \mathcal{C}_ρ , \mathcal{C}_σ , and \mathcal{C}_\parallel decay algebraically like in the absence of defects, see Eqs. (10a),(10b), and (15). The exponents η_ν are controlled by H_{wave} (9) if the bare stiffness constants are replaced by the renormalized ones. Since the boundary of phase I flows to a line of fixed points (dashed lines in Fig. 17 for zero fugacities) with continuously varying values of the renormalized stiffness constants, the transition is non-universal with exponents given in Tab. 2.

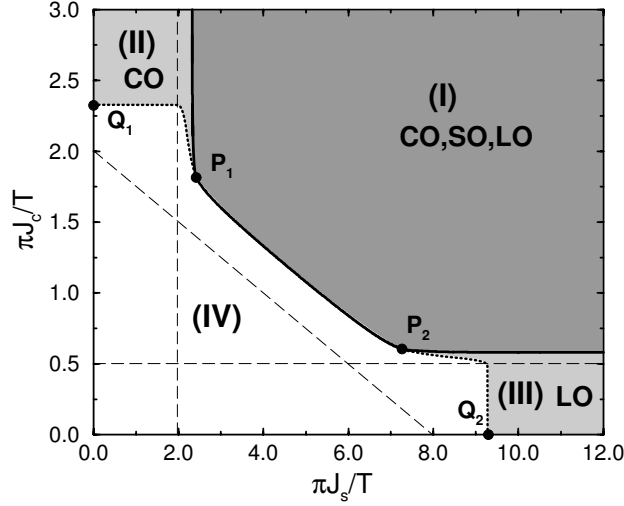


Figure 17: *Phase diagram. Thin dashed lines show where defects would become relevant for vanishing fugacities. For finite bare fugacities the transitions are located at the bold lines. Phase I has no free defects and therefore CO, SO, and LO exist. In phase II, vortices proliferate and destroy SO. In phase III, free loops are present, destroying CO and SO. Finally, all orders are absent in phase IV.*

Outside phase I, at least one fugacity increases with the scale. Since our flow equations are valid only for small fugacities, they can be evaluated outside the ordered phase only up to a finite scale l^* where some fugacity becomes of the order of unity. The divergence of a fugacity drives one or both stiffness constants to zero. A divergence of the renormalized exponent η then signals short-range order with a finite correlation length, which scales like $\xi \simeq ae^{l^*}$ sufficiently close to phase I. Although the divergence of fugacities hints at the nature of the phases II, III, and IV, the precise shape of the phase boundaries II/IV and III/IV is determined by strong coupling (large fugacity) regimes beyond the validity of Eqs. (27).

In phase II, vortices proliferate and the spin stiffness K_s is renormalized to zero. This leads to a destruction of the spin and the collinear order, since the exponents η_σ and η_\parallel are infinite. The corresponding correlation functions decay exponentially, $\mathcal{C}_\sigma \sim \mathcal{C}_\parallel \sim \exp(-r/\xi)$. Since K_s is renormalized to zero, the interaction in the spin sector effectively breaks down. Nevertheless, dislocations and loops are still coupled in the charge sector and can remain

	CO	SO	LO	ν
I/II	$\eta_\rho \leq \frac{1}{3}$	$\eta_\sigma \leq \frac{1}{3}$ *	$\eta_\parallel = 1$ *	$\frac{1}{2}$
I/III	$\eta_\rho = 1$ *	$\eta_\sigma \leq \frac{1}{3}$ *	$\eta_\parallel \leq \frac{1}{3}$	$\frac{1}{2}$
I/IV	$\frac{1}{3} \leq \eta_\rho \leq 1$ *	$\frac{1}{6} \leq \eta_\sigma \leq \frac{1}{2}$ *	$\frac{1}{3} \leq \eta_\parallel \leq 1$ *	$\frac{1}{2}$
II/IV	$\eta_\rho = \frac{1}{4}$ *	$\eta_\sigma = \infty$	$\eta_\parallel = \infty$	$\frac{1}{2}$
III/IV	$\eta_\rho = \infty$	$\eta_\sigma = \infty$	$\eta_\parallel = \frac{1}{4}$ *	$\frac{1}{2}$
P_1	$\eta_\rho = \frac{1}{3}$	$\eta_\sigma = \frac{1}{3}$	$\eta_\parallel = 1$	$\frac{2}{5}$
P_2	$\eta_\rho = 1$	$\eta_\sigma = \frac{1}{3}$	$\eta_\parallel = \frac{1}{3}$	$\frac{2}{5}$

Table 2: Values of the exponents η and ν at the phase transitions. Orders that become short-ranged at a transition line (η jumps to infinity) are marked by an asterisk.

bound for sufficiently large K_c ¹. Then also charge order remains quasi-long ranged with finite η_ρ .

In phase III loop pairs unbind and the charge stiffness K_c is renormalized to zero, leading to $\eta_\sigma = \eta_\rho = \infty$ and therefore to short-range spin and charge order. The spin order is destroyed because of the arbitrarily large fluctuations of the domain walls. Since K_s is screened only by bound vortices and dislocations, η_\parallel remains finite and quasi-long ranged collinear order is preserved. In phase IV the proliferating dislocations obviously render all correlations short ranged, $\mathcal{C}_\sigma \sim \mathcal{C}_\rho \sim \mathcal{C}_\parallel \sim \exp(-r/\xi)$.

As pointed out above the precise location of the transitions between phases II and IV and phases III and IV cannot be obtained by the weak coupling (low fugacity) flow equations. Nevertheless, we now present qualitative arguments for their location, focusing on the example of the transition II/IV. In the limit $K_s(0) = 0$ the interaction in the charge sector is simply switched off. Nevertheless, loops and dislocations interact in the charge sector; the former stronger than the latter. Therefore, the transition (point Q_1 with $K_c(\infty) = 2/\pi$) is driven by the unbinding of the dislocations. At this point loops are irrelevant and the transition belongs to the KT universality class. When the bare K_s is increased, it is renormalized to zero by free vortices and the transition occurs practically at the same value of K_c as long

¹In phase II, very close to phase I, the flow equations (27) show that y_v becomes of order 1 first. On larger scales, the flow equations are no longer reliable. They would suggest that the divergence of y_v entails the divergence of y_d and thus the destruction of all orders. On physical grounds one expects that the strong coupling limit should be described by $K_s = 0$ where the coupling of y_v to the other defects becomes meaningless.

as $K_s \lesssim 2/\pi$. When K_s increases to the value where vortices start to bind, the transition line II/IV reaches the point P_1 at a smaller value of K_c since dislocations start to be stabilized by the additional interaction in the spin sector. The situation for the transition line between the phases III and IV is similar, in this case the interaction of the charge components of the mixed defects is screened by the proliferating charge loops.

6.2 Correlation lengths of disordered phases

We proceed to calculate the correlation length of short ranged orders close to the ordered phase I. Outside phase I at least one fugacity diverges with the scale l indicating the proliferation of the associated defect type and causing the degradation of the involved orders. We determine the correlation length ξ of short-ranged orders by the scale l^* where the first fugacity reaches the order of unity. Approaching the ordered phase, the divergence of the correlation length $\xi \sim e^{l^*}$ follows Eq.(29). For large but finite systems sizes, ξ appears to diverge with an effective exponent ν_{eff} which appears to vary continuously in the range $0.4 \lesssim \nu_{\text{eff}} \lesssim 0.5$. Focussing on the vicinity of the triple point P_2 we have analyzed the divergence of ξ from a numerical integration of the flow equations up to $l_{\text{max}} = 10^3$ which corresponds to astronomically large scales. The resulting ν_{eff} (cf. Fig. 18) shows a notch at P_2 of a relatively small width which can become substantially larger for smaller values of l_{max} . In the thermodynamic limit, $l_{\text{max}} \rightarrow \infty$ the width of the notch goes to zero indicating that the exponent ν is discontinuous along the border of phase I, except for the triple points $P_{1,2}$ we have the KT value $\nu = 1/2$, whereas at the triple points the ν jumps to a smaller value. While this discontinuity describes the divergence of ξ in the thermodynamic limit, it is unlikely to be seen in samples of finite size.

On physical grounds the discontinuity of ν along the border of phase I is reasonable since only at the triple points $P_{1,2}$ the critical properties are governed by the balanced competition between two types of defects which can recombine into each other. Therefore only these special points do not belong to the universality class of the KT transition.

The value of the critical exponent ν at the triple points $P_{1,2}$ can be calculated analytically. Because of the symmetry of the flow equations we can concentrate on point P_2 . There one can neglect y_v to a good approximation and the conditions $y_l = y_d$ and $K_s = 12K_c$ (thin dotted line in Fig. 18 top) are conserved under the flow. In this case the flow equations for $Y := 2\pi\sqrt{6}y_d$

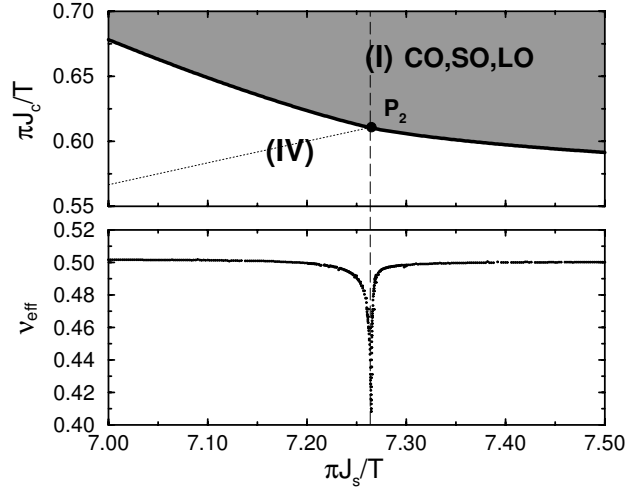


Figure 18: *Top: magnification of the phase diagram near point P_2 . In this region, phase III is extremely narrow and masked by the transition line to the right of P_2 . Bottom: Numerically calculated effective exponent ν_{eff} for $l_{\text{max}} = 10^3$ along the boundary of phase I.*

and the small variable $X := \frac{1}{\pi K_c} - 2$ read

$$\frac{dX}{dl} = Y^2, \quad (30a)$$

$$\frac{dY}{dl} = XY + 2\alpha Y^2, \quad (30b)$$

with $\alpha = 1/(2\sqrt{6})$. Sufficiently close to the separatrix these flow equations can be integrated analytically [114]. As shown in Appendix C the critical exponent ν for these flow equations is given by

$$\nu = 1 - \frac{1}{2} \left(\alpha^2 - \alpha\sqrt{\alpha^2 + 1} + 1 \right)^{-1} = \frac{2}{5}, \quad (31)$$

in excellent agreement with the numerically determined value $\nu_{\text{eff}} \approx 0.41$ (cf. Fig. 18 bottom).

7 Discussion and conclusion

From the phase diagram of our model several scenarios of spin-charge separation are possible. At low temperatures the stripe phase I is realized, CO, SO, and LO are quasi-long ranged. With increasing temperature the orders can disappear at a single transition or in a sequence of two transitions, depending on the ratio of the couplings J_c and J_s (cf. Fig. 19).

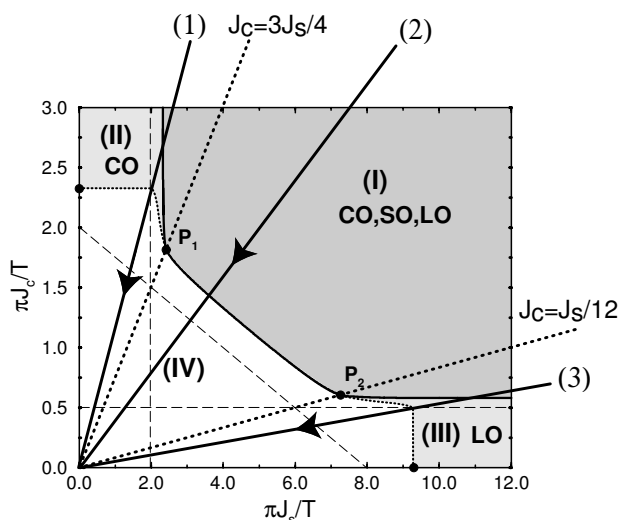


Figure 19: Possible scenarios of spin-charge separation. With increasing temperature CO, SO, and LO can disappear at a single transition (2) or in a sequence of two transitions (1,3) depending on the ratio of the stiffness constants.

- (1) For $J_c > \frac{3}{4}J_s$, there occur *two distinct transitions* with increasing temperature: first into phase II (loss of SO and LO), then into phase IV (loss of CO). This scenario is observed in experiments [102, 100].
- (2) For $\frac{1}{12}J_s < J_c < \frac{3}{4}J_s$ there is a *single transition* from phase I to phase IV where all orders disappear simultaneously.
- (3) For $J_c < \frac{1}{12}J_s$, CO and SO disappear at the same temperature of the phase transition I/III while LO disappears only at an even higher temperature at the transition III/IV.

The relation between J_s and J_c – which determines the scenario – can be tuned by doping. With increasing doping, the shrinking stripe distance should lead to a significant increase of J_c , whereas J_s should change only weakly since it is essentially determined by the antiferromagnetic exchange coupling. Therefore, in principle, the last scenario could be realized and the transition III/IV should be detectable for example by polarized neutron scattering.

To establish the phase diagram in the doping-temperature plane one should know the dependence of the phenomenological constants J_α on these parameters. This dependence is not provided by our analysis. However, one can draw conclusions about J_α from a comparison of our phase diagram to experiments. For example, in a doping range where $T_{CO} > T_{SO}$, our analysis implies that $J_c > \frac{3}{4}J_s$ and that $J_c \sim T_{CO}$ (cf. Fig. 19, path (1)). Furthermore, T_{CO} was found to have a maximum near a commensurate doping. We interpret this as a maximum of J_c which could be enhanced by renormalization effects close to a lock-in in a washboard potential.

From our findings, apart from the triple points the phase transitions should belong to the universality class of the KT transition. Approaching the ordered phase I, the correlation length of short ranged orders diverges due to Eq.(29) with a critical exponent $\nu = 1/2$ whereas at the triple points the exponent jumps to the smaller value $\nu = 2/5$. In systems with finite size the effective exponent ν_{eff} varies continuously between these values.

We compare our results with x-ray scattering data of the charge-ordering transition in $\text{La}_{5/3}\text{Sr}_{1/3}\text{NiO}_4$ [26]. In this compound the charge- and spin-ordering temperatures have been reported to be $T_{CO} \approx 240$ K and $T_{SO} \approx 180$ K [59]. Since the difference of the ordering temperatures is relatively large we expect that the charge stiffness is large compared to the spin stiffness and that the transition point of the charge ordering is far from the triple point. Therefore, the critical exponent ν_{eff} in the finite sample should be close to $\nu = 1/2$.

Due to the presence of disorder only a crossover at T_{CO} is observed experimentally (cf. Fig. 20). Below the charge ordering temperature the correlation length saturates at a finite value smaller than the sample size. The length scale of the disorder is quenched at low temperatures since the correlation length does not increase as the temperature is lowered significantly below T_{CO} . Above T_{CO} only a weak scattering at the expected positions in reciprocal lattice space is observed, however Du *et al.* [26] were able to extract the correlation length up to a temperature $T_{CO} + 20$ K. Fitting the correlation length

above the ordering temperature with a power law, $\xi \sim [(T - T_{CO})/T_{CO}]^{-\nu}$ with $\nu \approx 1$ they concluded that the transition belongs to the 2D-Ising universality class.

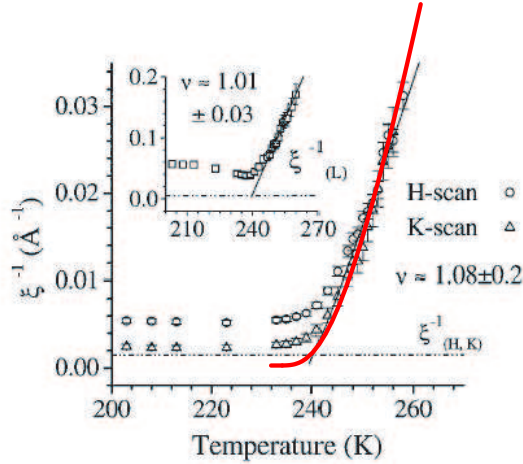


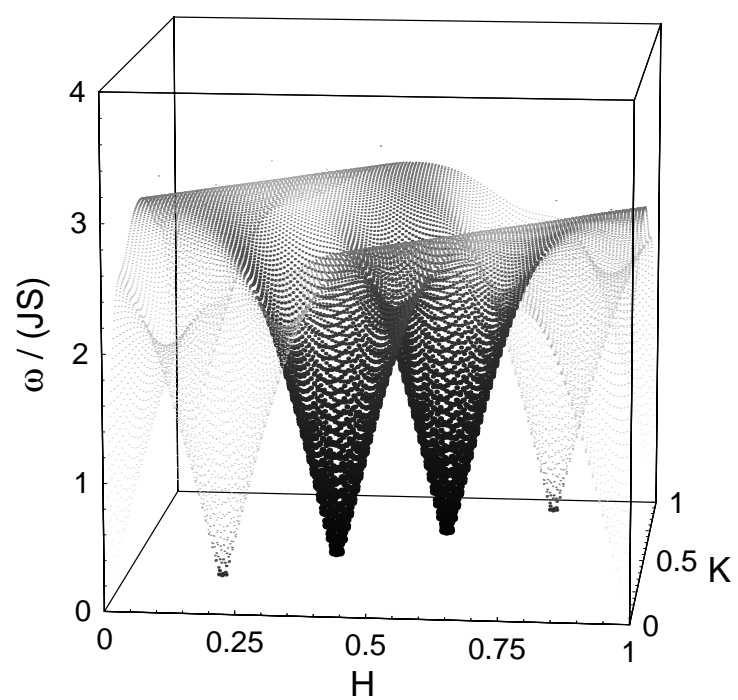
Figure 20: *The evolution of the inverse correlation length of the charge stripe satellite [26]. In this work the data was fitted by a power law $\xi^{-1} \sim [(T - T_{CO})/T_{CO}]^\nu$ with $\nu \approx 1$ and $T_{CO} \approx 240\text{K}$ (thin curve). Finite correlation length below T_{CO} indicate the presence of disorder. Our fit with Eq. (29) is shown as bold curve.*

However, the data is also consistent with our findings since the temperature dependence of the correlation length is at least as well fitted with Eq.(29) (cf. Fig. 20). From the data a concluding decision on the criticality of the transition is not possible since the transition is washed out by disorder and the available data for $T > T_{CO}$ is limited to a range of 20 K only.

In conclusion, we have examined a model of coupled spin and charge order in stripe phases, from which several scenarios of spin charge separation are possible. We have shown that the transitions between the various phases are nonuniversal. We have identified collinearity as a physical quantity that allows one to discriminate between the phases III and IV. Several interesting questions invite further investigations, in particular, the properties of related quantum critical points at zero temperature and the influence of disorder (see also [119, 8]) on the nature of ordering.

Part III

Spin dynamics of stripes



1 Introduction

The evidence for the formation of stripes in high-temperature superconductors (HTSC) and related materials increases continuously. Several years after the theoretical prediction [116, 92, 63] of stripes as a combined charge and spin-density wave phenomenon experimental evidence for these superstructures in the insulating nickelate compound $\text{La}_{2-x}\text{Sr}_x\text{NiO}_{4+\delta}$ (LSNO) as well as in the superconducting cuprate $\text{La}_{2-x}\text{Sr}_x\text{CuO}_4$ (LSCO) was supplied by Tranquada and co-workers [101, 102]. More recent experimental evidence [21, 72, 43, 42] for stripes in the paradigmatic HTSCs $\text{YBaCuO}_{6+\delta}$ (YBCO) and $\text{Bi}_2\text{Sr}_2\text{CaCu}_2\text{O}_{8+\delta}$ (BSCCO) strengthens the expectation that stripe formation in doped layered perovskites is quite generic.

A prominent piece of phenomenology in the cuprates is the magnetic resonance peak, the so-called π -resonance, observed in neutron scattering [88, 33, 50, 41, 23], which is the presence of extra scattering weight appearing at the antiferromagnetic wave vector at finite frequency. The resonance is sharp in both, frequency and momentum.

Since LSCO and YBCO are paradigmatic for monolayer and bilayer compounds, stripe-like “low”-energy response is characteristic for both classes of materials. On the other hand, at “high” energies spin fluctuations appeared to be qualitatively different since a commensurate π -resonance had been observed only in bilayer compounds, notably in $\text{YBa}_2\text{Cu}_3\text{O}_{6+x}$ [88, 33] and $\text{Bi}_2\text{Sr}_2\text{CaCu}_2\text{O}_{8+x}$ [50], whereas it seemed to be absent in monolayer compounds. This apparent distinction between mono- and bilayer compounds lost its justification only recently, when the π -resonance was discovered in $\text{Tl}_2\text{Ba}_2\text{CuO}_{6+x}$ [41] as the first monolayer compound. The fact that the π -resonant mode has not been detected in LSCO so far can possibly be ascribed to a larger effective strength of disorder, since the Sr-dopants are randomly distributed whereas in the oxygen doped compounds the excess oxygen orders in chains. Thus, one may believe that, in principle, mono- and bilayer compounds have qualitatively similar features also at higher energies. This universality of low- and high-energy features calls for an even more unifying framework [3].

At present, it is still an open question to what extent the stripe picture can account for spin fluctuations not only at low energies where collective magnetic excitations are observed at satellite positions in the vicinity of the antiferromagnetic wave vector, but also over a wider energy range, including the resonance phenomenon at the antiferromagnetic wave vector (see Refs.

[9, 41] and references therein). The specific form of the dynamic magnetic response – including incommensurability and π resonance – gave rise to doubts that it could be consistent with the stripe model [12]. On the other hand, there are proposals [3] that both features may be rooted in a stripe-like spin-density wave.

We complement the spin-wave analysis by Batista *et al.* [3]. There, the emphasis was put on generic features of striped systems for an arbitrary ratio between the spin spacing a and the stripe spacing d . For general ratios the structure of the magnetic excitation spectrum can be quite intricate due to the coupling of a larger number of modes with different wave vectors giving rise to a quasi continuous excitation spectrum. However, in many cases of interest, this ratio $p := d/a$ is very close to an integer value. Within the stripe model one actually expects that integer values are very stable due to a lock-in of the superstructure into the atomic structure. This pinning mechanism is considered as the origin of the so called ‘1/8 conundrum’ in the cuprates [102], i.e., the stability of $p = 4$ over a considerable doping range. Detailed measurements of the spin-excitation spectrum are available close to integer p : $p = 3$ in LSNO [11], $p = 4$ in LSCO [57], and $p = 4$ [70] and $p = 5$ [12] in YBCO.

In order to test whether these experiments can be consistent with the spin-wave excitation spectrum of a stripe model in the simplest and most transparent case, we therefore examine integer p . In this case a stripe state can be conveniently modelled in a real-space picture as a periodic structure of possible electron/hole positions on the square lattice. Our studies are based on a spin-only model which does not fully account for electronic correlations. In particular, a possible spin gap at very low energies due to the formation of Cooper pairs is not incorporated in our model. Nevertheless, one can expect an adequate description of the spin fluctuations well above the gap energy. This energy range also includes the π -resonance energy. At higher energies magnetic excitations beyond spin waves may become relevant. The magnetic excitations in stripe ordered $\text{La}_{1.875}\text{Ba}_{0.125}\text{CuO}$ observed recently [103] resemble spin-waves at low energies whereas at higher energies they are very similar to spin-1 excitations of isolated spin ladders.

In the first instance we focus on a single layer. Particular attention is paid to the spin-wave band structure in the vicinity of the antiferromagnetic wave vector. While the incommensurability as zero-frequency response is fixed by the geometry of the model, we calculate the spin-wave velocities at the incommensurability and the π -resonance as dynamic features. We evaluate

the dependence of these quantities on the doping level and the exchange coupling across the stripes. By a quantitative comparison, we determine the value of the exchange coupling across the stripes as the only *a priori* unknown model parameter. In particular, the dependence of the π -resonance on doping is found to be consistent with experiments.

Finally, we extend the model to bilayer systems in order to predict the corresponding features of the magnon band structure and the magnetic structure factor. We consider several possibilities (parallel and perpendicular relative orientations) of the charge order in the antiferromagnetically coupled neighboring layers. Again, the band structure and the $T = 0$ inelastic structure factor for even and odd excitations are calculated in linear spin-wave theory. Particular attention is paid to the band-splitting in the vicinity of the antiferromagnetic wave vector and to the influence of the interlayer coupling on the π -resonance energy.

In section 2 we introduce the spin-only model for a single layer that constitutes the basis of our study. The linear spin-wave theory is outlined in Sec. 3. We derive general expressions for the magnon dispersion relation and the inelastic structure factor at $T = 0$. In Sec. 4 we evaluate these expressions analytically for the pure antiferromagnet which should be recovered in the limit of $p \rightarrow \infty$ (corresponding to zero doping) and present numerical results for the magnon dispersion relation, spin-wave velocities, π -resonance, and the structure factor. We distinguish between diagonal and vertical stripes and consider different integer stripe spacings p . Additionally, we calculate the density of states in the case of diagonal stripes with a spacing $p = 3$. In Sec. 5 the results of our theory are discussed and compared to experimental data. After a short interim balance in section 6, we extend our model to a bilayer one in section 7. Classical ground states and the resulting phase diagrams for competing types of magnetic order are obtained. They are needed as starting point for the linear spin-wave theory. A customized formulation thereof is outlined in Sec. 8. The results, namely the spin-wave band structure, the zero-temperature structure factor for even and odd excitations, and the dependence of the band splitting at the antiferromagnetic wave-vector on the strength of the interlayer coupling are presented in Sec. 9 and compared to experiments in Sec. 10.

2 Spin-only model for a single layer

We start to introduce the minimalistic real-space spin-only model, which is the basis of our spin-wave analysis of the magnetic excitation spectrum in stripe phases. Here we focus on a single layer, since in monolayer compounds the interlayer couplings are negligible small. Later on in section 7 we extend the model to a bilayer since in various compounds the magnetic layers are grouped to closely spaced and relatively strong coupled pairs. For simplicity, the holes induced by doping are assumed to form site-centered rivers that act as anti-phase boundaries for the antiferromagnetically coupled spins populating a square lattice [102]. This naive real space picture is consistent with integer stripe spacings p . The rivers are assumed to be only one lattice spacing wide (cf. Fig. 21).

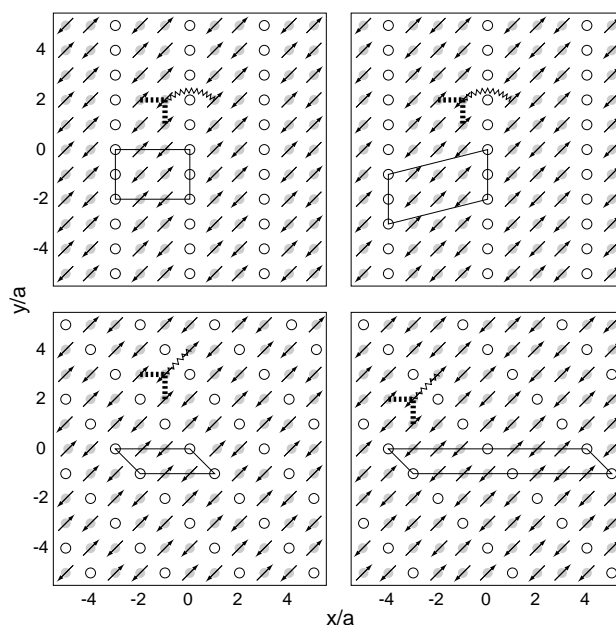


Figure 21: *Illustration of vertical and diagonal stripe patterns with spacings $p = 3$ and $p = 4$. The hole positions are indicated by open circles and the electron positions by grey ones. The arrows correspond to the spin orientations in the classical ground state. Parallelograms outline possible magnetic unit cells. In our model, we assume antiferromagnetic exchange couplings of strength J within the domains (dashed lines) and λJ across stripes (zig-zag lines).*

Since stripes are vertical in cuprates for doping concentrations where superconductivity occurs and diagonal in nickelates, we study both orientations with arbitrary integer stripe spacing p . Furthermore, the holes are considered as immobile since we are solely interested in the response of the spin degrees of freedom. However, in a spin-only model fluctuations of the charge stripes are captured by a modulation of the exchange couplings perpendicular to the stripes.

We are interested in collective excitations around a ground state, which – for classical spins – could be represented by $\mathbf{S}(\mathbf{r}) = S\{0, 0, \sigma(\mathbf{r})\}$ with $\sigma = \pm 1$ on the electron positions and $\sigma = 0$ on the hole positions (as illustrated in Fig. 21). Denoting by $\mathbf{A}^{(1)}$ and $\mathbf{A}^{(2)}$ the primitive basis vectors of the magnetic unit cell and by $\mathbf{A} = m_1\mathbf{A}^{(1)} + m_2\mathbf{A}^{(2)}$ an arbitrary magnetic lattice vector, the classical spin variables obey the translational symmetry $\sigma(\mathbf{r}) = \sigma(\mathbf{r} + \mathbf{A})$. By placing the origin at a hole position we obtain the additional reflection symmetry $\sigma(\mathbf{r}) = -\sigma(-\mathbf{r})$.

For a paradigmatic and minimalistic description of magnetic quantum fluctuations we use a spin-only model with pair exchange. More complicated exchange processes such as cyclic exchange [97, 75, 105] may be important for quantitative purposes but are ignored here for simplicity. We use a generalized Heisenberg model on the two-dimensional square lattice [104]

$$\mathcal{H} = \frac{1}{2} \sum'_{\mathbf{r}, \mathbf{r}'} J(\mathbf{r}, \mathbf{r}') \mathbf{S}(\mathbf{r}) \mathbf{S}(\mathbf{r}'), \quad (32)$$

where the primed sums run over all spin positions with $\sigma \neq 0$. The exchange couplings obey the symmetry relations

$$J(\mathbf{r}, \mathbf{r}') = J(\mathbf{r}', \mathbf{r}), \quad (33a)$$

$$J(\mathbf{r}, \mathbf{r}') = J(\mathbf{r} + \mathbf{A}, \mathbf{r}' + \mathbf{A}), \quad (33b)$$

$$J(\mathbf{r}, \mathbf{r}') = J(-\mathbf{r}, -\mathbf{r}'). \quad (33c)$$

In fact, the exchange couplings may have a higher symmetry corresponding to the hole lattice, which however will not be needed explicitly in the further analysis. To implement that the hole strings act as antiphase boundaries between antiferromagnetic domains, we assume that $J(\mathbf{r}, \mathbf{r}') = J > 0$ for nearest neighbors \mathbf{r}, \mathbf{r}' within the domains and $J(\mathbf{r}, \mathbf{r}') = \lambda J > 0$ for nearest neighbors across a string.

While it is natural to assume that J should be comparable to the exchange coupling in the undoped material, the coupling λJ may deviate significantly.

To keep the number of parameters small, we ignore that the exchange coupling even within an antiferromagnetic domain should depend on the position of the pair relative to the hole strings.

3 Spin-wave theory

We address the spin dynamics in the framework of linear spin-wave theory (for a review in the context of cuprates, see e.g. Ref. [64]). In the following analytic part we keep the general form of the model and specialize to specific stripe configurations later in Sec. 4 when we numerically evaluate the results of this section. From now on all lengths are expressed in units of the square-lattice spacing a .

3.1 Holstein-Primakoff representation

In the first step we flip all spins on one sublattice by

$$S^x(\mathbf{r}) = \sigma^2(\mathbf{r})\tilde{S}^x(\mathbf{r}), \quad (34a)$$

$$S^y(\mathbf{r}) = \sigma(\mathbf{r})\tilde{S}^y(\mathbf{r}), \quad (34b)$$

$$S^z(\mathbf{r}) = \sigma(\mathbf{r})\tilde{S}^z(\mathbf{r}). \quad (34c)$$

The spin commutator relations $[S^i, S^j] = i\epsilon_{ijk}S^k$ are preserved under this rotation. Thereby, we allow $\tilde{\mathbf{S}}$ to have spin S also at the hole sites. Although this introduces certain modes of zero energy, as we will discuss below, it is advantageous to use a $\tilde{\mathbf{S}}$ with a *homogeneous* ferromagnetic ground state. The corresponding transformed Hamiltonian reads

$$\mathcal{H} = \frac{1}{2} \sum_{\mathbf{r}, \mathbf{r}'} \tilde{J}(\mathbf{r}, \mathbf{r}') \left[\tilde{S}^z(\mathbf{r})\tilde{S}^z(\mathbf{r}') + \tilde{S}^y(\mathbf{r})\tilde{S}^y(\mathbf{r}') + \sigma(\mathbf{r})\sigma(\mathbf{r}')\tilde{S}^x(\mathbf{r})\tilde{S}^x(\mathbf{r}') \right] \quad (35)$$

We have defined the new couplings $\tilde{J}(\mathbf{r}, \mathbf{r}') := J(\mathbf{r}, \mathbf{r}')\sigma(\mathbf{r})\sigma(\mathbf{r}')$ which obey the same symmetry relations (33) as $J(\mathbf{r}, \mathbf{r}')$. In the next step we represent the spin operators by the usual Holstein-Primakoff (HP) bosons via

$$\tilde{S}^+ = \sqrt{2S - \hat{n}} b, \quad (36a)$$

$$\tilde{S}^- = b^\dagger \sqrt{2S - \hat{n}}, \quad (36b)$$

$$\tilde{S}^z = -\hat{n} + S, \quad (36c)$$

with $\tilde{S}^\pm = \tilde{S}^x \pm i\tilde{S}^y$. The eigenstates of the number operator $\hat{n} = b^\dagger b$ are restricted to $n \leq 2S$ and the HP-operators fulfill the canonical commutator relations $[b, b^\dagger] = 1$. The linearized spin-wave Hamiltonian \mathcal{H}_{sw} is given by

the terms quadratic in the bosonic operators,

$$\mathcal{H}_{\text{sw}} = \frac{S}{2} \sum_{\mathbf{r}, \mathbf{r}'} \left\{ f(\mathbf{r}, \mathbf{r}') [b^\dagger(\mathbf{r})b(\mathbf{r}') + b(\mathbf{r})b^\dagger(\mathbf{r}')] \right. \\ \left. + g(\mathbf{r}, \mathbf{r}') [b(\mathbf{r})b(\mathbf{r}') + b^\dagger(\mathbf{r})b^\dagger(\mathbf{r}')] \right\}, \quad (37a)$$

$$f(\mathbf{r}, \mathbf{r}') = \frac{1}{2} \tilde{J}(\mathbf{r}, \mathbf{r}') [\sigma(\mathbf{r})\sigma(\mathbf{r}') + 1] - \delta_{\mathbf{r}, \mathbf{r}'} \sum_{\mathbf{r}'} \tilde{J}(\mathbf{r}, \mathbf{r}'), \quad (37b)$$

$$g(\mathbf{r}, \mathbf{r}') = \frac{1}{2} \tilde{J}(\mathbf{r}, \mathbf{r}') [\sigma(\mathbf{r})\sigma(\mathbf{r}') - 1]. \quad (37c)$$

Obviously the functions f and g again satisfy the symmetry relations (33). For further manipulations it is useful to decompose a vector $\mathbf{r} = \mathbf{A} + \mathbf{a}$ on the square lattice into a vector $\mathbf{A} = m_1 \mathbf{A}^{(1)} + m_2 \mathbf{A}^{(2)}$ on the magnetic lattice and a decoration vector \mathbf{a} . The number of vectors \mathbf{a} is denoted by N (the area of the magnetic unit cell). In momentum space, the reciprocal magnetic basis $\mathbf{Q}^{(i)}$ defines the corresponding magnetic Brillouin zone (\mathcal{BZ}). Wave vectors \mathbf{k} can be uniquely decomposed into $\mathbf{k} = \mathbf{Q} + \mathbf{q}$ with $\mathbf{q} \in \mathcal{BZ}$ and $\mathbf{Q} = m_1 \mathbf{Q}^{(1)} + m_2 \mathbf{Q}^{(2)}$. Within the Brillouin zone of the square lattice there are N vectors \mathbf{Q} which we denote by \mathbf{Q}_ν .

We Fourier transform the bosonic operators via $b(\mathbf{r}) = \int_{\mathbf{k}} \exp(i\mathbf{k}\mathbf{r}) b(\mathbf{k})$, where $\int_{\mathbf{k}} = (2\pi)^{-2} \int d^2k$ and the \mathbf{k} integrals run over the Brillouin zone of the square lattice with an area $(2\pi)^2$. Using these decompositions and the Poisson sum formula

$$\sum_{\mathbf{A}} e^{i\mathbf{k}\mathbf{A}} = \frac{1}{N} \sum_{\mathbf{Q}} \delta(\mathbf{k} + \mathbf{Q}) \quad (38)$$

we rewrite the spin-wave Hamiltonian as

$$\mathcal{H}_{\text{sw}} = \frac{1}{2} \int_{\mathbf{q}} \sum_{\nu, \nu'} \left\{ F_{\nu, \nu'}(\mathbf{q}) [b_{\mathbf{q}+\mathbf{Q}_\nu}^\dagger b_{\mathbf{q}+\mathbf{Q}_{\nu'}} + b_{-\mathbf{q}-\mathbf{Q}_\nu} b_{-\mathbf{q}-\mathbf{Q}_{\nu'}}^\dagger] \right. \\ \left. + G_{\nu, \nu'}(\mathbf{q}) [b_{\mathbf{q}+\mathbf{Q}_\nu}^\dagger b_{-\mathbf{q}-\mathbf{Q}_{\nu'}}^\dagger + b_{-\mathbf{q}-\mathbf{Q}_\nu} b_{\mathbf{q}+\mathbf{Q}_{\nu'}}] \right\}, \quad (39)$$

where

$$F_{\nu, \nu'}(\mathbf{q}) = \frac{S}{N} \sum_{\mathbf{A}} \sum_{\mathbf{a}, \mathbf{a}'} f(\mathbf{a} + \mathbf{A}, \mathbf{a}') \cos [\mathbf{q}\mathbf{A} + \mathbf{q}(\mathbf{a} - \mathbf{a}') + \mathbf{Q}_\nu \mathbf{a} - \mathbf{Q}_{\nu'} \mathbf{a}'] \quad (40)$$

is essentially the Fourier transform of f ,

$$\frac{S}{N}f(\mathbf{Q}_\nu + \mathbf{q}, \mathbf{Q}_{\nu'} + \mathbf{q}') = \delta(\mathbf{q} + \mathbf{q}')F_{\nu,\nu'}(\mathbf{q}). \quad (41)$$

Analogous expressions relate G to g .

3.2 Bogoliubov transformation

To diagonalize the Hamiltonian, we express the bosonic operators by canonical coordinate and momentum operators $\Phi_\nu(\mathbf{q}) := \Phi(\mathbf{q} + \mathbf{Q}_\nu)$ and $\Pi_\nu(\mathbf{q}) := \Pi(\mathbf{q} + \mathbf{Q}_\nu)$ via the relations

$$\Phi_\nu(\mathbf{q}) = \frac{1}{\sqrt{2}} \left(b_{\mathbf{q}+\mathbf{Q}_\nu} + b_{-\mathbf{q}-\mathbf{Q}_\nu}^\dagger \right), \quad (42a)$$

$$\Pi_\nu(\mathbf{q}) = \frac{1}{\sqrt{2}i} \left(b_{-\mathbf{q}-\mathbf{Q}_\nu} - b_{\mathbf{q}+\mathbf{Q}_\nu}^\dagger \right). \quad (42b)$$

In terms of these operators, the spin-wave Hamiltonian reads

$$\begin{aligned} \mathcal{H}_{\text{sw}} = & \frac{1}{2} \int_{\mathbf{q}} \sum_{\nu,\nu'} \left\{ \Pi_\nu^\dagger(\mathbf{q}) M_{\nu,\nu'}^{-1}(\mathbf{q}) \Pi_{\nu'}(\mathbf{q}) \right. \\ & \left. + \Phi_\nu^\dagger(\mathbf{q}) K_{\nu,\nu'}(\mathbf{q}) \Phi_{\nu'}(\mathbf{q}) \right\}, \end{aligned} \quad (43)$$

with the inverse mass matrix $\mathbf{M}^{-1} = \mathbf{F} - \mathbf{G}$ and the coupling matrix $\mathbf{K} = \mathbf{F} + \mathbf{G}$. As a result of the invariance of the Hamiltonian under the replacement $\tilde{S}^x(\mathbf{r}) \rightarrow \sigma(\mathbf{r})\tilde{S}^x(\mathbf{r})$, $\tilde{S}^y(\mathbf{r}) \rightarrow \sigma(\mathbf{r})\tilde{S}^y(\mathbf{r})$ one can easily derive the symmetry conditions

$$\mathbf{K} = \boldsymbol{\sigma} \mathbf{M}^{-1} \boldsymbol{\sigma}, \quad (44a)$$

$$\mathbf{M}^{-1} = \boldsymbol{\sigma} \mathbf{K} \boldsymbol{\sigma}, \quad (44b)$$

with the hermitian matrix $\sigma_{\nu,\nu'} := \frac{1}{N} \sum_{\mathbf{a}} e^{-i(\mathbf{Q}_\nu - \mathbf{Q}_{\nu'})\mathbf{a}} \sigma(\mathbf{a})$. To simplify notation, we suppress arguments \mathbf{q} which may be considered as fixed during the diagonalization in ν space and use the pseudo Dirac notation $|\Phi\rangle := \sum_\nu \Phi_\nu |\nu\rangle$, $|\Pi\rangle := \sum_\nu \Pi_\nu |\nu\rangle$ with the Cartesian basis $|\nu\rangle$, $\nu = 1, \dots, N$. After performing the canonical transformation $|\Phi\rangle = \mathbf{M}^{-1/2} |\tilde{\Phi}\rangle$, $|\Pi\rangle = \mathbf{M}^{1/2} |\tilde{\Pi}\rangle$ the Hamiltonian can be rewritten as

$$\mathcal{H}_{\text{sw}} = \frac{1}{2} \int_{\mathbf{q}} \left\{ \langle\langle \tilde{\Pi} | \tilde{\Pi} \rangle\rangle + \langle\langle \tilde{\Phi} | \mathbf{M}^{-1/2} \mathbf{K} \mathbf{M}^{-1/2} | \tilde{\Phi} \rangle\rangle \right\}, \quad (45)$$

and we still have to diagonalize $\mathbf{M}^{-1/2}\mathbf{K}\mathbf{M}^{-1/2} = \mathbf{W}^2$ with hermitian $\mathbf{W} := \mathbf{M}^{-1/2}\boldsymbol{\sigma}\mathbf{M}^{-1/2}$. Introducing an orthonormal eigenbasis $\{|\alpha\rangle\rangle, \alpha = 1, \dots, N\}$ of this matrix, $\mathbf{W}|\alpha\rangle\rangle = \xi_\alpha|\alpha\rangle\rangle$, and defining $\omega_\alpha := |\xi_\alpha|$ we can transform to normal coordinates

$$\tilde{\Phi}_\nu = \sum_\alpha \omega_\alpha^{-1/2} \langle\langle \nu | \alpha \rangle\rangle \tilde{\Phi}_\alpha, \quad (46a)$$

$$\tilde{\Pi}_\nu = \sum_\alpha \omega_\alpha^{1/2} \langle\langle \alpha | \nu \rangle\rangle \tilde{\Pi}_\alpha, \quad (46b)$$

and obtain

$$\mathcal{H}_{\text{sw}} = \frac{1}{2} \sum_\alpha \int_{\mathbf{q}} \omega_\alpha \left\{ \tilde{\Pi}_\alpha^\dagger \tilde{\Pi}_\alpha + \tilde{\Phi}_\alpha^\dagger \tilde{\Phi}_\alpha \right\}. \quad (47)$$

Transforming back to corresponding bosonic operators $\tilde{\Phi}_\alpha(\mathbf{q}) = \frac{1}{\sqrt{2}}[b_\alpha(\mathbf{q}) + b_\alpha^\dagger(-\mathbf{q})]$, $\tilde{\Pi}_\alpha(\mathbf{q}) = \frac{1}{\sqrt{2i}}[b_\alpha(-\mathbf{q}) - b_\alpha^\dagger(\mathbf{q})]$ we obtain the final diagonal bosonic representation of the spin-wave Hamiltonian

$$\mathcal{H}_{\text{sw}} = \sum_\alpha \int_{\mathbf{q}} \omega_\alpha(\mathbf{q}) \left\{ \frac{1}{2} + b_\alpha^\dagger(\mathbf{q})b_\alpha(\mathbf{q}) \right\}. \quad (48)$$

Thus, as the result of the above diagonalization we obtain $\omega_\alpha(\mathbf{q})$ as the magnon dispersion relation with the band index α .

We would like to remark that the $|\nu\rangle\rangle$ space contains a common subspace of eigenvectors of the matrices $\boldsymbol{\sigma}$, \mathbf{M}^{-1} and \mathbf{K} with vanishing eigenvalues. This subspace is h dimensional, where h is the number of holes in the magnetic unit cell. These zero modes are an artifact of the introduction of spins $\hat{\mathbf{S}}$ on the hole sites. All above manipulations, including e.g. the calculation of $\mathbf{M}^{1/2}$ and ω_α^{-1} , are well defined on the orthogonal subspace of physical spins.

3.3 Structure factor

In this section we proceed to calculate the zero-temperature structure factor

$$\mathcal{S}(\mathbf{k}, \omega) := \sum_{\mathbf{F}} \sum_{j=x,y,z} |\langle \mathbf{F} | S^j(\mathbf{k}) | 0 \rangle|^2 \delta(\omega - \omega_{\mathbf{F}}). \quad (49)$$

Here, $|0\rangle$ denotes the ground state (the magnon vacuum) characterized by $b_\alpha(\mathbf{q})|0\rangle = 0$ and we consider only single-magnon states $|\mathbf{F}\rangle$ with excitation

energy $\omega_F := E_F - E_0$. Since

$$\begin{aligned} S^z(\mathbf{k}) &= S \sum_{\nu'} \delta(\mathbf{k} - \mathbf{Q}_{\nu'}) \sigma(\mathbf{Q}_{\nu'}) \\ &\quad - \sum_{\nu'} \sigma(\mathbf{Q}_{\nu'}) \int_{\mathbf{k}''} b^\dagger(\mathbf{k}'') b(\mathbf{k} - \mathbf{Q}_{\nu'} + \mathbf{k}'') \end{aligned} \quad (50)$$

with $\sigma(\mathbf{Q}) := \frac{1}{N} \sum_{\mathbf{a}} e^{-i\mathbf{Q}\mathbf{a}} \sigma(\mathbf{a})$ preserves the magnon number, it contributes only to the elastic part of the structure factor,

$$\mathcal{S}^{\text{el}}(\mathbf{k}, \omega) \propto S^2 \sum_{\mathbf{Q}} \delta(\mathbf{k} - \mathbf{Q}) |\sigma(\mathbf{Q})|^2 \delta(\omega). \quad (51)$$

To calculate the inelastic part of the structure factor (which has contributions of order S only from $j = x, y$) we express these spin components by the bosonic operators using the transformations derived in section 3.2,

$$\begin{aligned} S^x(\mathbf{q} + \mathbf{Q}_\nu) &\approx \sqrt{S} \sum_{\nu'} \sigma^{(2)}(\mathbf{Q}_\nu - \mathbf{Q}_{\nu'}) \Phi_{\nu'}(\mathbf{q}) \\ &= \sqrt{\frac{S}{2}} \sum_{\alpha, \nu'} \sigma^{(2)}(\mathbf{Q}_\nu - \mathbf{Q}_{\nu'}) \omega_\alpha^{-1/2} \\ &\quad \times \langle\langle \nu' | \mathbf{M}^{-1/2} | \alpha \rangle\rangle [b_\alpha(\mathbf{q}) + b_\alpha^\dagger(-\mathbf{q})], \end{aligned} \quad (52a)$$

$$\begin{aligned} S^y(\mathbf{q} + \mathbf{Q}_\nu) &\approx \sqrt{S} \sum_{\nu'} \sigma(\mathbf{Q}_\nu - \mathbf{Q}_{\nu'}) \Pi_{\nu'}^\dagger(\mathbf{q}) \\ &= i \sqrt{\frac{S}{2}} \sum_{\alpha, \nu'} \sigma(\mathbf{Q}_\nu - \mathbf{Q}_{\nu'}) \omega_\alpha^{1/2} \\ &\quad \times \langle\langle \nu' | \mathbf{M}^{1/2} | \alpha \rangle\rangle [b_\alpha(\mathbf{q}) - b_\alpha^\dagger(-\mathbf{q})], \end{aligned} \quad (52b)$$

where we have defined $\sigma^{(2)}(\mathbf{Q}) := \frac{1}{N} \sum_{\mathbf{a}} e^{-i\mathbf{Q}\mathbf{a}} \sigma^2(\mathbf{a})$. Since the contributing final states are just given by the one-magnon states $|F\rangle = b_\alpha^\dagger(\mathbf{q})|0\rangle$ it is easy to calculate the inelastic part of the structure factor. Using the relations $\sigma^2 \mathbf{M}^{-1/2} |\alpha\rangle\rangle = \sigma \mathbf{M}^{1/2} \mathbf{W} |\alpha\rangle\rangle = \xi_\alpha \sigma \mathbf{M}^{1/2} |\alpha\rangle\rangle$ and $\sigma^2 \mathbf{M}^{-1/2} |\alpha\rangle\rangle = \mathbf{M}^{-1/2} |\alpha\rangle\rangle$ we obtain

$$\mathcal{S}^{\text{in}}(\mathbf{q} + \mathbf{Q}_\nu, \omega) = S \sum_{\alpha} S_\alpha(\mathbf{q} + \mathbf{Q}_\nu) \delta(\omega - \omega_\alpha(\mathbf{q})), \quad (53a)$$

$$S_\alpha(\mathbf{q} + \mathbf{Q}_\nu) = \langle\langle \nu | \mathbf{M}^{-1/2} | \alpha \rangle\rangle \frac{1}{\omega_\alpha} \langle\langle \alpha | \mathbf{M}^{-1/2} | \nu \rangle\rangle. \quad (53b)$$

At this point it may be helpful to remind that \mathbf{q} is an implicit argument of ω_α , $\mathbf{M}^{-1/2}$, and $|\alpha\rangle$. The periodicity $\omega_\alpha(\mathbf{q}) = \omega_\alpha(\mathbf{q} + \mathbf{Q})$ of the eigenfrequencies is absent in the structure factor since the coupling of an external field to a spin wave wave vector $\mathbf{k} = \mathbf{q} + \mathbf{Q}$ depends on \mathbf{Q} .

4 Monolayer results

In this section we evaluate the general expressions for the magnon dispersion and the inelastic $T = 0$ structure factor for diagonal and vertical stripes with different spacing p and couplings λ . The spin-wave velocities parallel and perpendicular to the stripe direction are calculated as a function of the doping $x = 1/p$ and the coupling λ across a charge stripe. Since in the limit $p \rightarrow \infty$ the results of the pure antiferromagnet should be recovered we briefly specialize our analysis to the undoped case.

4.1 Pure antiferromagnet

In the case of the pure system a possible magnetic unit cell is given by the base vectors $\mathbf{A}^{(1)} = (2, 0)$ and $\mathbf{A}^{(2)} = (-1, 1)$. The number of spins in the unit cell (corresponding to the area of the cell) is given by $N = 2$. The classical ground state is a perfectly ordered Néel state, the two sublattices are characterized by $\sigma = 1$ and $\sigma = -1$. To obtain the symmetry $\sigma(\mathbf{r}) = -\sigma(-\mathbf{r})$ used for the Fourier transformation of the coupling matrices we choose an origin between two spins corresponding to decoration vectors $\mathbf{a} = (-1/2, 0), (1/2, 0)$. The couplings are given by $J(\mathbf{r}, \mathbf{r}') = J$ for nearest neighbor spins and $J(\mathbf{r}, \mathbf{r}') = 0$ for non nearest neighbor spins. Using Eq. (40) we obtain the coupling matrices

$$\mathbf{F}(\mathbf{q}) = 4JS \begin{pmatrix} 1 & 0 \\ 0 & 1 \end{pmatrix}, \quad (54)$$

$$\mathbf{G}(\mathbf{q}) = 4JS\gamma(\mathbf{q}) \begin{pmatrix} 1 & 0 \\ 0 & -1 \end{pmatrix}, \quad (55)$$

where the form factor is given by $\gamma(\mathbf{q}) = \frac{1}{2}[\cos(q_x) + \cos(q_y)]$. The squared magnon energies are the eigenvalues of the matrix $\mathbf{W}^2 = \mathbf{M}^{-1/2}\mathbf{K}\mathbf{M}^{-1/2}$. Since this matrix is already diagonal,

$$\mathbf{W}^2(\mathbf{q}) = (4JS)^2[1 - \gamma^2(\mathbf{q})] \begin{pmatrix} 1 & 0 \\ 0 & 1 \end{pmatrix}, \quad (56)$$

we directly obtain a twofold degenerate band with dispersion

$$\omega(\mathbf{q}) = 4JS\sqrt{1 - \gamma^2(\mathbf{q})}. \quad (57)$$

The twofold degeneration of the magnon band reflects the equivalence of the two sublattices. With $\omega_1(\mathbf{q}) = \omega_2(\mathbf{q}) = \omega(\mathbf{q})$ the inelastic structure factor directly reduces to the compact form

$$\mathcal{S}^{\text{in}}(\mathbf{q} + \mathbf{Q}_\nu, \omega) = S \frac{M_{\nu,\nu}^{-1}(\mathbf{q})}{\omega(\mathbf{q})} \delta(\omega - \omega(\mathbf{q})). \quad (58)$$

Inserting the inverse mass matrix $\mathbf{M}^{-1} = \mathbf{F} - \mathbf{G}$ and $\omega(\mathbf{q})$ we obtain within the Brillouin zone of the square lattice (we choose $0 \leq H, K < 1$ in reciprocal lattice units)

$$\mathcal{S}^{\text{in}}(\mathbf{q}, \omega) = S \sqrt{\frac{1 - \gamma(\mathbf{q})}{1 + \gamma(\mathbf{q})}} \delta(\omega - \omega(\mathbf{q})). \quad (59)$$

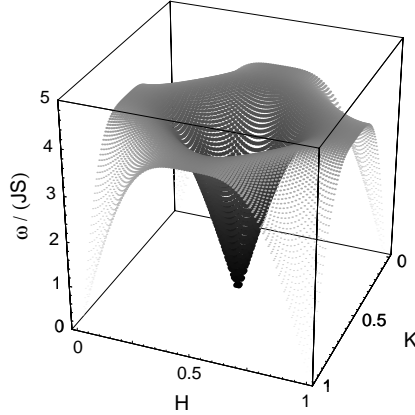


Figure 22: *Spin-wave dispersion $\omega(H, K)$ for the pure antiferromagnet. Darker points with larger size correspond to larger weight of the inelastic structure factor.*

Although the dispersion relation obeys the symmetry $\omega(\mathbf{q}) = \omega(\mathbf{q} + \mathbf{Q})$ corresponding to the period of the magnetic unit cell, this symmetry is absent in the structure factor (cf. Fig. 22). The spectral weight is concentrated in the vicinity of the antiferromagnetic wave vector $(H, K) = (1/2, 1/2) =: \mathbf{q}_{\text{AF}}$ where collective low energy excitations are observed. To leading order in $\delta\mathbf{q} = \mathbf{q} - \mathbf{q}_{\text{AF}}$, the low energy spin-wave excitations are characterized by an isotropic dispersion $\omega_{\text{AF}} \approx v_{\text{AF}} |\delta\mathbf{q}|$ with a spin-wave velocity $v_{\text{AF}} = 2\sqrt{2}JSa$.

4.2 Vertical stripes

For vertical stripes a possible magnetic unit cell is given by the base vectors $\mathbf{A}^{(1)} = (0, 2)$ and $\mathbf{A}^{(2)} = (p, 0)$ for odd or $\mathbf{A}^{(2)} = (p, 1)$ for even p . Therefore we have $N = 2p$ lattice sites per unit cell (cf. Fig. 21) and $2p$ eigenvalues $\omega_\alpha(\mathbf{q})$. Two of them (corresponding to the number of holes) vanish identically and we obtain $p - 1$ twofold degenerate physical bands. This degeneracy results from the equivalence of the two sublattices.

The lowest, acoustical band has zeros at the magnetic superstructure lattice vectors. Within the Brillouin zone of the square lattice (we choose $0 \leq H, K < 1$), the vectors \mathbf{Q}_ν are located at $(\frac{j}{p}, 0)$ and $(\frac{j}{p}, \frac{1}{2})$ for odd p or $(\frac{j}{p} + \frac{1}{2p}, \frac{1}{2})$ for even p (with $0 \leq j < p$). In the upper row of Fig. 23, we show $\omega(\mathbf{k})$ for the acoustical band as a density plot, where black corresponds to $\omega = 0$ and white to the upper band edge.

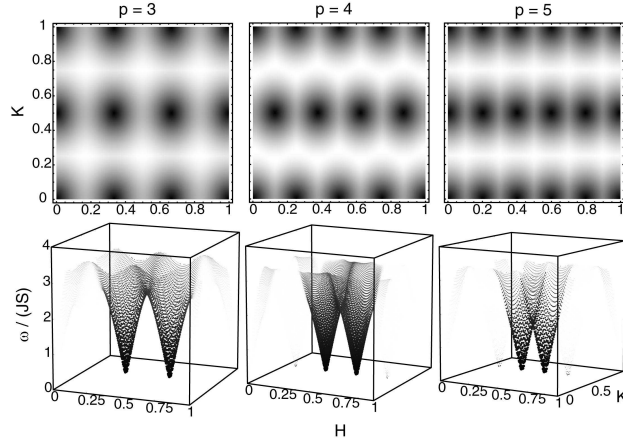


Figure 23: *Acoustical band for vertical stripes with spacings $p = 3, 4, 5$ and $\lambda = 0.5$. The upper row shows density plots of the spin-wave dispersion, where dark regions correspond to low energy values. The lower row shows the acoustical band in the (H, K, ω) space including the weight of the inelastic structure factor, where larger weight corresponds to darker points with larger size.*

Although the dispersion relation obeys the symmetry $\omega(\mathbf{k}) = \omega(\mathbf{k} + \mathbf{Q})$ corresponding to the period of the magnetic unit cell, this symmetry is absent in the structure factor. In the lower row of Fig. 23 the acoustic band is replotted in the (H, K, ω) space using darker and thicker dots for points with

larger values of the structure factor (53). In agreement with experiments, the weights are concentrated near the lowest harmonic “incommensurate” wave vectors $\mathbf{Q} = (\frac{1}{2} \pm \frac{1}{2p}, \frac{1}{2})$. Higher harmonics of the superstructure are much weaker as already noticed in Ref. [102].

To study the anisotropy of the dispersion next to the satellite positions we calculate the spin-wave velocities v_{\perp} and v_{\parallel} perpendicular and parallel to the stripe orientation (cf. Fig. 24). For $\lambda = 0$, where the coupling between the domains is switched off, v_{\perp} is zero and v_{\parallel} remains finite. With increasing λ both velocities increase, v_{\perp} stronger than v_{\parallel} . There exists a value λ^* with isotropic velocities, $v_{\perp} = v_{\parallel}$. For $p = 4$ we find $\lambda^* \approx 0.3$. In the limit $p \rightarrow \infty$ both velocities converge to v_{AF} as expected, for $p \gg 1$ we find $v_{\perp, \parallel}/v_{\text{AF}} - 1 \propto 1/p$.

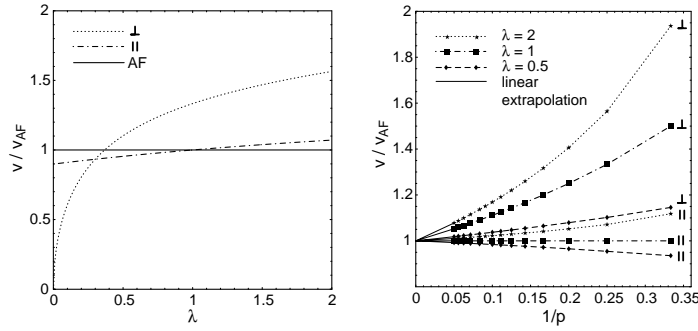


Figure 24: *Spin-wave velocities v_{\perp} and v_{\parallel} for vertical stripes with spacing $p = 4$ as a function of λ (left panel) and as a function of $1/p$ for different couplings λ (right panel; lines are a guide to the eye).*

In the special case $\lambda = 1$ the velocities are given by

$$v_{\parallel} = v_{\text{AF}}, \quad (60a)$$

$$v_{\perp} = \frac{p}{p-1} v_{\text{AF}} \quad (60b)$$

for purely geometric reasons. In this case, all spins are interacting in terms of the topology and strength of the exchange couplings exactly like in the antiferromagnet. The only difference lies in the insertion of strings of holes, which effectively stretch the lattice and increase the velocity by a factor $p/(p-1)$ in the perpendicular direction.

We now focus on the line $\mathbf{k} = (H, \frac{1}{2})$ containing the satellites, along which we plot all $p-1$ magnon bands in Fig. 25 for a variety of p and λ . For $\lambda < 1$

and $\lambda > 1$ the bands are separated by gaps. (In this context, “gaps” are not necessarily real gaps showing up in the density of states, they are apparent gaps along the chosen line.) Only for $\lambda = 1$, the structure seems to consist of displaced and intersecting antiferromagnetic bands. The value $\lambda = 1$ is special for the reasons explained above which also imply that the band width must coincide with the antiferromagnet. The purely geometric effect entails just a more complicated band structure.

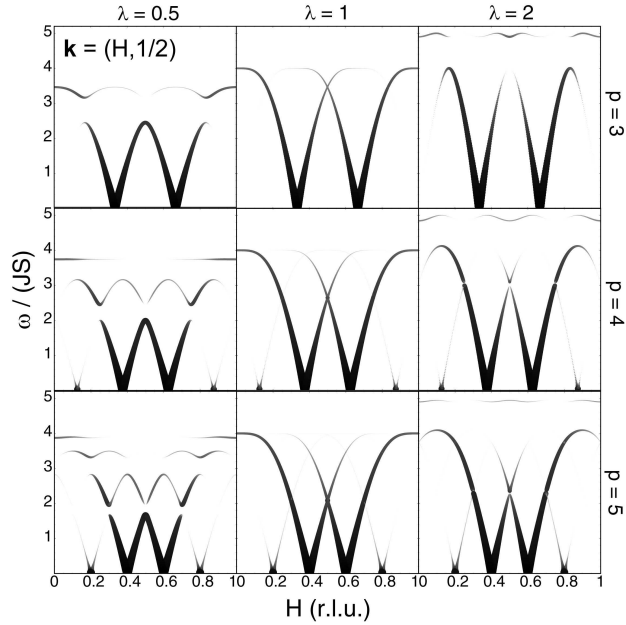


Figure 25: *Band structure for vertical stripes along the $(H, 0.5)$ direction with different spacings p and couplings λ . Darker and larger points correspond to a larger weight of the inelastic structure factor.*

To the extent to which our stripe model provides a valid description of the magnetic excitations in the materials where the π -resonance was observed, the resonance frequency has to be identified with $\omega(\mathbf{k}_{\text{AF}})$ from the lowest magnon band, provided $\omega(\mathbf{k}_{\text{AF}}) > 0$ and the structure factor has significant weight. From Fig. 25 one recognizes that for $\lambda < 1$ this is always the acoustic band. On the other hand, for $\lambda > 1$ higher bands may yield a stronger resonance (see case $p = 3$ and $\lambda = 2$). In Fig. 26 we illustrate the dependence of ω_π on λ and p .

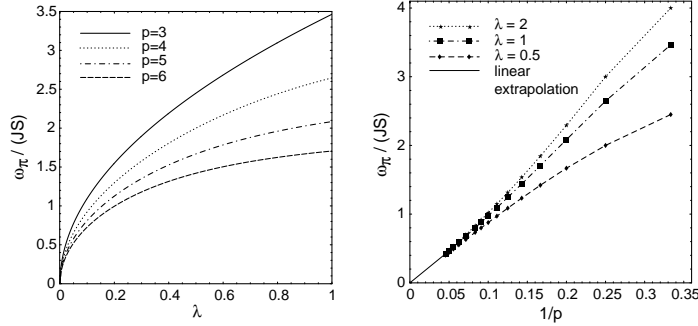


Figure 26: *The resonance frequency ω_π for vertical stripes as a function of λ for different spacings p (left) and as a function of $1/p$ for different couplings λ (right; lines are a guide to the eye).*

For p large enough such that $v_{\parallel} \approx v_{\text{AF}}$ and the magnon dispersion is roughly linear between the main satellite and \mathbf{k}_{AF} , we may estimate

$$\omega_\pi \approx v_{\text{AF}} \frac{\pi}{pa}. \quad (61)$$

This estimate becomes exact for small $1/p$ and represents the linear asymptotics in Fig. 26 (right). Deviations grow with decreasing p and increasing deviation of λ from 1.

4.3 Diagonal stripes

For diagonal stripes there are more subtle differences between even and odd stripe spacings p . Since the base vectors of the magnetic unit cell can be chosen as $\mathbf{A}^{(1)} = (-1, 1)$ and $\mathbf{A}^{(2)} = (p, 0)$ for odd or $\mathbf{A}^{(2)} = (2p, 0)$ for even p (cf. Fig. 21), we have one hole and $p - 1$ spins per unit cell for odd p and twice the number of holes and spins for even p . Like in the vertical case, the number of eigenvalues vanishing identically corresponds to the number of holes, the number of bands is given by half of the number of spins per unit cell, and the bands are twofold degenerate.

All magnetic Bragg peaks are located along the line $\mathbf{Q} = (H, H)$ with $H = j/p$ for odd and $H = j/(2p)$ for even p (cf. Fig. 27). The doubling of the zeros of the dispersion in the case of even stripe spacings reflects the doubling of the magnetic unit cell. Nevertheless, calculating the weight by the structure factor of the bands we find the strongest intensity near the

zeros of the acoustic band at the satellite positions $\mathbf{Q} = (\frac{1}{2} \pm \frac{1}{2p}, \frac{1}{2} \pm \frac{1}{2p})$ for all p . At the additional zeros resulting from the doubling of the magnetic unit cell in the case of even spacings the spectral weight strictly vanishes.

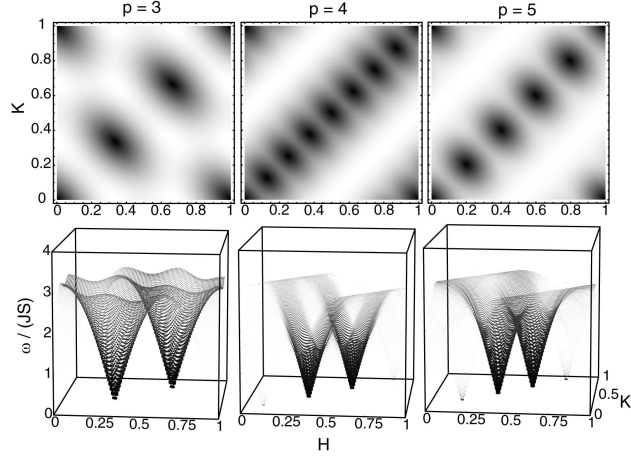


Figure 27: Acoustical band for diagonal stripes with spacings $p = 3, 4, 5$ for $\lambda = 1$ plotted in analogy to Fig. 23.

The behavior of the spin-wave velocities v_{\perp} and v_{\parallel} (cf. Fig. 28) is similar to the vertical case. Only for small values of p and small couplings λ the difference between even and odd spacings p becomes visible.

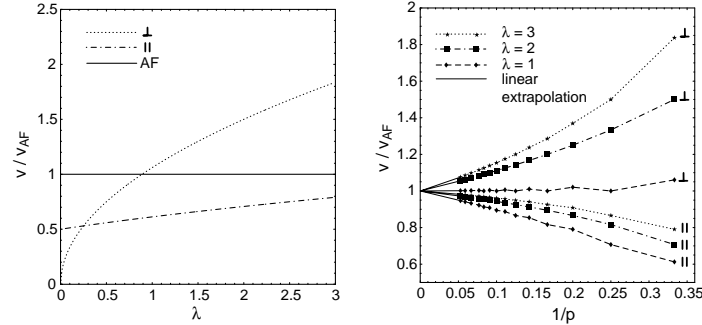


Figure 28: Spin-wave velocities v_{\perp} and v_{\parallel} for diagonal stripes with spacing $p = 3$ as a function of λ (left) and as a function of $1/p$ for different couplings λ (right; lines are a guide to the eye).

In the simplest case $p = 3$ where we only have one twofold degenerated

acoustical band we can calculate the dispersion analytically and find

$$\omega(H, K) = 2JS \left\{ \sin^2 [\pi(H - K)] + \lambda \sin^2 [\pi(2H + K)] + \lambda \sin^2 [\pi(H + 2K)] \right\}^{1/2}, \quad (62a)$$

$$\omega(H, H) = 2\sqrt{2\lambda}JS |\sin(3\pi H)| \quad (62b)$$

Along the $\mathbf{k} = (H, H)$ direction, the acoustical band is separated by finite gaps from the optical bands for $\lambda \neq 2$. For $\lambda = 2$, the band structure again seems to consist of intersecting displaced antiferromagnetic bands. In contrast to the vertical case, the special value of λ is now 2 since for this value the sum of the exchange couplings to neighboring spins is as large as in the antiferromagnet. However, for diagonal stripes the topology of the couplings is different from the antiferromagnet.

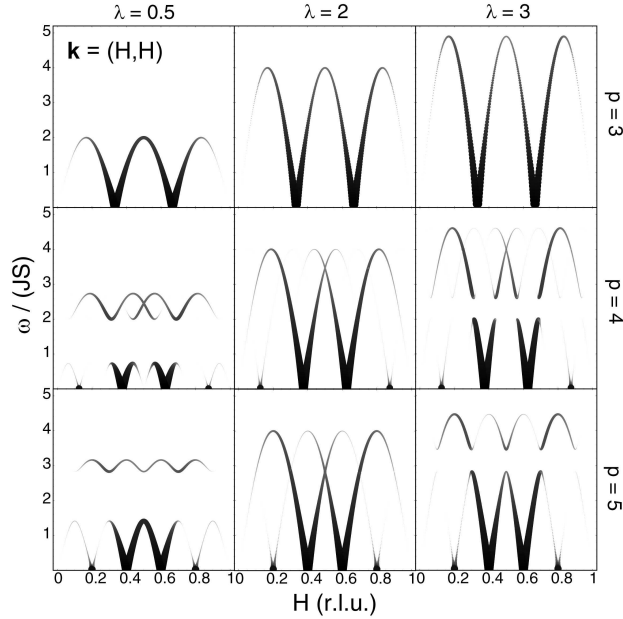


Figure 29: *Band structure for diagonal stripes along the (H, H) direction with different spacings p and couplings λ .*

For odd p , the π -resonance results from the excitation of acoustical magnons since the lowest band has a finite $\omega(\mathbf{k}_{AF})$ with a relatively strong weight. In contrast, for even p the frequency and the weight of the acoustical band

vanish at \mathbf{k}_{AF} . In this case, the π -resonance should therefore be ascribed to optical magnons. For $\lambda = 2$, the π -resonance results from the common edge of the acoustical and optical bands (cf. Fig. 29).

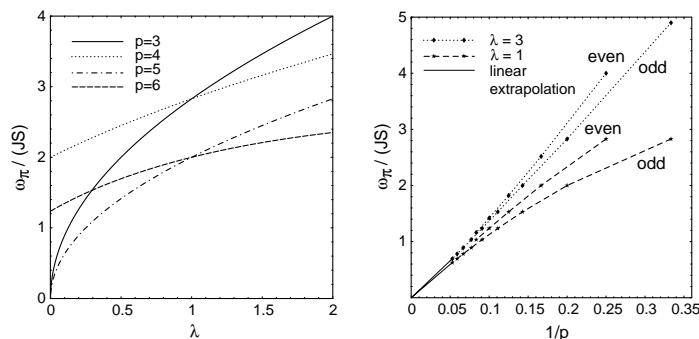


Figure 30: Resonance frequency ω_π for diagonal stripes as a function of λ for different spacings p (left) and as a function of $1/p$ for different couplings λ (right; lines are a guide to the eye distinguishing even and odd p).

With increasing coupling λ the resonance energy increases. In contrast to vertical stripes, the resonance energy remains finite in the limit $\lambda \rightarrow 0$ for even p where it arises from an optical band (cf. Fig. 30). Like for the vertical case, ω_π decreases with increasing stripe spacing, for $p \gg 1$ according to $\omega_\pi \propto 1/p$. Since resonance comes from different bands for even and odd p , ω_π is a nonmonotonous function of p . For this reason, $\omega_\pi(p)$ is plotted in Fig. 30 separately for the two cases.

4.4 Density of states

In this subsection we briefly discuss how the density of states (DOS)

$$\rho(\omega) = \sum_{\alpha} \rho_{\alpha}(\omega) \sim \sum_{\alpha} \int_{\mathbf{k}} \delta(\omega - \omega_{\alpha}(\mathbf{k})) \quad (63)$$

can be calculated numerically from the dispersion. Since $\rho_{\alpha}(\omega)d\omega$ is proportional to the number of wave vectors in the α -band in the energy range from ω to $\omega + d\omega$ the DOS can be calculated numerically by counting the number of discrete wave vectors corresponding to energies $\omega_{\alpha}(\mathbf{k})$ in a finite energy range from ω to $\Delta\omega$. The numerical resolution is limited due to the discretization of the wave vectors and the replacement $d\omega \rightarrow \Delta\omega$.

At the energies of the critical points of the dispersion which are determined by $\nabla_{\mathbf{k}}\omega_{\alpha} = 0$ the DOS shows van-Hove singularities. The shape of these singularities at ω_c depends on the dimension and the nature of the critical point. In $D = 2$ one finds $\rho_{\alpha}(\omega) \sim |\omega - \omega_c|^{-1}$ for relative maxima or minima and a logarithmic divergence at ω_c for saddle points. This can easily be seen by expanding $\omega_{\alpha}(\mathbf{k})$ around the critical point and inserting into Eq. (63).

Exemplary we present the numerically calculated DOS for the case of diagonal stripes with spacing $p = 3$. Although this case with a single band is the simplest possible, we find several critical points in the dispersion, which should result in a nontrivial shape of the DOS. Therefore we calculate this quantity just to illustrate that even for this simplest case $\rho(\omega)$ shows interesting features strongly depending on the effective coupling λ .

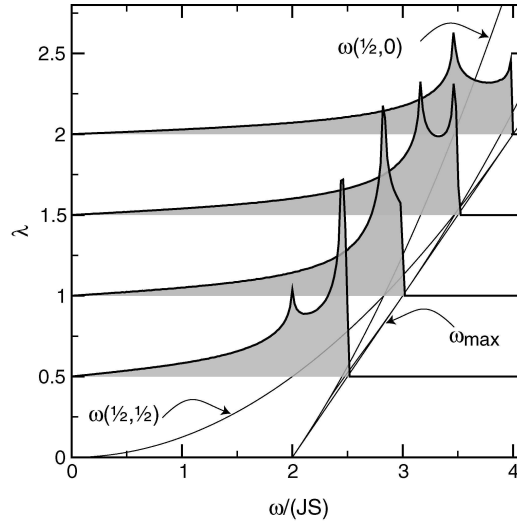


Figure 31: *Density of states $\rho(\omega)$ (height of shaded area in arbitrary units) for diagonal stripes with spacing $p = 3$ and different couplings λ . The thin lines correspond to the energies of the critical points in the dispersion. There are up to four inequivalent ones, at $\mathbf{k} = (\frac{1}{2}, \frac{1}{2})$, $\mathbf{k} = (\frac{1}{2}, 0)$, the upper band edge with ω_{max} , and a possible additional critical point.*

The numerically calculated density of states is plotted in Fig. 31 for different values of λ . The van-Hove singularities are located at the energies of the critical points in the dispersion. The dependence of these energies on the coupling λ is also shown in this figure. Due to the limited numerical and

graphical resolution the van-Hove singularities are not resolved if they are too close to each other and their precise shape is not reproduced, e.g. at the energies of the saddle points $\rho(\omega)$ should diverge logarithmically as explained before.

5 Comparison to experiments

We now discuss our findings in comparison to experimental data on the spin dynamics, which are obtained predominantly from neutron scattering. We also include experimental data for the bilayer compounds YBCO and BSCCO into our comparison though the bilayer coupling which might be relevant in these materials is neglected in our model so far.

As a result of this comparison we wish to advocate that the simple stripe model provides a fair account of the spin dynamics at not too low energies. At very low energies, spin gaps may occur, e.g., due to spin anisotropies (as in non-superconducting LNO[77] and LCO[49]), due to the coupling of spins to the superconducting order parameter (as in superconducting cuprates, see below), or simply due to the absence of antiferromagnetic order (for too small λ). Our model could straightforwardly be generalized to account for the first origin. The inclusion of superconductivity would require a major extension.

In Table 3 we have collected basic parameters for various undoped compounds setting the fundamental physical scales. In Table 4 spin dynamics data for specific stripe structures are compiled.

material	# layers	S	a	J	v_{AF}	Refs.
LNO	1	1	3.8 Å	30 meV	0.32 eV Å	[97, 109, 77]
LCO	1	$\frac{1}{2}$	3.8 Å	135 meV	0.85 eV Å	[62, 37]
YBCO	2	$\frac{1}{2}$	3.9 Å	125 meV	n/a	[97]
BSCCO	2	$\frac{1}{2}$	3.8 Å	140 meV	n/a	[97]

Table 3: *Basic parameters of the undoped parent compounds: number of layers in the crystalline unit cell, spin, nearest-neighbor spin spacing, nearest-neighbor antiferromagnetic exchange coupling, and spin-wave velocity. n/a stands for not available.*

5.1 $\text{La}_{2-x}\text{Sr}_x\text{NiO}_4$

We start the comparison with LSNO which displays diagonal stripes and where integer values of p are particularly stable [18, 20] due to a lock-in of the stripes into the atomic structure. In this material, static stripes (i.e. stripes that are visible down to $\omega = 0$) are seen at wave vectors \mathbf{Q}_ν [38]. For

material	T_c	p	ω_π	ω_{gap}	Refs.
LSNO	0K	3 (d)	80 meV	≤ 28 meV	[11]
LSCO	≈ 38 K	4 (v)	n/a	3.5 meV	[112, 82, 57]
LSCO	10K	6 (v)	25 meV	≤ 1.1 meV	[82]
LSCO	0K	≈ 43 (d)	7 meV	0 meV	[66]
YBCO	90K	5 (v)	41 meV	28 meV	[88, 74, 12]
YBCO	63K	n/a	35 meV	28 meV	[24]
YBCO	59K	n/a	26 meV	16 meV	[88]
YBCO	39K	8 (v)	23 meV	10 meV	[70]
BSCCO	91K	n/a	43 meV	n/a	[32, 40]
BSCCO	83K	n/a	38 meV	n/a	[40]

Table 4: *Spin dynamics data for different materials at various doping levels characterized by the critical temperature T_c , stripe period p and orientation (diagonal/vertical), resonance frequency ω_π , and gap frequency ω_{gap} .*

$p = 3$, the spin dynamics at higher energies has been measured in detail [11]. Similar data are also available for noninteger p , e.g. $p = 3.75$ [99].

Experiments [109, 77] on *undoped* material are in agreement with 2D spin-wave theory for the antiferromagnet with $J \approx 30$ meV. This exchange coupling corresponds to an isotropic spin-wave velocity $v_{\text{AF}} = 2\sqrt{2}SJ a = 0.32$ eVÅ [77] since $S = 1$ and $a \approx 3.8$ Å. This agreement is reasonably good over a wide energy range $\omega \gtrsim 30$ meV up to the band edge at $\omega \approx 125$ meV, at low energies $\omega \lesssim 15$ meV deviations (gaps) appear [77] due to a uniaxial spin anisotropy and weak interlayer couplings.

The spin dynamics of the stripe system was examined for $p = 3.75$ due to oxygen doping [99] as well as for $p = 3$ with Sr doping [11]. In the first case, a reduced velocity $v_{\parallel} \approx 0.6v_{\text{AF}}$ was found in direction parallel to the stripes, v_{\perp} was not resolved. In the second case, the velocity was measured in both directions and found to be remarkably isotropic and close to the value of the undoped system: $v_{\parallel} \approx 0.30$ eVÅ and $v_{\perp} \approx 0.35$ eVÅ. The overall shape of the magnon dispersion was sinusoidal with an upper edge at $\omega_\pi \approx 80$ meV (cf. Fig. 10).

In our theory, this sinusoidal shape for $p = 3$ is well reproduced [compare Fig. 29 and Eq. (62)]. The ratio $\omega_\pi/(JS) \approx 2.7$ is consistent with $\lambda \approx 0.9$. For this value of λ , $v_{\perp} \approx v_{\text{AF}}$ and $v_{\parallel} \approx 0.67v_{\text{AF}}$. Although we find v_{\parallel} to be

smaller than in Ref. [11], the overall agreement is very satisfying and provides strong support for our case that the spin dynamics can be well understood from a stripe model. Small quantitative deviations may be attributed to the simplicity of our model using only two types of exchange couplings.

Remarkably, $\lambda \approx 0.9$ implies that the spin exchange across a stripe is *not much smaller* than within an AFM domain. It is important to keep in mind that λ *must not* be too small to preserve magnetic order. A quantum Monte Carlo analysis [67] of coupled two-leg ladders ($S = 1$) indicates a quantum phase transition into a disordered state at $\lambda \approx 0.011$. Below this value, stripe order would be destroyed by quantum fluctuations.

Within our approach we can estimate also the two-magnon signal accessible by Raman spectroscopy. We may compare our single-magnon density $\rho(\omega)$ to the two-magnon scattering intensity at frequency 2ω . Certainly, this can be made only on a qualitative level, since ρ was calculated neglecting weight factors (which would change the shape of spectra but not the frequency of resonances) and because linear spin-wave theory does not include interactions between magnons. Nevertheless, it is instructive to compare the outcome from our model for the diagonal case $p = 3$ with an experiment by Blumberg *et al.* [7] on LSNO. In this experiment, two magnetic resonances are observed at $\omega \approx 4.6J$ and $\omega \approx 3J$. For $\lambda \approx 0.9$ we expect a singularity in the single-magnon density at $\omega \approx 2.7JS$ (see Fig. 31), which would correspond to a two-magnon resonance at $\omega \approx 5.4JS$. If corrections due to magnon interactions are modest, the resonance of the theory could be identified with the upper experimental one. Then the resonance at the lower frequency cannot be understood. On the other hand, for λ not too close to 1 the single-band structure for $p = 3$ would lead to several well-separated extrema but contradict the above determination of λ . In particular, for $\lambda < 1$, the additional resonance lies above ω_π since it arises from extrema close to the upper band edge and there is only a saddle-point at \mathbf{k}_{AF} . This apparent contradiction might be resolved if either interaction corrections are large, additional exchange interaction are important, or the lower experimental resonance is of different origin.

5.2 Cuprates

In the present study, we *assume* the presence of charge stripes and evaluate the spin dynamics for a simple model. The question of why stripes are formed and how stripe formation is related to superconductivity therefore cannot be

addressed. In particular, the simple spin-only model misses the coupling of spin fluctuations to the superconducting order parameter. Consequently, our analysis misses the opening of a spin gap due to superconductivity. Therefore, the spin dynamics for $\omega < \omega_{\text{gap}}$ is masked by superconductivity (see Table 4). Nevertheless, one can expect the stripe-like spin dynamics to remain visible in superconducting samples for $\omega > \omega_{\text{gap}}$. While the collective low energy excitations are governed by spin waves, at higher energies spin excitations beyond spin waves become relevant. The magnetic excitations in stripe ordered $\text{La}_{1.875}\text{Ba}_{0.125}\text{CuO}$ observed recently [103] resemble spin-waves at low energies whereas at higher energies they are very similar to spin-1 excitations of isolated spin ladders. Therefore, our analysis has its limitations also at higher energies. The experimental data in this energy range is well reproduced using a model of coupled two-leg spin ladders [105] or by mean-field calculations based on coupled dimers [107].

At low energies a spin gap has been observed in experiments on LSCO (e.g., $\omega_{\text{gap}} \simeq 3.5$ meV near optimal doping with $T_c = 38.5\text{K}$ [112, 82, 57]; a gap smaller than 1.1 meV for underdoped samples with $T_c = 12\text{K}$ and $T_c = 25\text{K}$ [82]) and on YBCO (e.g., $\omega_{\text{gap}} \simeq 10$ meV for a highly underdoped material with $T_c = 39\text{K}$ [70]; $\omega_{\text{gap}} \simeq 16$ meV for a moderately underdoped material with $T_c = 59\text{K}$ [88]; $\omega_{\text{gap}} \simeq 30$ meV for near optimal doping with $T_c = 89\text{K}$ [12]). For YBCO there is evidence [23] for a proportionality between the gap energy and the superconducting transition temperature, $\omega_{\text{gap}} \approx 3.8T_c$ which is not far away from the BCS weak-coupling limit with $\omega_{\text{gap}} = 3.52T_c$.

Furthermore – and more importantly in the present context – there is evidence for such a (rough) proportionality not only between T_c and ω_{gap} but also between T_c and ω_π ($\omega_\pi \simeq 5T_c$ for underdoped YBCO [34, 22], $\omega_\pi \simeq 5.4T_c$ for under- and overdoped BSCCO [40]). From our theory, we expect ω_π to be roughly inversely proportional to p , see Eq. (60) and Fig. 30. At low doping p should be inversely proportional to the doping level ($x + 2\delta$), i.e., ω_π should be proportional to the doping level. Such a relation was found in a previous theoretical study of the Hubbard model [25], where it was attributed to a particle-particle collective mode. Although our approach is technically much less involved, it provides an alternative explanation which is not in contradiction with the previous one since stripe order itself can be considered as a collective phenomenon that can be derived from the Hubbard model [116, 92].

On the other hand, at larger doping there is no simple relation between

the doping level and p . In YBCO, for example, the charge-transfer mechanism between the CuO_2 plane and the CuO chains interferes. In LSCO it is well documented that p saturates at $p = 4$ for $x \gtrsim 0.12$ [111]. Beyond that point (which corresponds to optimum doping [111]), additional holes may populate the antiferromagnetic domains without affecting their period p . However, these excess holes may suppress the antiferromagnetic exchange coupling in analogy to holes in the spin-glass phase (Ref. [99] reports the corresponding suppression of the spin-wave velocity). Hence, the effective J and, consequently, also ω_π may shrink with overdoping as seen in experiments on BSCCO [40].

For LSCO, so far no direct evidence for a π -resonance has been found. This could be simply because the resonance intensity is expected to be only $\sim 10\%$ of the total magnetic scattering [9]. However, if the π resonance – in the sense of a merger of the incommensurate signals – can be attributed to magnons in stripes which are particularly well established for LSCO, one definitely has to expect such a resonance. For underdoped LSCO ($p = 6$, $T_c = 25\text{K}$) there is evidence for $\omega_\pi = 25$ meV (where incommensurate response becomes commensurate) [82]. A similar signal was observed at even lower doping in the spin-glass phase ($\omega_\pi = 7$ meV for $p \approx 43$) [66].

Like for LSNO, we may use the values of J , p , and ω_π to estimate λ for the cuprates. For YBCO with $J = 125$ meV, $p = 5$, and $\omega_\pi = 41$ meV [12, 23], we obtain $\lambda \sim 0.07$ from the left panel of Fig. 26. If we take $J = 135$ meV and $\omega_\pi = 25$ meV for LSCO with $p = 6$ [82], an even smaller value $\lambda \sim 0.04$ is found.

From this result we may predict where the resonance ω_π should be expected in LSCO near optimal doping ($p = 4$). For $J = 135$ meV and $\lambda = 0.04 - 0.07$ we find $\omega_\pi \approx 40 - 52$ meV. While the resulting values for ω_π have a certain spread, they suggest that the resonance frequency should be at least as large as in optimally doped YBCO.

In the experiments known to us, the considered energy range was simply too small to detect the resonance for optimally doped LSCO: $\omega \lesssim 6$ meV in [112], $\omega \lesssim 10$ meV in Refs. [111, 58], $\omega \leq 16$ meV in Ref. [57]. However, from pulsed neutron scattering evidence has been found for a broad peak in the momentum-integrated susceptibility between 40 and 70 meV [110, 1] which could be ascribed to the π -resonance.

Apparently, λ seems to be significantly smaller in the cuprates than in the nickelates. At the same time, S is smaller (although J is larger). Therefore one may wonder whether static magnetic stripe order is already destroyed by

quantum fluctuations without invoking competing orders leading to a gap. For $S = \frac{1}{2}$ the coupling needs to satisfy $\lambda \gtrsim 0.3$ to stabilize spin order for $p = 3$ [104, 67], while for $p = 4$ a finite $\lambda > 0$ is sufficient [104]. For $p = 5$ (as for every odd p) one again expects a finite critical λ . If the interstripe coupling is below this value, the presence of a spin gap can be understood also within the spin-only model.

6 Conclusion

In summary, we find that the spin fluctuations of stripes can provide a simple and valuable description of the dynamics observed in high- T_c compounds and related materials. Already our minimalistic spin-only model provides an accurate account of experiments on LSNO and possibly also a unifying framework for incommensurate response and the π resonance in the cuprates. While such a framework has been suggested recently [3], it is analyzed and evaluated here for the most transparent case of integer periods p . Our results unravel the evolution of the band structure with p for diagonal and vertical stripe configurations. Likewise, we have explicitly determined the dependence of characteristic spin-wave velocities and of the resonance frequency on p and λ . Thereby, we postulate that the π resonance reflects the magnon frequency ω_π of the lowest lying band with nonvanishing weight. In particular, ω_π was found to be roughly inversely proportional to p in agreement with experiments. A similar analysis for bond-centered stripes [14] performed recently suggests that there are qualitative differences between bond- and site-centered stripes, in particular, bond-centered stripes produce more magnon bands than their site-centered counterparts and in the case of odd stripe spacings the bond-centered stripes exhibit more elastic peaks than the site-centered ones. Furthermore for bond-centered configurations, rather isotropic spin-wave cones are predicted for a wide range of parameters.

Hopefully, future experiments can provide more direct evidence for the π resonance also in LSCO. This would also relax the controversial question, whether spin excitations in LSCO and YBCO are analogous [72] or not [12]. If stripe magnons indeed explain the spin dynamics at intermediate energies, as we expect, they would provide a unifying framework for understanding the spin dynamics above the gap scale. Then the stripe physics would be also of great importance as basement for superconductivity as low-energy phenomenon.

Naturally, several aspects remain unexplained by our minimalistic theory. For example, our model cannot be expected to explain why the magnetic incommensurability disappears at T_c in YBCO [12] while charge order is visible up to 300 K [70]. This is probably a question to the stripe-forming mechanism and to a possible coupling between the order parameters for stripe order and superconductivity. In LSCO, the vicinity of soft phonons and structural instabilities may help to stabilize stripes at temperatures above the superconducting transition.

For future studies it would be interesting to include effects of the bilayer coupling present in YBCO and BSCCO, of the weak 3D coupling present in all materials, as well as spin anisotropy, more complicated spin interactions (e.g. four-spin cyclic exchange[97, 75]), excitations beyond spin waves (e.g. double-spin excitations [7]), mobility of spins, and effects of disorder, to name just a few.

7 Bilayer model

In the previous sections we have studied the spin-wave excitations of a monolayer stripe system using a simple real space spin-only model. Already this minimalistic model provides an accurate account of experiments on LSNO and possibly also a unifying framework for incommensurate response and the π -resonance in the cuprates. From the comparison to experimental data we fixed the relative coupling λ across a stripe as the only a priori unknown model parameter. While in the case of LSNO the exchange coupling across a stripe was not much smaller than within an antiferromagnetic domain ($\lambda \approx 0.9$), in the cuprates the coupling between the domains was found to be much smaller, $\lambda \approx 0.04 - 0.07$. Since, for almost undoped YBCO, the bilayer coupling is only one order of magnitude smaller than the antiferromagnetic nearest neighbor exchange within the layers [85], it is not justified to neglect the interlayer couplings within a bilayer. Therefore we extend the minimalistic spin-only model introduced in section 2 to a bilayer model.

As before, within one layer we assume the holes to form parallel site-centered rivers, which act as anti-phase boundaries for the antiferromagnetic spin domains in between and choose the simplest possible implementation of exchange couplings stabilizing this magnetic structure: antiferromagnetic exchange couplings J between neighboring spins within the domains and antiferromagnetic couplings λJ between closest spins across a stripe.

Here we focus on vertical stripes as observed in the superconducting cuprates and, for simplicity, restrict our analysis to the representative case of a stripe spacing $p = 4$. This corresponds to a doping of one hole per 8 Cu sites since the rivers have a line charge of only half a hole per lattice constant.

In addition to the in-plane couplings we consider an antiferromagnetic exchange μJ between two layers (cf. Fig. 32). The Hamiltonian of this bilayer model is given by

$$H = \sum_{\alpha=1,2} H_{\alpha} + H_{1,2}, \quad (64a)$$

$$H_{\alpha} = \frac{1}{2} \sum_{\mathbf{r}, \mathbf{r}'}^* J_{\alpha}(\mathbf{r}, \mathbf{r}') \mathbf{S}_{\alpha}(\mathbf{r}) \mathbf{S}_{\alpha}(\mathbf{r}'), \quad (64b)$$

$$H_{1,2} = \mu J \sum_{\mathbf{r}}^* \mathbf{S}_1(\mathbf{r}) \mathbf{S}_2(\mathbf{r}), \quad (64c)$$

where \mathbf{r} specifies the square-lattice position and $\alpha = 1, 2$ numbers the layers. The asterisks indicate that the sums do not include positions of charge rivers. The in-plane couplings $J_\alpha(\mathbf{r}, \mathbf{r}')$ defined in the text above are illustrated in Fig. 32. They explicitly depend on the layer index if the charge distribution is different in both layers.

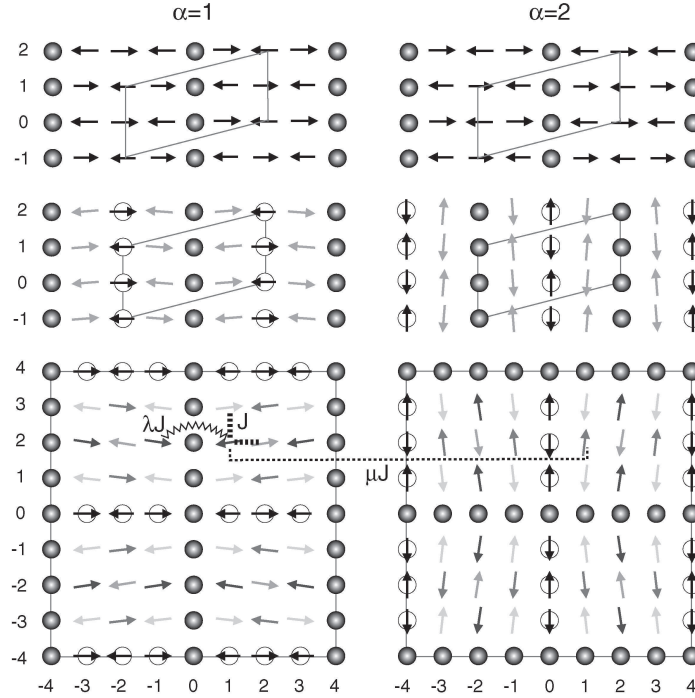


Figure 32: *Classical ground states for bilayer systems with parallel (upper row), shifted parallel (middle row), and perpendicular hole stripes (lower row) for a stripe spacing $p = 4$. The exchange couplings of the simple model are illustrated in the lower row: AF couplings $J > 0$ for nearest neighbors within the domains (bold dashed), λJ between nearest neighbors across a hole stripe (zig-zag) and couplings μJ between spins one above the other (dashed). Frustration of exchange coupling may lead to a canting of spins (calculated for $\mu = 0.09$ and $\lambda = 0.07$ in the middle and bottom row, respectively). Possible magnetic unit cells are outlined by gray lines, identical gray levels of spins correspond to identical canting angles.*

The actual stripe configuration is determined by several influences. Besides the magnetic exchange energy one also has to take into account the

Coulomb energy, and in principle also a further reduction of the fourfold symmetry of CuO_2 planes in orthorhombic structures which may favor a certain alignment of the stripes. In $\text{YBa}_2\text{Cu}_3\text{O}_{6+x}$ the formation of CuO chains along the b -direction may favor a parallel alignment of stripes.

We find that three different stripe configurations may be realized physically (see Fig. 32). The exchange energy favors *parallel stripes* lying exactly on top of each other. This configuration is free of magnetic exchange frustration, each bond can be fully saturated. However, this configuration is disfavored by the Coulomb energy which would favor a configuration where stripes are *parallel but shifted* with respect to each other by half a stripe spacing. (In our simple model, where holes are assumed to be site centered, this configuration is only compatible with even stripe spacings p .) The gain in Coulomb energy has to be paid by a loss of exchange energy. For certain parameters, a third configuration may be favorable, where the charge stripes of the two layers are *perpendicular*.

For the later analysis it is instructive to anticipate that for these configurations the Hamiltonian has discrete symmetries. We focus on symmetries involving an exchange of layers. For parallel and shifted parallel stripes, this symmetry is just the reflection $z \rightarrow -z$ combined with a translation (coordinates are chosen such that the planes are parallel to the xy plane). For perpendicular stripes, one needs to add a rotation around the z axis.

7.1 Energetic estimates

To estimate the Coulomb energy for the three stripe configurations, we assume a charge-density modulation $\rho(\mathbf{r}) = \rho_1(\mathbf{r})\delta(z) + \rho_2(\mathbf{r})\delta(z-d)$ with $\rho_\alpha(\mathbf{r}) = \rho_\alpha^{(0)} \cos(\mathbf{k}_\alpha \mathbf{r})$ where the planes with distance d are perpendicular to the z -direction. For simplicity, only the first harmonic of the charge modulation is retained. Parallel stripes are described by $\mathbf{k}_1 = \mathbf{k}_2 = k\mathbf{e}_x$ and $\rho_1^{(0)} = \rho_2^{(0)} = \bar{\rho}$, shifted parallel stripes are realized for $\mathbf{k}_1 = \mathbf{k}_2 = k\mathbf{e}_x$ and $\rho_1^{(0)} = -\rho_2^{(0)} = \bar{\rho}$, and perpendicular stripes for $\mathbf{k}_1 = k\mathbf{e}_x$, $\mathbf{k}_2 = k\mathbf{e}_y$ and $\rho_1^{(0)} = \rho_2^{(0)} = \bar{\rho}$. For a stripe spacing pa the charge-modulation wave vectors are given by $k = 2\pi/(pa)$, the amplitude by $\bar{\rho} = e/(2pa^2)$. Calculating the Coulomb coupling energy per square lattice site

$$E_C = \frac{1}{4\pi\epsilon_0} \frac{a^2}{A} \int d^3r \int d^3r' \frac{\rho_1(\mathbf{r})\rho_2(\mathbf{r}')}{|\mathbf{r} - \mathbf{r}'|}, \quad (65)$$

where A denotes the area of the planes, we find, in the limit $A \rightarrow \infty$, a vanishing Coulomb coupling for perpendicular stripes, an energy cost

$$\Delta E_C = \frac{e^2}{32\pi\epsilon_0 pa} \exp\left(-2\pi\frac{d}{pa}\right) \quad (66)$$

for parallel stripes, and an energy gain of the same size for shifted parallel stripes. For YBCO with $a \approx 3.85 \text{ \AA}$, $d \approx 3.34 \text{ \AA}$, $J = 125 \text{ meV}$, $S = \frac{1}{2}$ and for a stripe spacing $p = 4$ we obtain $\Delta E_C \approx 29 \text{ meV}$.

For antiferromagnetic YBCO the magnetic interlayer superexchange is reported to be $\mu \approx 0.08$ [85]. For parallel stripes, spins are not frustrated and, in a classical picture, antiparallel in different layers, $\mathbf{S}_1(\mathbf{r}) = -\mathbf{S}_2(\mathbf{r})$. Thus, the exchange coupling roughly leads to an energy gain of order $\mu JS^2 \approx 3 \text{ meV}$, whereas the energy gain will be smaller for the other two configurations due to frustration.

Thus, within our rough estimate, the Coulomb energy appears to be up to one order of magnitude larger than the exchange energy, such that one might expect the parallel shifted configuration to be the only physical one. On the other hand the actual Coulomb energy may be significantly smaller than the result of our estimate since we have completely neglected screening. For almost undoped YBCO a relatively large value of $\epsilon \approx 15$ for the static dielectric constant at $T = 4\text{K}$ is reported [89]. Therefore the Coulomb energy might be of the same order of magnitude as the magnetic exchange energy. Due to the crudeness of our estimate no stripe configuration can be strictly ruled out.

7.2 Classical ground states

Due to frustration effects, the ground-state structure is nontrivial for shifted parallel and perpendicular stripes. We now determine these ground states treating spins as classical. These ground states will be a necessary prerequisite for the subsequent spin-wave analysis. We continue to focus on the representative case $p = 4$.

Depending on the values of the couplings λ and μ we find two different types of ground states. For a nearest neighbor exchange across a stripe in the range $0 < \lambda < \lambda_c$ ($\lambda_c \approx 0.59$ for shifted parallel and $\lambda_c \approx 0.35$ for perpendicular stripes) the ground state has a canted planar topology up to a value $\mu_c(\lambda)$ of the interlayer exchange (cf. Fig. 33). For $\mu > \mu_c(\lambda)$ spins lock into a collinear texture.

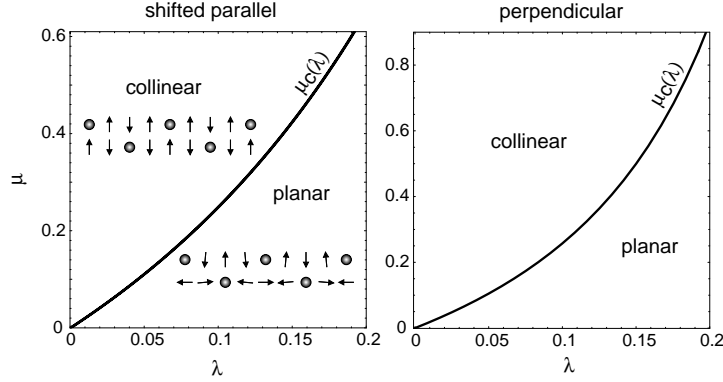


Figure 33: Classical ground-state phase diagrams for shifted parallel and perpendicular stripes. For $\mu < \mu_c(\lambda)$ the ground states show a canted planar spin pattern illustrated in Fig. 32. For $\mu > \mu_c(\lambda)$ the topology of the ground states changes into a collinear pattern where spins lying on top of each other are strictly antiparallel and nearest neighbors across a stripe are parallel. For $\lambda \rightarrow \lambda_c$ ($\lambda_c \approx 0.59$ for shifted parallel and $\lambda_c \approx 0.35$ for perpendicular stripes) μ_c goes to infinity. Above λ_c the ground states are always planar.

To characterize these different phases, we start with the planar one. As already indicated above, the frustration can lead to a canting of spins. The origin of the canting is easily understood. For $\mu = 0$ the layers are decoupled and the sublattice magnetization in both layers can have an arbitrary relative orientation. For small interlayer coupling μ the spins start to cant starting from a configuration where spins lying on top of each other are perpendicular. Only in this case the interlayer couplings lead to an energy gain proportional to small canting angles while the intralayer couplings lead to an energy cost of second order in the canting angles. Such canted planar ground states are illustrated in Fig. 32. In Fig. 34 the corresponding tilting angles are plotted for $\lambda = 0.1$ as a function of μ . The tilting angles increase monotonously in a way that spins lying on top of each other become increasingly antiparallel with increasing μ .

In the other phase, for $\mu > \mu_c(\lambda)$, the interlayer coupling μ dominates the coupling λ across the stripes and the topology of the ground state changes into a collinear configuration where the spins lying on top of each other are strictly antiparallel and nearest neighbor spins across a stripe are strictly parallel although they are antiferromagnetically coupled. This configuration

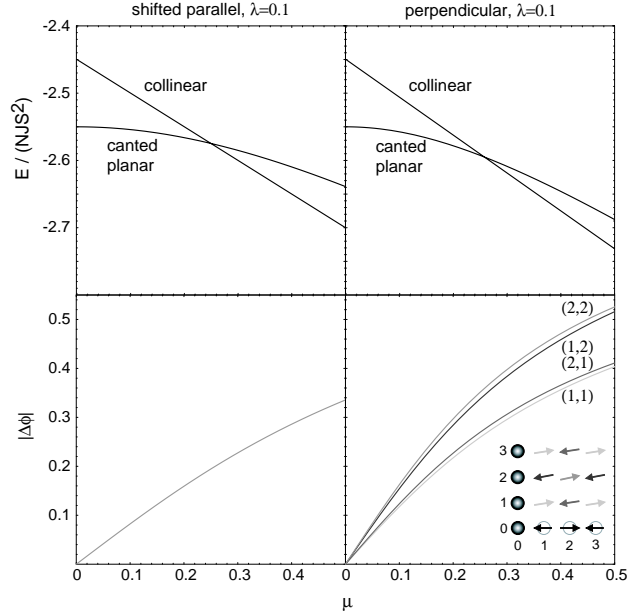


Figure 34: Upper row: Energy per lattice site in units of JS^2 as a function of μ for $\lambda = 0.1$. For both stripe configurations the energies of the canted planar and the collinear spin pattern are plotted. The curves intersect at $\mu = \mu_c$ where the topology of the ground states changes. Lower row: Relative values of the tilting angles of the spins in the planar configuration as a function of the interlayer coupling μ for $\lambda = 0.1$.

is stable against a canting of the spins because for small λ the energy gain for λ -bonds and the energy costs for μ -bonds as well as the couplings within the domains would be quadratic in the tilting angles. Since this ground state has lost the antiphase-boundary character of the charge stripes it resembles a diluted antiferromagnet. This would lead to a static magnetic response at the antiferromagnetic wave vector in disagreement with experimental observations. Therefore, these collinear phases probably are not relevant for the magnetic properties of the cuprate compounds.

For small values of λ the phase boundary is approximately given by $\mu_c(\lambda) \approx 2\lambda$ for both stripe configurations (cf. Fig. 33). In the limit $\lambda \rightarrow \lambda_c$ the critical value μ_c goes to infinity. Above λ_c the ground states remain canted planar for all values of the interlayer coupling μ .

Comparing the classical magnetic ground-state energies for the two frus-

trated configurations, we find that – in contrast to the Coulomb energy – the exchange coupling favors perpendicular stripes over shifted parallel stripes. For this reason we retain perpendicular stripes in our consideration.

8 Bilayer modifications of spin-wave theory

In this analytic part the expressions for the magnon band structure and the spectral weight at zero temperature are generalized to a bilayer. Since the analysis is similar to that for a single layer (see Sec. 3), here we only elaborate on the substantial differences. The general expressions derived in this section are evaluated numerically later on in Sec. 9 for parallel, shifted parallel and perpendicular stripes with fixed stripe spacing $p = 4$.

The ground-state analysis of the preceding section has made clear that spin waves now have to be introduced as excitation of a non-collinear ground state. However, our numerical calculation of the classical ground states have shown planar spin textures (here, a collinear texture is considered as a special subcase of a planar texture).

In the following we consider a general planar ground state which can be captured by a vector field $\mathbf{S}_\alpha(\mathbf{r}) = \{\cos \phi_\alpha(\mathbf{r}), \sin \phi_\alpha(\mathbf{r}), 0\}$, where the tilting angles of the spins obey the translational symmetry $\phi_\alpha(\mathbf{r}) = \phi_\alpha(\mathbf{r} + \mathbf{A})$ for an arbitrary magnetic lattice vector $\mathbf{A} = m_1 \mathbf{A}^{(1)} + m_2 \mathbf{A}^{(2)}$. For the spin textures displayed in Fig. 32, corresponding magnetic unit cells are given by $\mathbf{A}^{(1)} = (4, 1)$ and $\mathbf{A}^{(2)} = (0, 2)$ for parallel stripes and for shifted parallel stripes, and by $\mathbf{A}^{(1)} = (8, 0)$ and $\mathbf{A}^{(2)} = (0, 8)$ for perpendicular stripes.

To study the quantum fluctuation around the classical ground state we rotate all spins by their planar angles $\phi_\alpha(\mathbf{r})$ according to

$$S_\alpha^x(\mathbf{r}) = \tilde{S}_\alpha^x(\mathbf{r}) \cos \phi_\alpha(\mathbf{r}) - \tilde{S}_\alpha^y(\mathbf{r}) \sin \phi_\alpha(\mathbf{r}), \quad (67a)$$

$$S_\alpha^y(\mathbf{r}) = \tilde{S}_\alpha^x(\mathbf{r}) \sin \phi_\alpha(\mathbf{r}) + \tilde{S}_\alpha^y(\mathbf{r}) \cos \phi_\alpha(\mathbf{r}), \quad (67b)$$

$$S_\alpha^z(\mathbf{r}) = \tilde{S}_\alpha^z(\mathbf{r}), \quad (67c)$$

such that $\tilde{\mathbf{S}}(\mathbf{r})$ has a classical ferromagnetic ground state $\tilde{\mathbf{S}}(\mathbf{r}) = S\{1, 0, 0\}$. In the transformed spin basis we introduce Holstein-Primakoff (HP) bosons in the standard way (using $\tilde{S}^\pm = \tilde{S}^y \pm i\tilde{S}^z$),

$$\tilde{S}_\alpha^+(\mathbf{r}) = \sqrt{2S - \hat{n}_{\mathbf{r},\alpha}} b_{\mathbf{r},\alpha}, \quad (68a)$$

$$\tilde{S}_\alpha^-(\mathbf{r}) = b_{\mathbf{r},\alpha}^\dagger \sqrt{2S - \hat{n}_{\mathbf{r},\alpha}}, \quad (68b)$$

$$\tilde{S}_\alpha^x(\mathbf{r}) = -\hat{n}_{\mathbf{r},\alpha} + S, \quad (68c)$$

and obtain the spin-wave Hamiltonian

$$\begin{aligned} \mathcal{H}_{\text{sw}} = & \frac{S}{2} \sum_{\mathbf{r}, \mathbf{r}'}^* \sum_{\alpha, \alpha'} \left\{ f_{\alpha, \alpha'}(\mathbf{r}, \mathbf{r}') \left[b_{\mathbf{r}\alpha}^\dagger b_{\mathbf{r}'\alpha'} + b_{\mathbf{r}\alpha} b_{\mathbf{r}'\alpha'}^\dagger \right] \right. \\ & \left. + g_{\alpha, \alpha'}(\mathbf{r}, \mathbf{r}') \left[b_{\mathbf{r}\alpha} b_{\mathbf{r}'\alpha'} + b_{\mathbf{r}\alpha}^\dagger b_{\mathbf{r}'\alpha'}^\dagger \right] \right\}, \end{aligned} \quad (69)$$

where the functions f and g are defined by

$$\begin{aligned} f_{\alpha, \alpha'}(\mathbf{r}, \mathbf{r}') &= \frac{1}{2} [J_\alpha(\mathbf{r}, \mathbf{r}') \delta_{\alpha, \alpha'} + \mu J \delta_{\mathbf{r}, \mathbf{r}'} (1 - \delta_{\alpha, \alpha'})] \\ &\quad \times [\Delta_{\alpha, \alpha'}(\mathbf{r}, \mathbf{r}') + 1] \\ &\quad - \delta_{\mathbf{r}, \mathbf{r}'} \delta_{\alpha, \alpha'} \sum_{\mathbf{r}''} J_\alpha(\mathbf{r}, \mathbf{r}'') \Delta_{\alpha, \alpha'}(\mathbf{r}, \mathbf{r}'') \\ &\quad - \mu J \delta_{\mathbf{r}, \mathbf{r}'} \delta_{\alpha, \alpha'} \sum_{\alpha''} (1 - \delta_{\alpha, \alpha''}) \Delta_{\alpha, \alpha''}(\mathbf{r}, \mathbf{r}') \\ g_{\alpha, \alpha'}(\mathbf{r}, \mathbf{r}') &= \frac{1}{2} [J_\alpha(\mathbf{r}, \mathbf{r}') \delta_{\alpha, \alpha'} + \mu J \delta_{\mathbf{r}, \mathbf{r}'} (1 - \delta_{\alpha, \alpha'})] \\ &\quad \times [\Delta_{\alpha, \alpha'}(\mathbf{r}, \mathbf{r}') - 1] \\ \Delta_{\alpha, \alpha'}(\mathbf{r}, \mathbf{r}') &= \cos[\phi_\alpha(\mathbf{r}) - \phi_{\alpha'}(\mathbf{r}')]. \end{aligned} \quad (70a)$$

$$(70a)$$

$$\Delta_{\alpha, \alpha'}(\mathbf{r}, \mathbf{r}') = \cos[\phi_\alpha(\mathbf{r}) - \phi_{\alpha'}(\mathbf{r}')]. \quad (70b)$$

From now on we can proceed exactly in the same way as in section 3. We Fourier transform the bosonic operators and use the same decompositions for the lattice vectors and the wave vectors and obtain

$$\begin{aligned} \mathcal{H}_{\text{sw}} = & \frac{1}{2} \int_{\mathbf{q}} \sum_{\nu, \nu'} \sum_{\alpha, \alpha'} \left\{ F_{\nu\alpha, \nu'\alpha'}(\mathbf{q}) [b_{\alpha, \mathbf{q}+\mathbf{Q}_\nu}^\dagger b_{\alpha', \mathbf{q}+\mathbf{Q}_{\nu'}} + b_{\alpha, -\mathbf{q}-\mathbf{Q}_\nu} b_{\alpha', -\mathbf{q}-\mathbf{Q}_{\nu'}}^\dagger] \right. \\ & \left. + G_{\nu\alpha, \nu'\alpha'}(\mathbf{q}) [b_{\alpha, \mathbf{q}+\mathbf{Q}_\nu}^\dagger b_{\alpha', -\mathbf{q}-\mathbf{Q}_{\nu'}}^\dagger + b_{\alpha, -\mathbf{q}-\mathbf{Q}_\nu} b_{\alpha', \mathbf{q}+\mathbf{Q}_{\nu'}}] \right\}, \end{aligned} \quad (71)$$

where F and G are related to f and g due to Eq.(40).

The Hamiltonian (71) has exactly the same structure as in the monolayer case [compare Eq. (39) in section 3] and can be diagonalized by a Bogoliubov transformation in an analogous way. The final diagonal form is given by

$$\mathcal{H}_{\text{sw}} = \sum_{\gamma=1}^{2n} \int_{\mathbf{q}} \omega_\gamma(\mathbf{q}) \left\{ b_\gamma^\dagger(\mathbf{q}) b_\gamma(\mathbf{q}) + \frac{1}{2} \right\}, \quad (72)$$

where n denotes the number of spins and holes in the magnetic unit cell (corresponding to the area of the cell). The squared energies ω_γ^2 are eigenvalues of the hermitian matrix $\mathbf{M}^{-1/2}\mathbf{K}\mathbf{M}^{-1/2}$. Thereby $\mathbf{M}^{-1} = \mathbf{F} - \mathbf{G}$ denotes the inverse mass matrix and $\mathbf{K} = \mathbf{F} + \mathbf{G}$ the coupling matrix.

We now proceed to calculate the inelastic zero-temperature structure factor. Here we distinguish between even and odd excitations with respect to the two layers,

$$\mathcal{S}_\pm^{\text{in}}(\mathbf{k}, \omega) := \sum_{\mathbf{F}} \sum_{j=x,y,z} |\langle \mathbf{F} | S_1^j(\mathbf{k}) \pm S_2^j(\mathbf{k}) | 0 \rangle|^2 \times \delta(\omega - \omega_{\mathbf{F}}), \quad (73)$$

where $|0\rangle$ denotes the magnon vacuum characterized by $b_\gamma(\mathbf{q})|0\rangle = 0$. We consider only single-magnon final states $|\mathbf{F}\rangle = b_\gamma^\dagger(\mathbf{q})|0\rangle$ with excitation energy $\omega_{\mathbf{F}} := E_{\mathbf{F}} - E_0$. $\mathbf{k} = (k_x, k_y)$ denotes the in-plane wave-vector, odd excitations correspond to $k_z^- = (2n+1)\pi/d$ [$L^- = (2n+1)c/(2d)$ in reciprocal lattice units], even ones to $k_z^+ = 2n\pi/d$ ($L^+ = nc/d$), where d is the distance of the two layers within the orthorhombic unit cell. For YBCO with $d \approx 3.34 \text{ \AA}$ and $c \approx 11.7 \text{ \AA}$ the corresponding values for even and odd modes are $L^- \approx 1.75, 5.25$ and $L^+ \approx 0, 3.5$.

Expressing the spin operators by the final bosonic operators $b_\gamma(\mathbf{q})$ it is straightforward to calculate the structure factor. Using a pseudo-Dirac notation and denoting the $2n$ -dimensional cartesian basis by $|\nu, \alpha\rangle$ ($\nu = 1, \dots, N, \alpha = 1, 2$) and the orthonormal eigenbasis of $\mathbf{M}^{-1/2}\mathbf{K}\mathbf{M}^{-1/2}$ by $|\gamma\rangle$, the structure factor can be rewritten in a compact form,

$$\mathcal{S}_\pm^{\text{in}}(\mathbf{q} + \mathbf{Q}_\nu, \omega) = S \sum_{\gamma} \mathcal{S}_\gamma^\pm(\mathbf{q} + \mathbf{Q}_\nu) \delta(\omega - \omega_\gamma(\mathbf{q})), \quad (74a)$$

$$\mathcal{S}_\gamma^\pm(\mathbf{q} + \mathbf{Q}_\nu) = \frac{1}{2} \sum_{\mathbf{X}=\mathbf{C}, \mathbf{S}, \frac{\mathbf{K}}{\omega_\gamma}} \langle\langle \nu, \pm | \mathbf{X} \mathbf{M}^{-1/2} | \gamma \rangle\rangle \frac{1}{\omega_\gamma} \langle\langle \gamma | \mathbf{M}^{-1/2} \mathbf{X} | \nu, \pm \rangle\rangle, \quad (74b)$$

where we have defined $|\nu, \pm\rangle = (1/\sqrt{2})[|\nu, 1\rangle \pm |\nu, 2\rangle]$ and introduced the matrices \mathbf{S} and \mathbf{C} according to

$$s_{\nu\alpha, \nu'\alpha'} = \frac{1}{n} \delta_{\alpha\alpha'} \sum_{\mathbf{a}}^* \sin \phi_\alpha(\mathbf{a}) e^{i(\mathbf{Q}_\nu - \mathbf{Q}_{\nu'})\mathbf{a}}, \quad (75a)$$

$$c_{\nu\alpha, \nu'\alpha'} = \frac{1}{n} \delta_{\alpha\alpha'} \sum_{\mathbf{a}}^* \cos \phi_\alpha(\mathbf{a}) e^{i(\mathbf{Q}_\nu - \mathbf{Q}_{\nu'})\mathbf{a}}. \quad (75b)$$

9 Bilayer results

We now evaluate the magnon dispersion and the inelastic structure factor for even and odd excitations numerically. From a comparison of our findings for the monolayer system to neutron scattering data for the cuprate compounds we found (see Sec. 4) the coupling λJ across a stripe to be about one order of magnitude smaller than the nearest neighbor coupling J within the domains. For the coupling μJ between the layers a value $\mu \approx 0.08$ is reported [85] for antiferromagnetic YBCO in the absence of stripes. Therefore in the stripe system the couplings λ and μ can be assumed to be of the same order. In the following we keep the value of λ fixed and discuss the effects of increasing μ starting from the case of decoupled layers ($\mu = 0$) where the band structure of the monolayer system (see Sec. 4) should be recovered. In this parameter regime the classical ground states for shifted parallel and perpendicular charge stripes show the canted planar texture and the antiphase domain boundary character of the charge stripe is weakened by the interlayer coupling but still pronounced. Finally we shortly present the excitation spectra for shifted parallel and perpendicular stripes for parameters belonging to the collinear ground state regime.

In the case of decoupled layers ($\mu = 0$) the results of the monolayer system are trivially recovered. Since the two layers are uncorrelated, the structure factor does not depend on the L component of the wave vector. For parallel stripes (with or without a relative shift of the stripes) where the charge modulation is unidirectional with $\mathbf{Q}_1^{\text{ch}} = \mathbf{Q}_2^{\text{ch}} = (1/4, 0)$ we just obtain an additional twofold degeneracy of each of the three bands due to the equivalence of the two layers. Therefore the degeneration of the bands is fourfold since in the monolayer case each band is twofold degenerated due to the equivalence of the two sublattices (see Sec. 4). The lowest, acoustical band has zeros at the magnetic superstructure vectors which are located at $(j/4, 0)$ and $(j/4 + 1/8, 1/2)$, $j = 0, \dots, 3$, within the Brillouin zone of the square lattice (we choose $0 \leq H, K < 1$). The spectral weight is concentrated near the lowest harmonic incommensurate wave vectors $\mathbf{Q} = (1/2 \pm 1/8, 1/2)$. With increasing energy the incommensurability decreases and the branches of the acoustic magnon band close at the antiferromagnetic wave vector $(1/2, 1/2)$ and an energy ω_π which we associate with the π -resonance. Along the $(H, 1/2)$ direction the acoustic band is gapped to the overlying optical magnon band (see upper left panels in Figs. 35 and 36). Along the orthogonal direction $(1/2, K)$, one optical band has vanishing spectral weight and

only two bands are visible (see middle-left panels in Figs. 35 and 36).

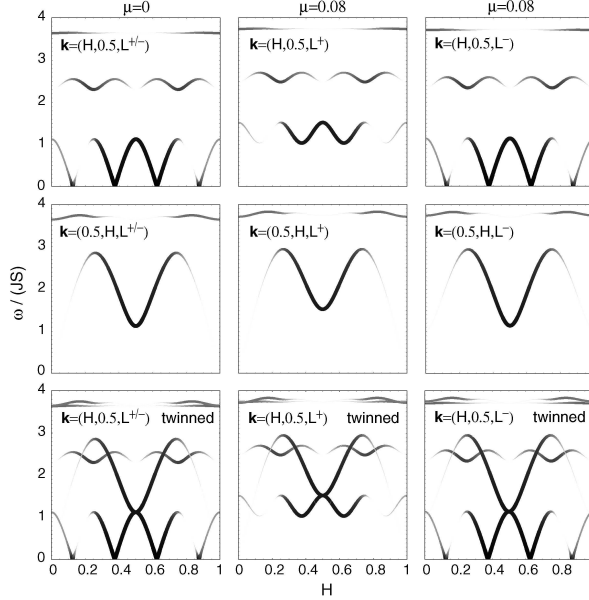


Figure 35: *Band structure and spectral weight along the $(H, 0.5, L^\pm)$ and $(0.5, H, L^\pm)$ directions for parallel stripes lying on top of each other and couplings $\lambda = 0.15$ and $\mu = 0, 0.08$. The last row shows the band structure of a twinned sample (see text). L^+ corresponds to even, L^- to odd excitations. Darker and larger points correspond to a larger weight of the inelastic structure factor.*

In twinned samples with stripe domains oriented orthogonal to each other, a scan along the $(H, 1/2)$ direction results in the superposition of the signals obtained from scans in directions $(H, 1/2)$ and $(1/2, H)$ of a single-domain sample. For domains of equal size, one thus obtains an apparent symmetry $(H, K) \leftrightarrow (K, H)$ and a fourfold pattern of the static incommensurate wave vectors located at $\mathbf{Q} = (1/2 \pm 1/8, 1/2)$ and $\mathbf{Q} = (1/2, 1/2 \pm 1/8)$ also for (shifted) parallel stripes. In Figs. 35 and 36, the panels in the third row are just obtained by superimposing the panels of the first and second row. Since the acoustic band of the monolayer system has a saddle point at the antiferromagnetic wave vector, the resulting band structure is x-shaped in the vicinity of the π -resonance energy.

The configuration of hole stripes lying perpendicular to each other corresponds to charge modulation wave vectors $\mathbf{Q}_1^{\text{ch}} = (1/4, 0)$ and $\mathbf{Q}_2^{\text{ch}} = (0, 1/4)$.

For decoupled layers, the resulting band structure contains the bands of the monolayer system and the same bands rotated by 90 degrees leading to the symmetry $\omega(H, K) = \omega(K, H)$ and therefore to a fourfold pattern of the static incommensurate wave vectors located at $\mathbf{Q} = (1/2 \pm 1/8, 1/2)$ and $\mathbf{Q} = (1/2, 1/2 \pm 1/8)$. Thus, for $\mu = 0$, the structure factor is identical for perpendicular stripes and twinned parallel stripes (left lower panel in Figs. 35 and 36).

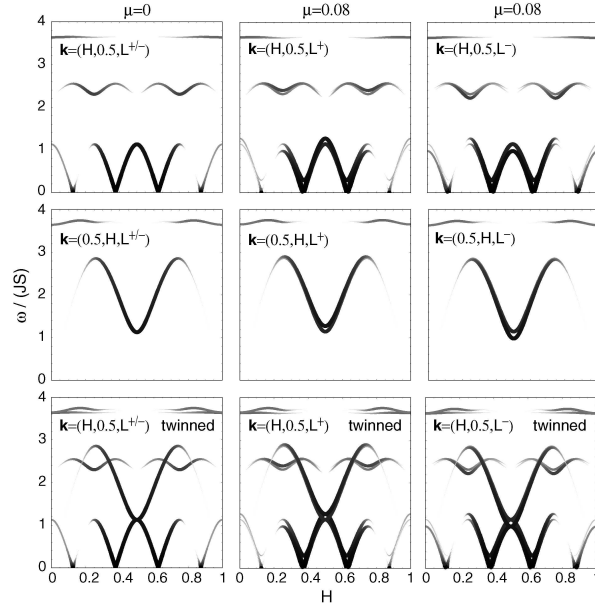


Figure 36: *Band structure and spectral weight along the $(H, 0.5, L^{\pm})$ and $(0.5, H, L^{\pm})$ directions for shifted parallel stripes and couplings $\lambda = 0.15$ and $\mu = 0, 0.08$. The last row shows the resulting band structure of a twinned sample.*

With increasing interlayer coupling μ the bands start to split with different distributions of the spectral weights in the odd and even channel (cf. Figs. 35, 36, and 37). For parallel and shifted parallel stripes the Hamiltonian is invariant under the reflection $z \rightarrow -z$ combined with a translation. This implies that the magnon states – modulo a phase factor which does not enter the structure factor – have a well defined parity with respect to an exchange of both layers. As a consequence, non-degenerate bands are visible only either in the even or the odd channel.

Nevertheless the excitation spectra of the two parallel stripe configurations deviate significantly, e.g. the even excitations are gapped for parallel stripes whereas for shifted parallel stripes the intensity of even excitations is only reduced at low energies (cf. middle columns of Figs. 35, 36). For stripes on top of each other each band – which is fourfold degenerate at $\mu = 0$ – splits up into twofold degenerate bands which have identical parity. For shifted stripes each band splits up into three bands. One of them is twofold degenerate and both subbands are of opposite parity. Therefore this degenerate band is visible in both channels (cf. Fig. 36).

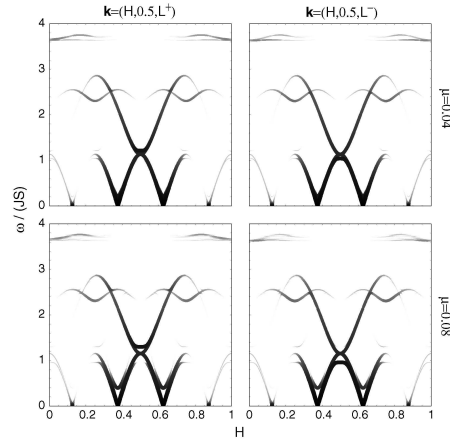


Figure 37: *Band structure and spectral weight for even (left panel) and odd (right panel) excitations along $(H, 0.5, L^\pm)$ direction for perpendicular stripes with couplings $\lambda = 0.15$ across the stripes and interlayer couplings $\mu = 0.04$ (upper row) and $\mu = 0.08$ (lower row).*

For perpendicular stripes the symmetry is more complicated. The Hamiltonian is invariant under a reflection $z \rightarrow -z$ in combination with a 90° -rotation along the z axis. Since this rotation mixes different wave vectors, almost all eigenstates do not have a well defined parity and will be partially visible in the odd and even channel. The exception are modes at particular wave vectors such as the antiferromagnetic wave vector which are mapped onto themselves (modulo a reciprocal lattice vector). Only there the excitations can be classified due to their symmetry. Like for the shifted parallel stripes the excitations are not gapped in the even channel (cf. Fig. 37).

We now focus on the band splitting and the distribution of the spectral weights of even and odd excitations at the antiferromagnetic wave-vector

(1/2, 1/2). With increasing interlayer coupling μ , the resonance energy ω_π splits up into two different energies ω_π^- and ω_π^+ for centered-parallel stripes and into three energies ω_π^- , ω_π^0 , and ω_π^+ for the other stripe configurations as schematically illustrated in Fig. 38.

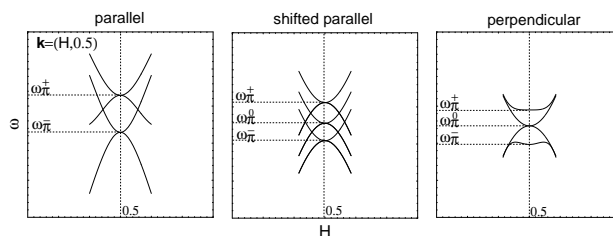


Figure 38: *Schematic illustration of the band splitting in the vicinity of the antiferromagnetic wave vector (1/2, 1/2) along the (H, 1/2) direction. In the cases of parallel stripes the band structures for twinned samples are shown. Even and odd bands are gathered together.*

It is common to all stripe configurations that ω_π^- has a finite spectral weight only in the odd channel, whereas ω_π^+ has a finite weight only in the even channel. For shifted parallel and perpendicular stripes, in both channels a finite intensity is found at the intermediate energy ω_π^0 . This intensity is however smaller than at ω_π^\pm .

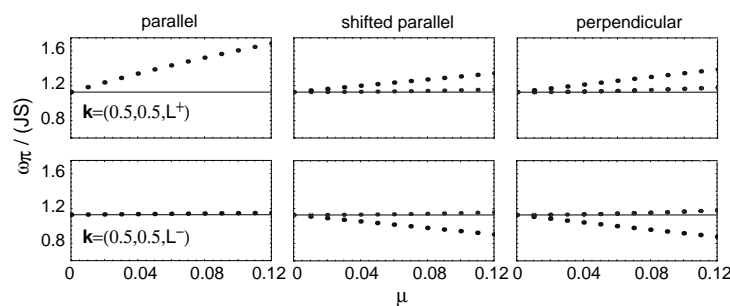


Figure 39: *Splitting of the resonance energy as a function of the interlayer coupling μ for $\lambda = 0.15$. In the odd channel ($L = L^-$) the spectral weight is concentrated at ω_π^- and no intensity is found at ω_π^+ , in the even channel ($L = L^+$) no excitations at ω_π^- are observable and the spectral weight is concentrated at ω_π^+ . For shifted and perpendicular stripes in both channels a small intensity is found at the intermediate energy ω_π^0 .*

The splitting of the resonance energy for shifted parallel and perpendicular stripes looks quite similar. ω_{π}^{-} and ω_{π}^{+} are almost equidistant to the intermediate energy ω_{π}^0 which increases only slightly with μ (cf. Fig. 39). For small couplings the splitting is quadratic in μ . For centered-parallel stripes the splitting looks different, ω_{π}^{+} increases almost linearly with μ whereas ω_{π}^{-} is almost independent of the interlayer coupling.

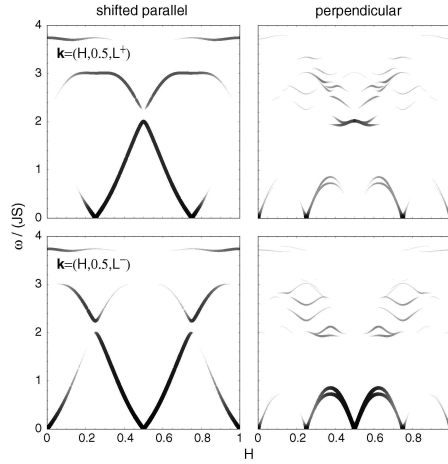


Figure 40: Band structure in the collinear regime $\mu > \mu_c(\lambda)$ along the direction $(H, 1/2, L^{\pm})$ for shifted parallel and perpendicular stripes with $\lambda = 0.07$ and $\mu = 0.50$.

Finally, we calculate the band structures for shifted parallel and perpendicular stripes for couplings $\lambda < \lambda_c$ and $\mu > \mu_c(\lambda)$ where the ground-states are collinear and the charge stripes lose their anti-phase domain boundary character. We implicitly assume that μ is not too large, otherwise spins on top of each other dimerize and lose their magnetization. In this regime the magnetic fluctuations are drastically changed. For both stripe orientations, the odd channel now has a static signal at the antiferromagnetic wave vector, whereas in the even channel the spectral weight is concentrated at incommensurate positions $(1/2 \pm 1/4, 1/2)$ (cf. Fig. 40). For perpendicular stripes we also find small intensity at these positions in the odd channel. The incommensurability is doubled compared to the regime of canted planar ground-states reflecting that the charge stripes do not act like anti-phase domain boundaries in the regime of strongly coupled layers. In the even channel the intensity at the antiferromagnetic wave-vector is peaked at an energy ω_{π}

which increases with the interlayer coupling μ and is approximately the same for both stripe configurations.

10 Discussion

In this section we compare our results to neutron scattering data for the bilayer high- T_c compound $\text{YBa}_2\text{Cu}_3\text{O}_{6+x}$. We want to stress – because of the simplifications assumed in our model – that it is not our goal to obtain a quantitative agreement. Rather we wish to draw a qualitative comparison in order to fortify the hypothesis that the stripe picture is a suitable approach to describe spin fluctuations. Furthermore, we hope that a comparison of future experimental data with our calculations will help to identify the realized stripe configuration.

Since a spin gap with an energy ω_{gap} – e.g. due to Cooper-pair formation – is not incorporated in our model, the results apply only to energies above ω_{gap} where the magnon dispersion is not masked by the superconducting condensate. In particular in the underdoped regime where ω_{gap} decreases with the doping level, the calculated spectral features become visible over an increasing energy range. Our calculations are restricted to zero temperature. Therefore, a comparison can also be made only to experiments performed at temperatures well below the superconducting transition temperature.

Experiments [71, 95, 94] in (partially) detwinned YBCO provide evidence for unidirectional order, i.e., that a fourfold pattern of incommensurate peaks near the antiferromagnetic wave vector $\mathbf{k}_{\text{AF}} = (1/2, 1/2)$ results only from the twinning. The stripes seem to be parallel and oriented along the direction of the oxygen chains in the adjacent planes. This immediately points against the scenario of perpendicular stripes for which detwinning would not affect the fourfold symmetry.

We briefly recall some neutron scattering measurements on $\text{YBa}_2\text{Cu}_3\text{O}_{6+x}$ which provide insight into the incommensurability and the π resonance over a wide doping and temperature range. For a long time it had been controversial whether both phenomena would exist above T_c until in underdoped materials the incommensurability was found also above T_c [21]. Likewise, the appearance of the magnetic resonance was found above T_c , occurring together with the pseudogap at a temperature $T^* > T_c$ determined from transport and nuclear resonance [22]. Although the π -resonance persists as a well defined feature also in the normal state above T_c , its intensity can be reduced significantly at T_c [94]. For near optimally doped compounds, the resonance is not detectable in the normal phase [12] since T^* almost coincides with T_c . Dai *et al.* [23] concluded that the resonance exists above T_c for $x \leq 0.8$ and that incommensurate spin fluctuations appear in the normal

state for $x \leq 0.6$. Arai *et al.* [2] also observed incommensurate fluctuations in the normal state for a sample with an oxygen concentration of $x = 0.7$. Thus, superconductivity is not a prerequisite for incommensurability and the π -resonance in bilayer compounds as well as in monolayer compounds.

For underdoped YBCO with various oxygen concentrations, the experimentally observed spin dynamics data (see Table 5) qualitatively look very similar. There is a systematic increase of the incommensurability and of the π resonance frequency with doping, which is consistent with our model (see Sec. 4. The bilayer stripe model shares this feature and therefore here we focus exclusively on specific bilayer features.

x	0.35	0.45	0.5	0.5	0.6	0.7	0.7	0.7
T_c (K)	39	48	52	59	63	67	67	74
δ (r.l.u.)	1/16	n/a	n/a	0.08	0.10	1/8	n/a	0.1
p	8	n/a	n/a	6.25	5	4	n/a	5
ω_π^- (meV)	23	30.5	31.5	33	34	36	33	37
ω_π^+ (meV)	n/a	n/a	n/a	n/a	n/a	41	50	n/a
Ref.	[70]	[23]	[23]	[94]	[23]	[2]	[31]	[23]

Table 5: *Spin dynamics data for $YBa_2Cu_3O_{6+x}$ for various oxygen concentrations x characterized by the critical temperature T_c , incommensurability δ , corresponding stripe period p , the resonance energy ω_π^- observed in the odd channel, and ω_π^+ . n/a stands for not available.*

Experimentally, constant energy scans slightly above the gap in the odd channel along $(H, 1/2, L^-)$ show a broad intensity peak at \mathbf{k}_{AF} , before incommensurate scattering sets in and the data can be compared to our model. The intensity shows magnetic peaks at a distance $\delta k(\omega)$ away from \mathbf{k}_{AF} . The incommensurability δ is determined by extrapolating $\delta k(\omega)$ to $\omega = 0$ and it is connected to the stripe spacing p through $\delta = 1/(2p)$. The incommensurate peaks are best defined if the stripe spacing is nearly a multiple of the lattice spacing (integer p) since the stripes are stabilized by the lattice [70].

The three stripe configurations examined for our model are not equivalent in their low-energy behavior. For (unshifted) parallel stripes (see Fig. 35), an incommensurability is visible at low energies only in the odd channel since the even channel has a relatively large gap not related to superconductivity. In contrast, for shifted parallel and perpendicular stripes the even channel shows

incommensurate response down to the superconducting gap. Experimental evidence [10, 22, 31] for a large gap in the even channel (well above the resonance energy in odd channel) therefore favors the configuration with unshifted parallel stripes.

With increasing energy, the separation $\delta k(\omega)$ of the incommensurate peaks decreases and the branches close at \mathbf{k}_{AF} at certain energies ω_π . Depending on the stripe configuration, there are two or three such energies, compare Fig. 38. According to our model, an energy scan of the odd channel at \mathbf{k}_{AF} would show a first resonance at the intersection with the lowest magnon band at ω_π^- which we identify with the resonance frequency [88, 87]. For shifted parallel and perpendicular stripes, a second line at ω_π^0 contributes to the odd channel. It has significantly less weight and is separated from the first one by only a small energy splitting (of the order of a few meV) which would be hard to be resolved experimentally.

In a similar way, the even channel has a resonance at an energy $\omega_\pi^+ > \omega_\pi^-$, and for shifted parallel and perpendicular stripes also a weaker resonance at an intermediate frequency ω_π^0 (cf. Fig. 38). Experimentally [87, 74, 94], a strong oscillatory dependence of the scattering intensity on L shows that the resonance frequencies in the odd and even channel are well separated. Energy scans at the antiferromagnetic wave vector show peaks at ω_π^- in the odd channel and ω_π^+ in the even channel, no peak at the intermediate energy ω_π^0 which should be visible in both channels is resolved [31]. This again favors unshifted parallel stripes, which (in contrast to shifted parallel and perpendicular stripes) have no shared resonance frequency ω_π^0 . Although we restricted our comparison to experiments on underdoped samples, overdoped compounds also show two distinct resonance modes of opposite symmetry [81], which could be identified with ω_π^- and ω_π^+ .

From a comparison of the band splitting $\Delta\omega_\pi = \omega_\pi^+ - \omega_\pi^-$ to experimental values (cf. Tab. 5) we can estimate the strength of the interlayer coupling μ . For $\lambda = 0.15$ we find $\mu \approx 0.02 - 0.06$ almost independent of the stripe configuration. This value is reasonable since the effective coupling μ in the stripe system should be slightly reduced compared to the undoped case where a value of $\mu \approx 0.08$ is reported [85].

Above ω_π the response is found to become incommensurate again with increasing separation $\delta k(\omega)$. The momentum width is larger and the intensity is weaker than below ω_π . Overall, the dispersion is “x-shaped”. As pointed out in Sec. 9 such a shape appears basically for every non-unidirectional stripe configuration, for parallel stripes in twinned crystals as well as in

perpendicular stripes. The x-shape has been observed explicitly in Refs. [10, 2, 31, 70]. It would be interesting to verify in detwinned samples that the relative intensities of the upper and lower branches of the x-shape are related to the population ratio of the twin domains.

In conclusion, we have calculated the bilayer effects in the magnetic excitation spectrum in striped states. As a generic feature of the stripe model we find an x-shaped dispersion in the vicinity of the π -resonance, which is consistent with experimental data. We have obtained a bilayer splitting of single-layer bands into two or three bilayer bands. From the three stripe configurations studied, the unshifted parallel case overall is most consistent with neutron scattering data, although it seems to be energetically unfavorable at first sight.

Part IV

Appendix

A Correlation functions \mathcal{C}_ρ , \mathcal{C}_σ , and \mathcal{C}_\parallel

In this appendix we calculate the correlation functions \mathcal{C}_ρ , \mathcal{C}_σ , and \mathcal{C}_\parallel introduced in section 2.3. Starting from the the Hamiltonian H_{wave} (9) quadratic in the fields ϕ and u the propagators are given by

$$\langle \phi(\mathbf{k})\phi(\mathbf{k}') \rangle = \frac{K_s^{-1}}{\mathbf{k}^2} \delta(\mathbf{k} + \mathbf{k}'), \quad (76a)$$

$$\langle u(\mathbf{k})u(\mathbf{k}') \rangle = \frac{K_c^{-1}}{\mathbf{k}^2} \left(\frac{d}{2\pi} \right)^2 \delta(\mathbf{k} + \mathbf{k}'). \quad (76b)$$

We proceed to show that

$$\langle e^{i[\phi(\mathbf{r})-\phi(\mathbf{0})]} \rangle \stackrel{|\mathbf{r}| \rightarrow \infty}{\sim} |\mathbf{r}|^{-1/(2\pi K_s)}, \quad (77a)$$

$$\langle e^{i\frac{2\pi}{d}[u(\mathbf{r})-u(\mathbf{0})]} \rangle \stackrel{|\mathbf{r}| \rightarrow \infty}{\sim} |\mathbf{r}|^{-1/(2\pi K_c)}. \quad (77b)$$

Since the calculation of both averages processes in the same manner, we only derive the first equation,

$$\langle e^{i[\phi(\mathbf{r})-\phi(\mathbf{0})]} \rangle = e^{-\frac{1}{2}\langle [\phi(\mathbf{r})-\phi(\mathbf{0})]^2 \rangle}, \quad (78a)$$

$$\begin{aligned} \frac{1}{2}\langle [\phi(\mathbf{r})-\phi(\mathbf{0})]^2 \rangle &= \frac{1}{K_s} \int_{\mathbf{k}}^{|k| \leq \Lambda} \frac{1 - e^{i\mathbf{k}\mathbf{r}}}{\mathbf{k}^2} \\ &= \frac{1}{2\pi K_s} \int_{k \leq \Lambda} \frac{1 - J_0(k|\mathbf{r}|)}{k} \\ &\stackrel{|\mathbf{r}| \rightarrow \infty}{\sim} \frac{1}{2\pi K_s} \ln(\Lambda|\mathbf{r}|). \end{aligned} \quad (78b)$$

Using Eqs. (77) it is straightforward to calculate the asymptotic behavior of the correlation functions,

$$\begin{aligned}
\mathcal{C}_\rho(\mathbf{r}) &= \langle \delta\rho(\mathbf{r})\delta\rho(\mathbf{0}) \rangle \\
&\approx \cos(\mathbf{q}\mathbf{r}) \langle e^{i\frac{2\pi}{d}[u(\mathbf{r})-u(\mathbf{0})]} \rangle \\
&\sim \cos(\mathbf{q}\mathbf{r}) |\mathbf{r}|^{-1/(2\pi K_c)}, \tag{79a}
\end{aligned}$$

$$\begin{aligned}
\mathcal{C}_\sigma(\mathbf{r}) &= \langle \vec{\sigma}(\mathbf{r}) \cdot \vec{\sigma}(\mathbf{0}) \rangle \\
&= \text{Re} \langle e^{i[\Phi(\mathbf{r})-\Phi(0)]} \rangle \\
&\approx \cos\left[\left(\mathbf{Q} + \frac{\mathbf{q}}{2}\right)\mathbf{r}\right] \langle e^{i\frac{2\pi}{d}[u(\mathbf{r})-u(\mathbf{0})]} \rangle \langle e^{i[\phi(\mathbf{r})-\phi(0)]} \rangle \\
&\sim \cos\left[\left(\mathbf{Q} + \frac{\mathbf{q}}{2}\right)\mathbf{r}\right] |\mathbf{r}|^{-1/(8\pi K_c)} |\mathbf{r}|^{-1/(2\pi K_s)}, \tag{79b}
\end{aligned}$$

$$\begin{aligned}
\mathcal{C}_\parallel(\mathbf{r}) &= 2\langle (\vec{\sigma}(\mathbf{r}) \cdot \vec{\sigma}(\mathbf{0}))^2 \rangle - 1 \\
&= \text{Re} \langle e^{2i[\Phi(\mathbf{r})-\Phi(0)]} \rangle \\
&= \cos(2\mathbf{Q}\mathbf{r}) \langle e^{i[\theta(\mathbf{r})-\theta(0)]} \rangle \langle e^{2i[\phi(\mathbf{r})-\phi(0)]} \rangle \\
&\stackrel{\Delta\theta \in 2\pi\mathbb{Z}}{=} \cos(2\mathbf{Q}\mathbf{r}) \langle e^{2i[\phi(\mathbf{r})-\phi(0)]} \rangle \\
&\sim \cos(2\mathbf{Q}\mathbf{r}) |\mathbf{r}|^{-2/(\pi K_s)}. \tag{79c}
\end{aligned}$$

B Renormalization of vector-Coulomb gases

In this appendix we explicitly renormalize the vector Coulomb gas (24) capturing the interaction of the topological defects of the stripe system and derive the flow equations (27). To be more general, we consider a vector Coulomb gas of topological charges $\mathbf{m}_i = (m_i^1, \dots, m_i^n)$ with bare fugacities $y[\mathbf{m}_i]$ located at positions $\mathbf{r}_i \in \mathbb{R}^2$,

$$\frac{H}{T} = -\pi \sum_{i \neq j} K_{\alpha\beta} m_i^\alpha \ln \left(\frac{|\mathbf{r}_i - \mathbf{r}_j|}{a_0} \right) m_j^\beta - \sum_i \ln y[\mathbf{m}_i], \quad (80)$$

where $K_{\alpha\beta} = J_{\alpha\beta}/T$ and a_0 denotes the hard-core cutoff the charges are assigned with. For the summation over the charge components α we use Einstein's sum convention. In our model we have $n = 2$ and a diagonal stiffness matrix $K_{\alpha\beta}$. The vector-Coulomb-gas Hamiltonian is identical to that of a replicated random phase-shift xy-model and we follow the coarse-graining procedure used in Refs. [13, 15]. The partition function reads

$$\mathcal{Z} = \sum_{N \geq 2} \mathcal{Z}_N = \sum_{N \geq 2} \sum_{\{\mathbf{m}_1, \dots, \mathbf{m}_N\}}^* \prod_{i=1}^N \int_{\text{h.c.}} \frac{d^2 \mathbf{r}_i}{a_0^2} y[\mathbf{m}_i] e^{\mathcal{A}_{a_0}[\mathbf{m}_1, \dots, \mathbf{m}_N]}, \quad (81)$$

$$\mathcal{A}_{a_0}[\mathbf{m}_1, \dots, \mathbf{m}_N] = \sum_{i \neq j} \pi K_{\alpha\beta} m_i^\alpha \ln \left(\frac{|\mathbf{r}_i - \mathbf{r}_j|}{a_0} \right) m_j^\beta. \quad (82)$$

The asterisk denotes the constraint of charge neutrality, $\sum_i \mathbf{m}_i = \mathbf{0}$, and the abbreviation h.c. stands for the hard-core constraints $|\mathbf{r}_i - \mathbf{r}_j| \geq a_0$ for all pairs i, j . Following the renormalization procedure developed for the scalar Coulomb gas [55, 53] we coarse grain the partition function to obtain scale dependent parameters $K_{\alpha\beta}$ and $y[\mathbf{m}]$. The functional form of the partition is preserved under an infinitesimal coarse graining, $a_0 \rightarrow \tilde{a}_0 = a_0 e^{dl}$ ($dl \ll 1$). As in the scalar case we obtain contributions to the coarse grained partition function resulting from the *rescaling* and the *annihilation* of charges with opposite sign at a scale a_0 . In addition to these contributions, in the case of vector charges we have to consider the *fusion* of charges at a scale a_0 . Two charges \mathbf{m}_i and \mathbf{m}_j with $\mathbf{m} := \mathbf{m}_i + \mathbf{m}_j \neq \mathbf{0}$ at positions \mathbf{r}_i and \mathbf{r}_j with $a_0 \leq |\mathbf{r}_i - \mathbf{r}_j| \leq \tilde{a}_0$ are replaced by a single vector charge \mathbf{m} at position $\mathbf{R} = (\mathbf{r}_i + \mathbf{r}_j)/2$. Starting from contributions with N vector charges captured by \mathcal{Z}_N , fusion leads to contributions to \mathcal{Z}_{N-1} , annihilation to contributions

to \mathcal{Z}_{N-2} , and rescaling to trivial contributions to \mathcal{Z}_N of the coarse grained partition function.

B.1 Rescaling

Under the increase of the cutoff the action transforms as follows,

$$\begin{aligned}
\mathcal{A}_{a_0}[\mathbf{m}_1, \dots, \mathbf{m}_N] &= \sum_{i \neq j} \pi K_{\alpha\beta} m_i^\alpha \ln \left(\frac{|\mathbf{r}_i - \mathbf{r}_j|}{a_0} \right) m_j^\beta \\
&= \sum_{i \neq j} \pi K_{\alpha\beta} m_i^\alpha \ln \left(\frac{|\mathbf{r}_i - \mathbf{r}_j|}{\tilde{a}_0} \right) m_j^\beta + dl \pi K_{\alpha\beta} \sum_{i \neq j} m_i^\alpha m_j^\beta \\
&= \mathcal{A}_{\tilde{a}_0}[\mathbf{m}_1, \dots, \mathbf{m}_N] - dl \pi K_{\alpha\beta} \sum_i m_i^\alpha m_i^\beta, \tag{83}
\end{aligned}$$

where we made use of the charge neutrality $\sum_i \mathbf{m}_i = \mathbf{0}$. Using this expression we obtain

$$\prod_{i=1}^N \int \frac{d^2 \mathbf{r}_i}{a_0^2} y[\mathbf{m}_i] e^{\mathcal{A}_{a_0}[\mathbf{m}_1, \dots, \mathbf{m}_N]} = \prod_{i=1}^N \int \frac{d^2 \mathbf{r}_i}{\tilde{a}_0^2} y[\mathbf{m}_i] e^{dl(2 - \pi K_{\alpha\beta} m_i^\alpha m_i^\beta)} e^{\mathcal{A}_{\tilde{a}_0}[\mathbf{m}_1, \dots, \mathbf{m}_N]}. \tag{84}$$

The extra factor resulting from the rescaling can be absorbed by the change of fugacities corresponding to the equation

$$\frac{dy[\mathbf{m}]}{dl} = (2 - \pi K_{\alpha\beta} m^\alpha m^\beta) y[\mathbf{m}]. \tag{85}$$

B.2 Annihilation and fusion

We split the partition function into two parts, $\mathcal{Z} = \tilde{\mathcal{Z}} + \mathcal{Z}_{pq}$ where \mathcal{Z}_{pq} involves configurations where one pair of charges \mathbf{m}_p and \mathbf{m}_q has a distance smaller than the increased cutoff $\tilde{a}_0 = a_0 e^{dl}$ while $\tilde{\mathcal{Z}}$ doesn't. To order dl we only have to consider configuration where one pair of charges has a distance smaller than the increased cutoff \tilde{a}_0 . We also neglect contributions of order dl where more than two charges recombine or annihilate each other since the Coulomb gas of topological vector charges is diluted for small T . Our calculation is valid only for small fugacities. Defining

$$\gamma_{ij} = 2\pi K_{\alpha\beta} m_i^\alpha m_j^\beta, \quad (86)$$

and denoting the annulus $a_0 \leq |\mathbf{r}_p - \mathbf{r}_q| \leq \tilde{a}_0$ with $\Delta(p, q)$ the contribution \mathcal{Z}_{pq} can be written as

$$\mathcal{Z}_{p,q} = \sum_{\{\mathbf{m}_1, \dots, \mathbf{m}_N\}}^* \prod_{i=1, \dots, N}^{i \neq p, q} \int_{\text{h.c.}} \frac{d^2 \mathbf{r}_i}{a_0^2} y[\mathbf{m}_i] \sum_{\mathbf{m}_p, \mathbf{m}_q} \int_{\Delta(p, q)} \frac{d^2 \mathbf{r}_p}{a_0^2} \frac{d^2 \mathbf{r}_q}{a_0^2} y[\mathbf{m}_p] y[\mathbf{m}_q] e^{\mathcal{A}_{pq}}, \quad (87)$$

with an exponentiated action

$$e^{\mathcal{A}_{pq}} = \left(\frac{|\mathbf{r}_p - \mathbf{r}_q|}{a_0} \right)^{\gamma_{pq}} \prod_{i \neq p, q} \left(\frac{|\mathbf{r}_i - \mathbf{r}_p|}{a_0} \right)^{\gamma_{ip}} \left(\frac{|\mathbf{r}_i - \mathbf{r}_q|}{a_0} \right)^{\gamma_{iq}} \prod_{i < j}^{i, j \neq p, q} \left(\frac{|\mathbf{r}_i - \mathbf{r}_j|}{a_0} \right)^{\gamma_{ij}} \quad (88)$$

B.2.1 Annihilation

To calculate the contribution resulting of the annihilation of two vector charges with opposite sign, $\mathbf{m}_p = -\mathbf{m}_q$ we have to integrate over \mathbf{r}_p and \mathbf{r}_q . Transforming to relative coordinates $\mathbf{r} = \mathbf{r}_p - \mathbf{r}_q$ and $\mathbf{R} = (\mathbf{r}_p + \mathbf{r}_q)/2$ and expanding Eq.(88) up to quadratic order in \mathbf{r} we obtain

$$\begin{aligned} \mathcal{Z}_{p,q} &= \sum_{\{\mathbf{m}_1, \dots, \mathbf{m}_N\}}^* \prod_{i=1, \dots, N}^{i \neq p, q} \int_{\text{h.c.}} \frac{d^2 \mathbf{r}_i}{a_0^2} y[\mathbf{m}_i] \prod_{i < j}^{i, j \neq p, q} \left(\frac{|\mathbf{r}_i - \mathbf{r}_j|}{a_0} \right)^{\gamma_{ij}} \sum_{\mathbf{m}_p} y^2[\mathbf{m}_p] \\ &\times \int_{a_0 \leq |\mathbf{r}| \leq \tilde{a}_0} \frac{d^2 \mathbf{r}}{a_0^2} \int \frac{d^2 \mathbf{R}}{a_0^2} \left(1 + \frac{1}{4} \sum_{i, j \neq p, q} \gamma_{ip} \gamma_{jp} \frac{\mathbf{r}(\mathbf{r}_i - \mathbf{R}) \cdot \mathbf{r}(\mathbf{r}_j - \mathbf{R})}{|\mathbf{r}_i - \mathbf{R}|^2 |\mathbf{r}_j - \mathbf{R}|^2} \right). \end{aligned} \quad (89)$$

Performing the integrals over \mathbf{r} and \mathbf{R} and reexponentiating the contribution to \mathcal{Z}_{N-2} of the coarse grained partition function reads

$$\mathcal{Z}_{p,q} \sim \sum_{\{\mathbf{m}_1, \dots, \mathbf{m}_N\}}^* \prod_{i=1, \dots, N}^{i \neq p, q} \int_{\text{h.c.}} \frac{d^2 \mathbf{r}_i}{a_0^2} y[\mathbf{m}_i] \prod_{i < j}^{i, j \neq p, q} \left(\frac{|\mathbf{r}_i - \mathbf{r}_j|}{a_0} \right)^{\gamma_{ij} - \pi^2 \text{dl} \sum_{\mathbf{m}_p} \gamma_{ip} \gamma_{jp} y^2[\mathbf{m}_p]}. \quad (90)$$

Therefore, the annihilation of charges leads to a scale dependent correction of the stiffness constants controlled by the flow equation

$$\frac{d}{dl}(\mathbf{K}^{-1})_{\alpha\beta} = 2\pi^3 \sum_{\mathbf{m}} m^\alpha m^\beta y^2[\mathbf{m}] \quad (91)$$

B.2.2 Fusion

In this case a pair of charges with $\mathbf{m} =: \mathbf{m}_p + \mathbf{m}_q \neq \mathbf{0}$ with distance $a_0 \leq |\mathbf{r}_p - \mathbf{r}_q| \leq \tilde{a}_0$ has to be replaced by an effective charge \mathbf{m} located at $\mathbf{R} = (\mathbf{r}_p + \mathbf{r}_q)/2$. Therefore, we have to integrate Eq.(87) over the relative position $\mathbf{r} = \mathbf{r}_p - \mathbf{r}_q$ of the two charges. To calculate the contributions of order dl to \mathcal{Z}_{N-1} it is enough to expand Eq.(88) to order 0 in \mathbf{r} . The contribution to the coarse grained partition function resulting from fusion then reads

$$\begin{aligned} \mathcal{Z}_{p,q} \sim & \sum_{\{\mathbf{m}_1, \dots, \mathbf{m}_N\}}^* \prod_{i=1, \dots, N}^{i \neq p, q} \int_{\text{h.c.}} \frac{d^2 \mathbf{r}_i}{a_0^2} y[\mathbf{m}_i] \sum_{\mathbf{m}_p, \mathbf{m}_q} \int \frac{d^2 \mathbf{R}}{a_0^2} 2\pi y[\mathbf{m}_p] y[\mathbf{m}_q] \\ & \times \prod_{i \neq p, q} \left(\frac{|\mathbf{r}_i - \mathbf{R}|}{a_0} \right)^{\gamma_{ip} + \gamma_{iq}} \prod_{i < j}^{i, j \neq p, q} \left(\frac{|\mathbf{r}_i - \mathbf{r}_j|}{a_0} \right)^{\gamma_{ij}}. \end{aligned} \quad (92)$$

Since $\gamma_{ip} + \gamma_{iq} = \gamma_{i, p+q}$ this contribution leads to a correction of the fugacity $y[\mathbf{m}_p + \mathbf{m}_q]$ of the non zero charge $\mathbf{m}_p + \mathbf{m}_q$ due to

$$\frac{d}{dl} y[\mathbf{m}_p + \mathbf{m}_q] = 2\pi \sum_{\mathbf{m}_p, \mathbf{m}_q} y[\mathbf{m}_p] y[\mathbf{m}_q]. \quad (93)$$

Putting together the corrections to the stiffness matrix $K_{\alpha\beta}$ and the fugacities $y[\mathbf{m}]$ resulting from rescaling, annihilation, and fusion, the flow equations can be written as

$$\frac{d}{dl}(\mathbf{K}^{-1})_{\alpha\beta} = 2\pi^3 \sum_{\mathbf{m}} m^\alpha m^\beta y^2[\mathbf{m}], \quad (94a)$$

$$\frac{dy[\mathbf{m}]}{dl} = (2 - \pi K_{\alpha\beta} m^\alpha m^\beta) y[\mathbf{m}] + \pi \sum_{\substack{\mathbf{m}', \mathbf{m}'' \neq \mathbf{0} \\ \mathbf{m}' + \mathbf{m}'' = \mathbf{m}}} y[\mathbf{m}'] y[\mathbf{m}'']. \quad (94b)$$

To derive these equations, we have made the assumptions that the fugacities are small and the gas is diluted. Therefore, the flow equations are valid only for small temperatures.

B.3 Evaluation for the stripe system

In the following we have to specify the flow equations (94) to the case of the two component vector gas describing the interaction of the topological charges in the stripe system. We have to sum over 8 different vector charges $\mathbf{m} = (m_s, m_c)$: vortices $(\pm 1, 0)$, loops $(0, \pm 2)$, and dislocations $(\pm 1/2, \pm 1)$. We denote the fugacities of these charges with y_v , y_l and y_d . Since the stiffness matrix is given by the diagonal matrix

$$\mathbf{K} = \begin{pmatrix} K_s & 0 \\ 0 & K_c \end{pmatrix}, \quad (95)$$

we can directly decompose Eq.(94a) to flow equations for K_s^{-1} and K_c^{-1} ,

$$\frac{dK_s^{-1}}{dl} = 2\pi^3 \sum_{\mathbf{m}} m_s^2 y^2[\mathbf{m}] = 2\pi^3(2y_v^2 + y_d^2), \quad (96a)$$

$$\frac{dK_c^{-1}}{dl} = 2\pi^3 \sum_{\mathbf{m}} m_c^2 y^2[\mathbf{m}] = 8\pi^3(2y_l^2 + y_d^2). \quad (96b)$$

Flow equations for the fugacities y_v , y_l and y_d can be easily obtained from Eq.(94b), e.g.

$$\begin{aligned} \frac{dy_d}{dl} &= \frac{dy[(\frac{1}{2}, 1)]}{dl} \\ &= \left(2 - \frac{\pi}{4}(K_s + 4K_c)\right) y_d + \pi \sum_{\substack{\mathbf{m}', \mathbf{m}'' \neq \mathbf{0} \\ \mathbf{m}' + \mathbf{m}'' = (\frac{1}{2}, 1)}} y[\mathbf{m}'] y[\mathbf{m}''] \\ &= \left(2 - \frac{\pi}{4}(K_s + 4K_c)\right) y_d + 2\pi \left(y[(1, 0)] y[(\frac{1}{2}, 1)] + y[(0, 2)] y[(\frac{1}{2}, -1)] \right) \\ &= \left(2 - \frac{\pi}{4}(K_s + 4K_c)\right) y_d + 2\pi(y_v + y_l) y_d. \end{aligned} \quad (97)$$

In the same manner we obtain

$$\frac{dy_v}{dl} = (2 - \pi K_s)y_v + 2\pi y_d^2, \quad (98)$$

$$\frac{dy_l}{dl} = (2 - 4\pi K_c)y_l + 2\pi y_d^2. \quad (99)$$

C Correlation length in the disordered phase

In the following we calculate the correlation length in the disordered phase sufficiently close to the ordered phase ($T > T_c$ and $(T - T_c)/T_c \ll 1$) for the KT transitions as well as close to the triple points of the vector-Coulomb gas. The corresponding trajectories are therefore very close to the separatrix. At the triple points the set of flow equations (27) reduces to

$$\frac{dX}{dl} = Y^2, \quad (100a)$$

$$\frac{dY}{dl} = XY + 2\alpha Y^2, \quad (100b)$$

with $\alpha = 1/(2\sqrt{6})$. For the KT equations we introduce $X := 2 - \pi K$ and $Y := 4\pi y$ and obtain, up to quadratic order in these small variables, the same equations with $\alpha = 0$. We proceed to integrate the flow equations (100) for an arbitrary $\alpha > 0$ close to the ordered phase following the analysis of Young [114].

The separatrix terminating at the repulsive fixed point $X^* = Y^* = 0$ is given by the straight lines $Y = m_+ X$ for $X > 0$ and $Y = m_- X$ for $X < 0$ where the slopes are solutions of the quadratic equation $m^2 - 2\alpha m - 1 = 0$,

$$m_{\pm} = \alpha \pm \sqrt{\alpha^2 + 1}. \quad (101)$$

For $T > T_c$ the fugacity Y decreases with l down to a value $Y_{\min} = Y(l_{\min})$ and then starts to increase with the scale. The correlation length $\xi \sim e^{l^*}$ is determined by the scale where y reaches a value of order unity. If we are very close to the ordered phase ($T - T_c \ll 1$) the trajectory is very close to the separatrix and $l^* \approx 2l_{\min}$. From the flow equations we recognize that $Y_{\min} = X(l_{\min})/(2\alpha)$. For $l < l^*$ we make an ansatz

$$Y(l) = m_- X(l) + \Delta(l). \quad (102)$$

The function Δ giving the deviation from the separatrix is determined by the differential equation

$$\frac{d\Delta}{dl} = -X\Delta + \mathcal{O}(\Delta^2), \quad (103)$$

leading to

$$\begin{aligned}\Delta(l) &= \Delta_0 \exp\left(-\int_0^l X(l') dl'\right) \\ &\approx \Delta_0 (1 - X_0 m_-^2 l)^{1/m_-^2},\end{aligned}\quad (104)$$

where we have inserted the flow $X(l) = (X_0^{-1} - m_-^2 l)^{-1}$ on the separatrix which is correct in lowest order of Δ . The initial value $\Delta_0 = \Delta(0)$ of the deviation function is proportional to $(K_c - K)$. Using the condition of the minimum of $Y(l)$,

$$Y_{\min} = m_- X(l_{\min}) + \Delta(l_{\min}) = \frac{1}{2\alpha} X(l_{\min}), \quad (105)$$

we obtain

$$l^* \approx 2l_{\min} \sim \Delta_0^{-\frac{m_-^2}{m_-^2+1}}, \quad (106)$$

and therefore for the correlation length

$$\xi \sim \exp(b(T - T_c)^{-\nu}), \quad (107)$$

with a critical exponent

$$\nu = \frac{m_-^2}{m_-^2 + 1} = 1 - \frac{1}{2} \left(\alpha^2 - \alpha \sqrt{\alpha^2 + 1} + 1 \right)^{-1}. \quad (108)$$

For the KT-transition ($\alpha = 0$) this results in a critical exponent $\nu = \frac{1}{2}$.

References

- [1] M. Arai, T. Arakawa, M. Fujita, S. Wakimoto, K. Yamada, Y. Endoh, G. Aeppli, T. E. Mason, and S. M. Hayden. *Czech. J. Phys. Suppl.*, 46:1147, 1996.
 - [2] M. Arai, T. Nishijima, Y. Endoh, T. Egami, S. Tajima, K. Tomimoto, Y. Shiohara, M. Takahashi, A. Garret, and S. M. Bennington. *Phys. Rev. Lett.*, 83:608, 1999.
 - [3] C. D. Batista, G. Ortiz, and A. V. Balatsky. *Phys. Rev. B*, 64:172508, 2001.
 - [4] J. G. Bednorz and K. A. Müller. *Z. Phys. B*, 64:189, 1986.
 - [5] V. L. Berezinski. *Sov. Phys. JETP*, 32:493, 1971.
 - [6] V. L. Berezinski. *Sov. Phys. JETP*, 34:610, 1972.
 - [7] G. Blumberg, M. V. Klein, and S.-W. Cheong. *Phys. Rev. Lett.*, 80:564, 1998.
 - [8] S. Bogner and S. Scheidl. *Phys. Rev. B*, 64:054517, 2001.
 - [9] P. Bourges. In J. Bok, G. Deutscher, D. Pavuna, and S. A. Wolf, editors, *The gap Symmetry and Fluctuations in High-Temperature Superconductors*. Plenum Press, 1998. condmat/9901333.
 - [10] P. Bourges, H. F. Fong, L. P. Regnault, J. Bossy, C. Vettier, D. L. Milius, I. A. Aksay, and B. Keimer. *Phys. Rev. B*, 56:R11439, 1997.
 - [11] P. Bourges, Y. Sidis, M. Braden, K. Nakajima, and J. Tranquada. *Phys. Rev. Lett.*, 90:147202, 2003.
 - [12] P. Bourges, Y. Sidis, H. F. Fong, L. P. Regnault, J. Bossy, A. Ivanov, and B. Keimer. *Science*, 288:1234, 2000.
 - [13] J. L. Cardy and S. Ostlund. *Phys. Rev. B*, 25:6899, 1982.
 - [14] E. W. Carlson, D. X. Yao, and D. K. Campbell. condmat/0402231.
 - [15] D. Carpentier and P. Le Doussal. *Nucl. Phys. B*, 588:565, 2000.
-

-
- [16] S. Chakravarty. *Eur. Phys. J. B*, 5:337, 1998.
- [17] L. Chayes, V. J. Emery, S. A. Kivelson, Z. Nussinov, and J. Tarjus. *Physica A*, 115:129, 1996.
- [18] C. H. Chen, S.-W. Cheong, and A. S. Cooper. *Phys. Rev. Lett.*, 71:2461, 1993.
- [19] S.-W. Cheong, G. Aeppli, T. E. Mason, H. Mook, S. M. Hayden, P. C. Canfield, Z. Fisk, K. N. Clausen, and J. L. Martinez. *Phys. Rev. Lett.*, 67:1791, 1991.
- [20] S.-W. Cheong, H. Y. Hwang, C. H. Chen, B. Batlogg, L. W. Rupp, Jr, and S. A. Carter. *Phys. Rev. B*, 49:7088, 1994.
- [21] P. Dai, H. A. Mook, and F. Dogan. *Phys. Rev. Lett.*, 80:1738, 1998.
- [22] P. Dai, H. A. Mook, S. M. Hayden, G. Aeppli, T. G. Perring, R. D. Hunt, and F. Dogan. *Science*, 284:1344, 1999.
- [23] P. Dai, H. A. Mook, R. D. Hunt, and F. Dogan. *Phys. Rev. B*, 63:054525, 1999.
- [24] P. Dai, M. Yethiraj, H. A. Mook, T. B. Lindemer, and F. Dogan. *Phys. Rev. Lett.*, 77:5425, 1996.
- [25] E. Demler and S.-C. Zhang. *Phys. Rev. Lett.*, 75:4126, 1995.
- [26] C.-H. Du, M. E. Ghazi, Y. Su, I. Pape, P. D. Hatton, S. D. Brown, W. G. Stirling, M. J. Cooper, and S.-W. Cheong. *Phys. Rev. Lett.*, 84:3911, 2000.
- [27] V. J. Emery. *Phys. Rev. Lett.*, 58:2794, 1987.
- [28] V. J. Emery, S. A. Kivelson, and H.-Q. Lin. *Phys. Rev. Lett.*, 64:475, 1990.
- [29] V. J. Emery, S. A. Kivelson, and J. M. Tranquada. *Proc. Natl. Acad. Sci. USA*, 96:8814, 1999.
- [30] H. Eskes and J. H. Jefferson. *Phys. Rev. B*, 9788:48, 1993.
-

-
- [31] H. F. Fong, P. Bourges, Y. Sidis, L. P. Regnault, J. Bossy, A. Ivanov, D. L. Milius, I. A. Aksay, and B. Keimer. *Phys. Rev. B*, 61:14773, 2000.
- [32] H. F. Fong, P. Bourges, Y. Sidis, L. P. Regnault, A. Ivanov, G. D. Guk, N. Koshizuka, and B. Keimer. *Nature (London)*, 398:588, 1999.
- [33] H. F. Fong, B. Keimer, P. W. Anderson, D. Reznik, F. Dogan, and I. A. Aksay. *Phys. Rev. Lett.*, 75:316, 1995.
- [34] H. F. Fong, B. Keimer, D. L. Milius, and I. A. Aksay. *Phys. Rev. Lett.*, 78:713, 1997.
- [35] M. Grüninger. *Of spin and charge in the cuprates*. PrintPartners Ipskamp B.V., Enschede, The Netherlands, 1999.
- [36] B. I. Halperin and D. R. Nelson. *Phys. Rev. Lett.*, 41:121, 1978.
- [37] S. M. Hayden, G. Aeppli, H. A. Mook, S.-W. Cheong, and Z. Fisk. *Phys. Rev. B*, 42:10220, 1990.
- [38] S. M. Hayden, G. H. Lander, J. Zarestky, P. J. Brown, C. Stassis, P. Metcalf, and J. M. Honig. *Phys. Rev. Lett.*, 68:1061, 1992.
- [39] R. M. Hazen. *Physical Properties of High Temperature Superconductors II*. edited by D. M. Ginsberg, World Scientific, Singapore, 1990.
- [40] H. He, P. Bourges, G. D. Gu, A. Ivanov, N. Koshizuka, B. Liang, C. T. Lin, L. P. Regnault, E. Schoenherr, and B. Keimer. *Phys. Rev. Lett.*, 86:1610, 2001.
- [41] H. He, P. Bourges, Y. Sidis, C. Ulrich, L. P. Regnault, S. Pailhes, N. S. Berzigiarova, N. N. Kolesnikov, and B. Keimer. *Science*, 295:1045, 2002.
- [42] J. E. Hoffman, E. W. Hudson, K. M. Lang, V. Madhavan, E. Eisaki, S. Uchida, and J. C. Davis. *Science*, 295:466, 2002.
- [43] C. Howald, H. Eisaki, N. Kaneko, and A. Kapitulnik. cond-mat/0201546.
- [44] M. S. Hybertsen, M. Schlüter, and N. E. Christensen. *Phys. Rev. B*, 39:9028, 1989.
-

-
- [45] N. Ichikawa, S. Uchida, J. M. Tranquada, T. Niemöller, P. M. Gehring, S. H. Lee, and J. R. Schneider. *Phys. Rev. Lett.*, 85:1738, 2000.
- [46] E. Kaneshita, M. Ichioka, and K. Machida. *J. Phys. Soc. Jap.*, 70:866, 2001.
- [47] B. Keimer, A. Aharony, A. Auerbach, R. J. Birgeneau, A. Cassanho, Y. Endoh, R. W. Erwin, M. A. Kastner, and G. Shirane. *Phys. Rev. B*, 45:7430, 1992.
- [48] B. Keimer, N. Belk, R. J. Birgeneau, A. Cassanho, C. Y. Chen, M. Greven, M. A. Kastner, A. Aharony, Y. Endoh, R. W. Erwin, and G. Shirane. *Phys. Rev. B*, 46:14034, 1992.
- [49] B. Keimer, R. J. Birgeneau, A. Cassanho, Y. Endoh, M. Greven, M. A. Kastner, and G. Shirane. *Z. Phys. B: Condens. Matter*, 91:373, 1993.
- [50] B. Keimer, P. Bourges, H. F. Fong, Y. Sidis, L. P. Regnault, A. Ivanov, D. L. Milius, I. A. Aksay, G. D. Gu, and N. Koshizuka. *J. Phys. Chem. Solids*, 60:1007, 1999.
- [51] B. Khaykovich, Y. S. Lee, R. W. Erwin, S. Lee, S. Wakimoto, K. J. Thomas, M. A. Kastner, and R. J. Birgeneau. *condmat/0112505*.
- [52] S. A. Kivelson, E. Fradkin, and V. J. Emery. *Nature (London)*, 393:550, 1998.
- [53] J. M. Kosterlitz. *Physica C*, 7:1046, 1974.
- [54] J. M. Kosterlitz and D. J. Thouless. *J. Phys. C*, 5:L124, 1972.
- [55] J. M. Kosterlitz and D. J. Thouless. *J. Phys. C*, 6:1181, 1973.
- [56] F. Krüger and S. Scheidl. *Phys. Rev. B*, 67:134512, 2003.
- [57] B. Lake, G. Aeppli, T. E. Mason, A. Schröder, F. D. McMorrow, K. Lefmann, M. Isshild, M. Nohara, H. Takagi, and S. M. Hayden. *Nature (London)*, 400:43, 2000.
- [58] C.-H. Lee, K. Yamada, Y. Endoh, G. Shirane, R. J. Birgeneau, M. A. Kastner, M. Greven, and Y.-J. Kim. *J. Phys. Soc. Jap.*, 69:1170, 2000.
-

-
- [59] S.-H. Lee and S.-W. Cheong. *Phys. Rev. Lett.*, 79:2514, 1997.
- [60] A. J. Leggett. *Phys. Rev. Lett.*, 83:392, 1999.
- [61] U. Löw, V. J. Emery, K. Fabricius, and S. A. Kivelson. *Phys. Rev. Lett.*, 72:1918, 1994.
- [62] K. B. Lyons, P. A. Fleury, J. P. Remeika, A. S. Cooper, and T. J. Negran. *Phys. Rev. B*, 37:2353, 1988.
- [63] K. Machida. *Physica C*, 158:192, 1989.
- [64] E. Manousakis. *Rev. Mod. Phys.*, 63:1, 1991.
- [65] T. E. Mason, G. Aeppli, and H. A. Mook. *Phys. Rev. Lett.*, 68:1414, 1992.
- [66] M. Matsuda, M. Fujita, K. Yamada, R. J. Birgeneau, M. A. Kastner, H. Hiraka, Y. Endoh, S. Wakimoto, and G. Shirane. *Phys. Rev. B*, 62:9148, 2000.
- [67] M. Matsumoto, C. Yasuda, S. Todo, and H. Takayama. *Phys. Rev. B*, 65:014407, 2001.
- [68] A. K. McMahan, J. F. Annett, and R. M. Martin. *Phys. Rev. B*, 42:6268, 1990.
- [69] N. D. Mermin and H. Wagner. *Phys. Rev. Lett.*, 17:1133, 1966.
- [70] H. A. Mook, O. Dai, and F. Dogan. *Phys. Rev. Lett.*, 88:097004, 2002.
- [71] H. A. Mook, P. Dai, F. Dögan, and R. S. Hunt. *Nature (London)*, 404:729, 2000.
- [72] H. A. Mook, P. Dai, S. M. Hayden, G. Aeppli, T. G. Perring, and F. Dogan. *Nature (London)*, 395:580, 1998.
- [73] H. A. Mook and F. Dögan. *Nature (London)*, 401:145, 1999.
- [74] H. A. Mook, M. Yethiraj, G. Aeppli, T. E. Mason, and T. Armstrong. *Phys. Rev. Lett.*, 70:3490, 1993.
- [75] E. Müller-Hartmann and A. Reischl. *Eur. Phys. J. B*, 28:173, 2002.
-

-
- [76] F. R. N. Nabarro. *Theory of Dislocations*. Clarendon Press, Oxford, 1967.
- [77] K. Nakajima, K. Yamada, S. Hosoya, T. Omata, and Y. Endoh. *J. Phys. Soc. Jap.*, 62:4438, 1993.
- [78] D. R. Nelson. *Phys. Rev. B*, 18:2318, 1978.
- [79] T. Niemöller, N. Ichikawa, T. Frello, H. Hünnefeld, N. H. Andersen, S. Uchida, J. R. Schneider, and J. M. Tranquada. *Eur. Phys. J. B*, 12:509, 1999.
- [80] M. Nuñez-Regueiro, J. L. Tholence, E. V. Antipov, J. J. Capponi, and M. Marezio. *Science*, 262:97, 1993.
- [81] S. Pailhes, Y. Sidis, P. Bourges, C. Ulrich, V. Hinkov, L. P. Regnault, A. Ivanov, B. Liang, C. T. Lin, and C. Bernhard. *condmat/0308394*.
- [82] S. Petit, A. H. Moudden, B. Hennion, A. Vietkin, and A. Revcolevschi. *Physica B*, 234-236:800, 1997.
- [83] D. Poilblanc and T. M. Rice. *Phys. Rev. B*, 39:9749, 1989.
- [84] C. N. R. Rao and B. Raveau. *Transition metal oxides*. VCH publishers, Inc., New York, 1995.
- [85] D. Reznik, P. Bourges, H. Fong, L. P. Regnault, J. Bossy, C. Vettier, D. L. Milius, I. A. Aksay, and B. Keimer. *Phys. Rev. B*, 53:R14741, 1996.
- [86] D. Reznik, P. Bourges, L. Pintschovius, Y. Endoh, T. Matsui, and S. Tajima. *condmat/0307591*.
- [87] J. Rossat-Mignod, L. P. Regnault, P. Bourges, P. Burlet, C. Vettier, and J. Y. Henry. *Physica B*, 192:109, 1993.
- [88] J. Rossat-Mignod, L. P. Regnault, C. Vettier, P. Bourges, P. Burlet, J. Bossy, J. Y. Henry, and G. Lapertot. *Physica C*, 185-189:86, 1991.
- [89] G. A. Samara, W. F. Hammetter, and E. L. Venturini. *Phys. Rev. B*, 41:8974, 1990.
-

-
- [90] S. Scheidl. *Physik Journal*, 2:41, 10/2003.
- [91] J. R. Schrieffer, S. C. Zhang, and X. G. Wen. *Phys. Rev. Lett.*, 60:944, 1988.
- [92] H. J. Schulz. *J. Physique*, 50:2833, 1989.
- [93] H. J. Schulz. *Phys. Rev. Lett.*, 64:1445, 1990.
- [94] C. Stock, W. J. L. Buyers, R. Liang, D. Peets, Z. Tun, D. Bonn, W. N. Hardy, and R. J. Birgeneau. *condmat/0308168*.
- [95] C. Stock, W. J. L. Buyers, Z. Tun, R. Liang, D. Peets, D. Bonn, W. N. Hardy, and L. Taillefer. *Phys. Rev. B*, 66:024505, 2000.
- [96] W. P. Su. *Phys. Rev. B*, 37:9904, 1988.
- [97] S. Sugai, M. Sato, T. Kobayashi, J. Akimitsu, T. Ito, H. Takagi, S. Uchida, S. Hosoya, T. Kajitani, and T. Fukuda. *Phys. Rev. B*, 42:1045, 1990.
- [98] T. Timusk and B. Statt. *Rep. Prog. Phys.*, 62:61, 1999.
- [99] J. M. Tranquada, J. D. Axe, N. Ichikawa, A. R. Moodebaugh, Y. Nakamura, and S. Uchida. *Phys. Rev. Lett.*, 78:338, 1997.
- [100] J. M. Tranquada, D. J. Buttrey, and V. Sachan. *Phys. Rev. B*, 54:12318, 1996.
- [101] J. M. Tranquada, D. J. Buttrey, V. Sachan, and J. E. Lorenzo. *Phys. Rev. Lett.*, 73:1003, 1994.
- [102] J. M. Tranquada, B. J. Sternlieb, J. D. Axe, Y. Nakamura, and S. Uchida. *Nature (London)*, 375:561, 1995.
- [103] J. M. Tranquada, H. Woo, T. G. Perring, H. Goka, G. D. Gu, G. Xu, M. Fujita, and K. Yamada. *condmat/0401621*.
- [104] J. Tworzydło, O. Y. Osman, C. N. A. van Duin, and J. Zaanen. *Phys. Rev. B*, 59:115, 1999.
- [105] G. S. Uhrig, K. P. Schmidt, and M. Grüninger. *condmat/0402659*.
-

-
- [106] C. M. Varma, S. Schmitt-Rink, and E. Abrahams. *Solid State Commun.*, 62:681, 1987.
- [107] M. Voijta and T. Ulbricht. *condmat/0402377*.
- [108] S. Wakimoto, G. Shirane, Y. Endoh, K. Hirota, S. Ueki, K. Yamada, R. J. Birgenau, M. A. Kastner, Y. S. Lee, P. M. Gehring, and S. H. Lee. *Phys. Rev. B*, 60:R769, 2000.
- [109] K. Yamada, M. Arai, Y. Endoh, S. Hosoya, K. Nakajima, T. Perring, and A. Taylor. *J. Phys. Soc. Jap.*, 60:1197, 1991.
- [110] K. Yamada, Y. Endoh, C. H. Lee, S. Wakimoto, M. Arai, K. Ubukata, M. Fujita, S. Hosoya, and S. M. Bennington. *J. Phys. Soc. Jap.*, 64:2742, 1995.
- [111] K. Yamada, C. H. Lee, K. Kurahashi, J. Wada, S. Wakimoto, S. Ueki, Y. Endoh, S. Hosoya, G. Shirane, R. J. Birgenau, M. Greven, M. A. Kastner, and Y. J. Kim. *Phys. Rev. B*, 57:6165, 1998.
- [112] K. Yamada, S. Wakimoto, G. Shirane, C. H. Lee, M. A. Kastner, S. Hosoya, M. Greven, Y. Endoh, and R. J. Birgenau. *Phys. Rev. Lett.*, 75:1626, 1995.
- [113] H. Yoshizawa, T. Kakeshita, R. Kajimoto, T. Tanabe, T. Katsufuji, and Y. Tokura. *Phys. Rev. B*, 61:R854, 2000.
- [114] A. P. Young. *Phys. Rev. B*, 19:1855, 1979.
- [115] J. Zaanen. *Physica C*, 317:217, 1999.
- [116] J. Zaanen and O. Gunnarsson. *Phys. Rev. B*, 40:7391, 1989.
- [117] J. Zaanen, O. Y. Osman, H. V. Krius, Z. Nussinov, and J. Tworzydło. *Phil. Mag. B*, 81:1485, 2001.
- [118] J. Zaanen and W. van Saarloos. *Physica C*, 282:178, 1997.
- [119] O. Zachar. *Phys. Rev. B*, 62:13836, 2000.
- [120] O. Zachar, S. A. Kivelson, and V. J. Emery. *Phys. Rev. B*, 57:1422, 1998.
-

Kurzzusammenfassung

Die Ausbildung von Streifenphasen in geschichteten Kuprat-Hochtemperatursupraleitern und eng verwandten Nickelaten ist generisch. Zusätzliche Ladungsträger, welche aus einer Dotierung der Materialien resultieren, kondensieren in sich spontan herausbildenden Antiphasengrenzen zwischen isolierenden antiferromagnetischen Domänen. In dieser Arbeit werden Spin- und Ladungsfluktuationen in solchen streifenartigen Überstrukturen untersucht.

Im ersten Teil der Arbeit wird das Phänomen der Spin- und Ladungsseparation in Streifenphasen untersucht. Experimentell wird Ladungsordnung oberhalb der Temperatur beobachtet, bei welcher die magnetische Ordnung einsetzt. Wir studieren das Schmelzen der Streifen, welches durch die thermische Anregung von drei Arten von topologischen Defekten getrieben wird, Ladungsversetzungen, Versetzungsschleifen und Spinwirbel. Da die Defekte in zwei Dimensionen auf großen Längenskalen logarithmisch miteinander wechselwirken, können sie als ein Coulombgas von topologischen Punktladungen aufgefasst werden. Das Phasendiagramm sowie die kritischen Eigenschaften der Phasenübergänge werden im Rahmen einer Renormierungsgruppenanalyse berechnet. Abhängig davon, welche Defektypen dissoziieren, können vier Phasen identifiziert werden. Diese sind charakterisiert durch die Reichweite der Ladungsordnung, der magnetischen Ordnung sowie der kollinearen Ordnung der Spins. Je nach Stärke der Wechselwirkungsparameter können diese Ordnungen simultan oder in einer Sequenz von zwei Übergängen zerstört werden.

Im zweiten Teil werden die magnetischen Anregungen eines Streifen-systems ausgehend von einem geeignet parametrisierten Heisenbergmodell studiert. Im Rahmen einer Spinwellenrechnung werden die Magnonenbandstruktur sowie der magnetische Strukturfaktor bei verschwindender Temperatur berechnet. Dabei werden sowohl vertikale als auch diagonale Streifen betrachtet, da beide Konfigurationen in dotierten Antiferromagneten beobachtet werden. Neben den für Streifensysteme typischen inkommensurablen Spinfluktuationen weist die Bandstruktur bei einer endlichen Energie einen kritischen Punkt am antiferromagnetischen Wellenvektor auf, welcher mit der π Resonanz identifiziert werden kann. Sowohl die Spinwellengeschwindigkeiten als auch die Resonanzfrequenz werden als Funktionen des Streifenabstandes und der Kopplungsstärke berechnet. Für geringe Dotierungen ist die Resonanzfrequenz umgekehrt proportional zum Streifenabstand. Schließlich wird

das Modell auf ein Doppelschichtsystem erweitert, wobei verschiedene relative Orientierungen der Streifen in den beiden Ebenen zugelassen werden. Auch hier werden die spektralen Eigenschaften im Rahmen einer Spinwellennäherung berechnet, wobei besonderes Augenmerk auf die Bandaufspaltung in der Nähe der inkommensurablen Niederenergieanregungen sowie der π Resonanz gerichtet wird. Eine x-förmige Dispersion in der Nähe der Resonanz stellt sich dabei als charakteristisch heraus. Der Vergleich mit experimentellen Untersuchungen zeigt, dass bereits ein minimalistisches Spinmodell eine erstaunlich gute Beschreibung der magnetischen Anregungen in streifen-geordneten Systemen liefert.

Dank

mein Dank gilt:

- dem Betreuer der Arbeit, Stefan Scheidl, für die große Unterstützung und seine kollegiale, produktive Anleitung;
 - Herrn Prof. T. Nattermann;
 - den Kollegen in der Arbeitsgruppe, Bernd, Thorsten, Rauno, Andreas, Sergey, Ying, Philipp und Sabine;
 - Simon, der die Gruppe im letzten Jahr verlassen hat;
 - natürlich meiner Familie und meinen Freunden;
 - vor allem aber meiner Freundin Verena.
-

Erklärung

Ich versichere, daß ich die von mir vorgelegte Dissertation selbständig angefertigt, die benutzten Quellen und Hilfsmittel vollständig angegeben und die Stellen der Arbeit - einschließlich Tabellen, Karten und Abbildungen -, die anderen Werken im Wortlaut oder dem Sinn nach entnommen sind, in jedem Einzelfall als Entlehnung kenntlich gemacht habe; daß diese Dissertation noch keiner Fakultät oder Universität zur Prüfung vorgelegen hat; daß sie - abgesehen von den unten angegebenen Teilpublikationen - noch nicht veröffentlicht worden ist sowie, daß ich eine solche Veröffentlichung vor Abschluß des Promotionsverfahrens nicht vornehmen werde. Die Bestimmungen dieser Promotionsordnung sind mir bekannt. Die von mir vorgelegte Dissertation ist von Herrn Priv.-Doz. Dr. S. Scheidl betreut worden.

Köln, den 10. Mai 2004

Frank Krüger

Teilpublikationen

- Frank Krüger and Stefan Scheidl, *Non-universal ordering of spin and charge in stripe phases*, Phys. Rev. Lett. **89**, 095701 (2002)
 - Frank Krüger and Stefan Scheidl, *Spin and charge ordering transitions in stripes*, J. Physique (France) **12**, Pr9-259 (2002)
 - Frank Krüger and Stefan Scheidl, *Spin dynamics of stripes*, Phys. Rev. B **67**, 134512 (2003)
 - Frank Krüger and Stefan Scheidl, *The spin excitation spectrum in striped bilayer compounds*, Phys. Rev. B **70**, 064421 (2004)
-

Lebenslauf

Persönliche Daten

Name	Frank Krüger
Geburtsdatum	2. März 1974
Geburtsort	Hameln
Eltern	Udo Krüger und Gisela Krüger, geb. Liebetrut
Familienstand	ledig
Staatsangehörigkeit	deutsch
Anschrift	Alteburger Str. 117, 50678 Köln

Ausbildung

1981 - 1985	Grundschule, Wiefelstede
1985 - 1987	Orientierungsstufe, Wiefelstede
1987 - 1993	Herbartgymnasium, Oldenburg
Mai 1993	Allgemeine Hochschulreife
1993 - 1995	Zivildienst an der Rheinischen Schule für Gehörlose, Düsseldorf
1995 - 2001	Diplomstudium Physik an der Universität zu Köln Diplomarbeit: <i>Antiferromagnete mit ungeordneter Austauschwechselwirkung Theorie und Anwendung auf das System $\text{La}_{2-x}\text{Sr}_x\text{CuO}_4$</i> bei Priv. Doz. Dr. S. Scheidl
Aug. 2001	Aufnahme des Promotionsstudiums Physik an der Universität zu Köln

Arbeitsverhältnisse an der Universität zu Köln

Juni 2000 - Juli 2001	Studentische Hilfskraft am Institut für Theor. Physik
Aug. 2001 - Dez. 2001	Wissenschaftliche Hilfskraft am Institut für Theor. Physik
Jan. 2002 - Mai 2004	Wissenschaftlicher Mitarbeiter am Institut für Theor. Physik
